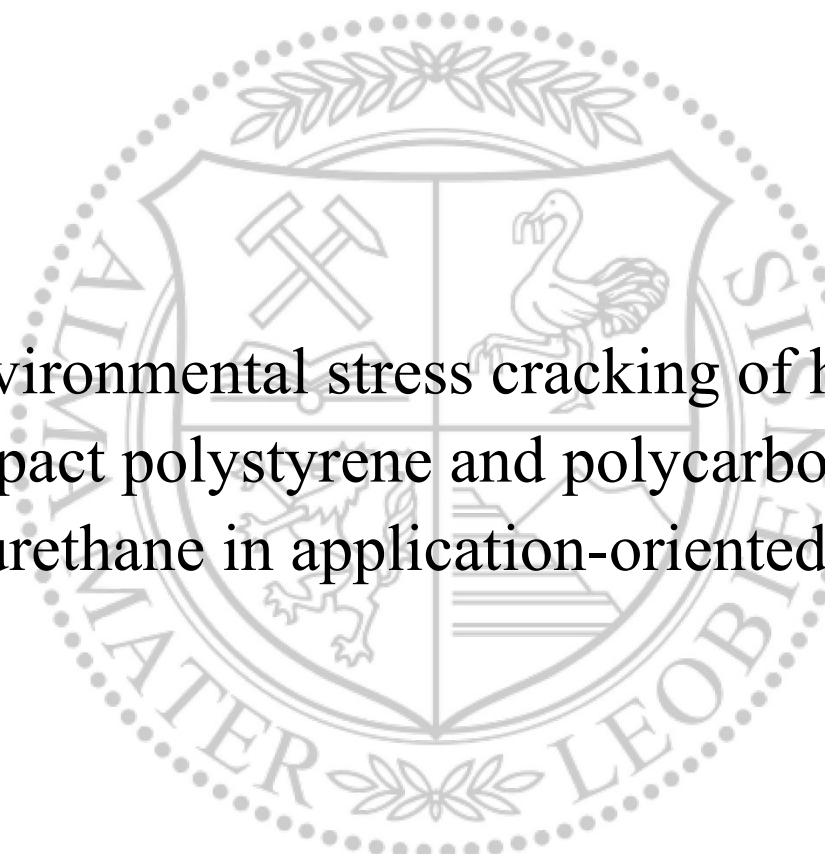Chair of Materials Science and Testing of Polymers

Master's Thesis

# Environmental stress cracking of high-impact polystyrene and polycarbonate polyurethane in application-oriented media

Martin Huemer, BSc

June 2022

**EIDESSTATTLICHE ERKLÄRUNG**

Ich erkläre an Eides statt, dass ich diese Arbeit selbständig verfasst, andere als die angegebenen Quellen und Hilfsmittel nicht benutzt, und mich auch sonst keiner unerlaubten Hilfsmittel bedient habe.

Ich erkläre, dass ich die Richtlinien des Senats der Montanuniversität Leoben zu "Gute wissenschaftliche Praxis" gelesen, verstanden und befolgt habe.

Weiters erkläre ich, dass die elektronische und gedruckte Version der eingereichten wissenschaftlichen Abschlussarbeit formal und inhaltlich identisch sind.

Datum 02.06.2022

Unterschrift Verfasser/in
Martin Huemer

# ACKNOWLEDGEMENT

# KURZFASSUNG

In der realen Anwendung von Werkstoffen werden diese einer Vielzahl an Umgebungseinflüssen, unteren anderem verschiedenen Temperaturen oder Umgebungsmedien, ausgesetzt. Diese können, je nach Beschaffenheit des Polymers, die Eigenschaften des Materials erheblich verändern. Aus diesem Grund ist es von hohem Interesse Materialdaten unter möglichst realitätsnahen Bedingungen zu ermitteln. Zu diesen Zweck wurden zwei unterschiedliche Polymertypen hinsichtlich ihres Verhaltens unter realen Umgebungsbedingungen untersucht.

Im ersten Teil wurde die Spannungsrissbeständigkeit von schlagzähmodifiziertem Polystyrol analysiert. Dazu wurden zwei Polystyrol-Typen, die sich in der Größe der Kautschukpartikel unterscheiden, sowohl statischen als auch zyklischen Belastungen ausgesetzt. Die Messungen wurden jeweils an Luft und in Sonnenblumenöl durchgeführt. Bei statischer Beanspruchung an Luft führten kleinere Kautschukpartikel zu einem deutlich höheren Widerstand gegen Risswachstum. Im Öl zeigte sich, dass mit zunehmender Größe der Kautschukpartikel die Spannungsrissbeständigkeit steigt. Die Detektion der Rissspitze bei Prüfungen in Öl erwies sich messtechnisch als sehr schwierig. Hier liegt noch Verbesserungspotential für zukünftige Untersuchungen. Bei den zyklischen „cracked round bar" Tests erwiesen sich die größeren Partikel an Luft und auch im Öl als deutlich effektiver.

Im zweiten Teil dieser Arbeit wurde ein thermoplastisches Polycarbonat Polyurethan untersucht, welches in Zukunft als Knochen- oder Gewebeersatz mittels additiver Fertigung verwendet werden könnte. Auch hier wurden zwei verschiedene Typen untersucht, die sich in ihrem Verhältnis von Hart-zu-Weichsegmenten unterscheiden. Um das Materialverhalten im Anwendungszustand zu simulieren, wurden die Materialien bei erhöhten Temperaturen, umgeben von einer simulierten Körperflüssigkeit, geprüft. Zur Analyse des Medieneinflusses wurden Auslagerungsstudien, Zugversuche und Wöhlerversuche durchgeführt. Es konnte gezeigt werden, dass die Absorption von körperähnlichen Flüssigkeiten zu einer Abnahme der Steifigkeit und Zugfestigkeit sowie zu einer Zunahme der Bruchdehnung führt. Ähnliche Auswirkungen konnten für das Material mit einem geringeren Anteil an Hartsegmenten durch die erhöhte Temperatur beobachtet werden. Für das Material mit dem höheren Hartsegmentanteil nahm die Zugfestigkeit und

Bruchdehnung bei erhöhter Temperatur zu. Die Wöhlerversuche zeigten, dass sich mit zunehmender absorbierter Flüssigkeitsmenge das Ermüdungsverhalten beträchtlich verschlechtert. Die Zeitfestigkeit der vollständig gesättigten Prüfkörper zeigt eine Parallelverschiebung gegenüber jener der unbehandelten Proben zu 20 % niedrigeren Spannungswerten. Bereits eine Aufnahme von rund 20 % der maximal möglichen Aufnahmemenge an simulierter Körperflüssigkeit bewirkt dieselbe Abnahme der ertragbaren Spannungen.

# ABSTRACT

In practice, materials are exposed to various environmental influences, including different temperatures and environmental media. Depending on the chemical structure of the polymer, this can significantly change the behaviour of the material. For this reason, it is of great interest to determine the properties of materials under conditions that are as close to reality as possible. For this purpose, two different polymer types were investigated regarding their mechanical behaviour under real environmental conditions.

In the first part, the environmental stress cracking resistance (ESCR) of impact-modified polystyrene was analysed. Two polystyrene types, differing in the size of the rubber particles, were subjected to both static and cyclic loads in air and in sunflower oil. Under long-term static loading in sunflower oil, it was found that, as the size of the rubber particles increases, ESCR increases. However, without the influence of the oil, smaller particles resulted in significantly higher resistance to crack growth. The detection of the crack tip during tests in oil proved to be very difficult. There is still potential for improvement with this regard for future investigations. In the cyclic "cracked round bar" tests, the larger particles proved to be more effective in air and also in oil.

In the second part of this work, a thermoplastic polycarbonate polyurethane was investigated for possible future use as bone and tissue replacement via additive manufacturing. Again, two different types were investigated, differing in their hard-to-soft segment ratio. To simulate material behaviour in the application condition, the materials were tested at elevated temperatures immersed in a simulated body fluid. Conditioning studies, tensile tests and high-cycle fatigue tests were performed to analyse the influence of the media. It was shown that absorption of body-like fluids resulted in a decrease in stiffness and tensile strength and an increase in elongation at break. Similar effects were observed for the material with a lower proportion of hard segments due to increased temperature. For the material with the higher hard segment content, the tensile strength and elongation at break increased at the elevated temperature. The high-cycle fatigue tests showed that as the amount of liquid absorbed increases, the fatigue behaviour deteriorates considerably. The fatigue strength of the fully saturated specimens showed a parallel shift compared to that of the untreated specimens to 20 % lower stress values. Even an

absorption of around 20 % of the maximum possible absorption quantity of simulated body fluid causes the same decrease in the tolerable stresses.

# TABLE OF CONTENTS

# SYMBOLS AND ABBREVIATIONS

| | | |
|---|---|---|
| $a$ | Crack length | mm |
| APF | ARBURG plastic freeforming | |
| $A_0$ | Initial cross section | mm² |
| $A_{hyst}$ | Area within the hysteresis loop | J |
| $B$ | Thickness | mm |
| $B_n$ | Net thickness | mm |
| $c$ | Concentration of PBS | % |
| CRB | Cracked round bar | |
| CT | Compact tension | |
| $D$ | Diffusion coefficient | $m^2\ s^{-1}$ |
| $\dfrac{da}{dt}$ | Crack growth rate | $mm\ s^{-1}$ |
| $\dfrac{ds}{dt}$ | Extraction speed | $mm\ s^{-1}$ |
| $E$ | Young's modulus | MPa |
| $E_{dyn}$ | Dynamic modulus | MPa |
| $E_S$ | Secant modulus | MPa |
| $E_s$ | Molar cohesive energy | $J\ mol^{-1}$ |
| ESC | Environmental stress cracking | |
| ESCR | Environmental stress cracking resistance | |
| $F$ | Force | N |
| HIPS | High impact polystyrene | |
| KCl | Potassium chloride | |
| $KH_2PO_4$ | Potassium dihydrogen phosphate | |

| | | |
|---|---|---|
| $K_I$ | Stress intensity factor for mode I | MPa m$^{0.5}$ |
| $K_{I,0}$ | Initial stress intensity factor | MPa m$^{0.5}$ |
| $K_{IC}$ | Critical stress intensity factor | MPa m$^{0.5}$ |
| $K_{ISSC}$ | Resistance to stable crack propagation | MPa m$^{0.5}$ |
| $K_{th}$ | Threshold value of the stress intensity factor | MPa m$^{0.5}$ |
| LEFM | Linear-elastic fracture mechanics | |
| $\Delta m$ | Relative mass gain | % |
| $m_0$ | Initial mass | g |
| $m_t$ | Mass at time t | g |
| $m_\infty$ | Weight at saturation | g |
| $\Delta m_\infty$ | Saturation concentration | % |
| $M_w$ | Molecular weight | g mol$^{-1}$ |
| $N$ | Number of cycles | |
| NaCl | Sodium chloride | |
| Na$_2$HPO$_4$ | Disodium hydrogen phosphate | |
| PB | Polybutadiene | |
| PBS | Phosphate-buffered saline | |
| PCU | Thermoplastic polycarbonate polyurethane | |
| PE | Polyethylene | |
| PS | Polystyrene | |
| $R$ | Stress ratio | |
| $R^2$ | Coefficient of determination | |
| $r$ | Distance to the crack tip | mm |
| RPS | Rubber particle size | |

| | | |
|---|---|---|
| $s$ | Line coordinate along the extension length | mm |
| $t_B$ | Time to fracture | s |
| TEM | Transmission electron microscope | |
| $T_g$ | Glass transition temperature | °C |
| TPU | Thermoplastic polyurethane | |
| $V$ | Molar volume | $cm^3 mol^{-1}$ |
| $W$ | Width | mm |
| $W_{diss}$ | Dissipated energy | J |
| $\delta$ | Solubility parameter | $J^{1/2} cm^{-3/2}$ |
| $\delta_v$ | Phase shift | |
| $\varepsilon_b$ | Elongation at break | % |
| $\eta_\xi$ | molecular friction coefficient | |
| $v$ | Poisson's ratio | |
| $\sigma$ | Stress | MPa |
| $\sigma_a$ | Stress amplitude | MPa |
| $\sigma_B$ | Stress at break | MPa |
| $\sigma_D$ | Fatigue strength | MPa |
| $\sigma_m$ | Mean stress | MPa |
| $\sigma_M$ | Tensile strength | MPa |
| $\sigma_o$ | Maximum stress | MPa |
| $\sigma_u$ | Minimum stress | MPa |
| $\sigma_{ys}$ | Yield stress | MPa |
| $\dfrac{\sigma}{N}$ | Stress per crack-bridging molecule/fibril | MPa |
| $\omega$ | Angular frequency | $s^{-1}$ |

# TABLE OF FIGURES

# 1      INTRODUCTION

Polymer materials are used in many areas, e.g. in the medical sector, warehousing and logistics. In all these applications, the material's service life plays an essential role. Therefore, it is important to determine the material's service life in advance. There are two main approaches for investigating the lifetime of a material: classical stress- or strain-based tests, e.g. creep tests under static loading or Wöhler lines under fatigue loading, as well as fracture mechanics based tests. Furthermore, the lifetime of a polymeric component can be influenced by the presence of an ambient medium due to chemical and physical interactions. Since the material is surrounded by a medium in nearly every application, it is essential to perform tests under environmental conditions as close to reality as possible. Environmental stress cracking (ESC) is a well-known phenomenon in polymer materials, leading to lower fracture stress levels. Literature claims, that ESC is attributed to around 20 % of all failures of plastic products [1, 2]. Hence, great care must be taken when designing components for use in medium environments to avoid dangerous damage, such as destroyed vessels or pump impellers [3]. The technical committee 4 from European Structural Integrity (ESIS-TC4) deals with the ESC in polymers, trying to standardise testing methods based on round robin experiments. In a round robin test, the reproducibility and measurement accuracy are investigated by performing tests by multiple independent scientists from different laboratories. The tests can be performed on the same or different equipment on the same or different specimens with the same or different methods [4, 5].

The focus of this master thesis is to investigate the ESC behaviour of two different polymer systems under their corresponding application conditions. The first objective addresses high-impact polystyrene (HIPS) used for storing and transporting sunflower oil. The influence of the sunflower oil on the creep-, as well as fatigue crack growth was studied by static tests on compact tension (CT) specimens, as well as fatigue tests on cracked round bar (CRB) specimens following fracture mechanical approaches. Furthermore, the influence of the rubber particle size (RPS) on ESC will be analysed. These investigations on HIPS are part of a round robin test organised from ESIS-TC4, with the goal to assess, if fracture mechanics based tests are reliable, fast and reproduceable and hence appropriate to analyse ESC in HIPS. If satisfying, reproduceable results can be achieved within the round

robin test, implementing standardised testing methods with applicability to other polymer materials would be the next step.

The second part of the thesis investigates the influence of a body simulating fluid and elevated temperature on the tensile and fatigue behaviour of a thermoplastic polycarbonate polyurethane copolymer (PCU) for the target application of 3D-printed bone and tissue replacement. Moreover, a conditioning study in the body simulating fluid was conducted at different temperatures. For both polymer systems, reference measurements at ambient air were performed. By comparing the results measured under ambient and application conditions, the environmentally assisted material behaviour can be evaluated.

## 2 THEORETICAL BACKGROUND

This chapter gives a brief overview of the physical background of the influence of an ambient medium on the material properties and the resulting behaviour of the polymers. Moreover, the available approaches for predicting the long-term properties of polymeric materials are explained.

### 2.1 Influence of ambient media on polymer materials

#### 2.1.1 Environmental stress cracking

When stresses and a physical active medium act simultaneously on a polymer, the material tends towards premature crack initiation. Thus, materials fail at lower loads than expected. This phenomenon is called environmental stress cracking [1, 3, 6].

To understand the process of ESC, a detailed investigation of the failure mechanism is necessary. The specimen surface or notch tips are initial points for craze formation. A craze consists of fibrils with microvoids lying between them. Figure 1 a shows the schematic description of crazes. In Figure 1 b crazes in polystyrene (PS) recorded with an electron microscope are displayed. These crazes expand perpendicular to the direction of the applied load. When subjected to an ambient medium, the medium diffuses through the cavities into the material. When reaching the crack tip, it acts as a plasticiser, resulting in a drop in the glass transition temperature ($T_g$) [6, 7]. Consequently, the chain disentanglement gets accelerated because the coefficient of sliding friction between the molecules decreases. This process is illustrated in Figure 1 c.
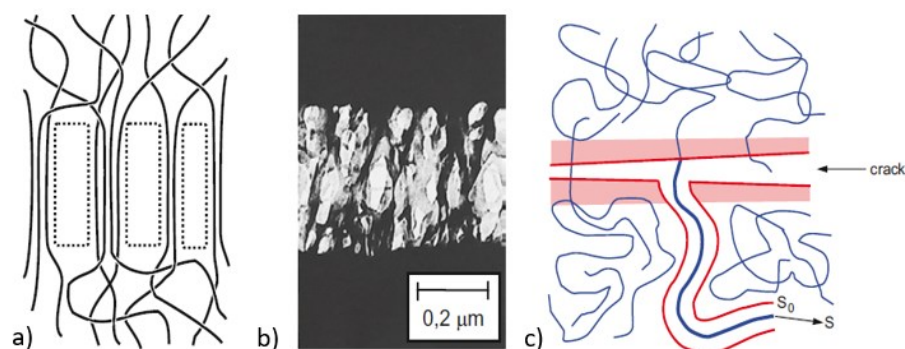


Figure 1: a) Schematic description of crazes [9], b) crazes in PS [9] and c) illustration of the accelerated chain disentanglement [3].

The model from Figure 1 c assumes that disentanglement is determined by purely viscous intermolecular friction. The nearby molecules remain unmovable. Thus, the bridging molecule slides out of a sturdy tube. Examining the equilibrium for a single chain, the following proportionality can be found [3]:

$$\frac{\sigma}{N} \sim \eta_\xi * s \frac{\mathrm{d}s}{\mathrm{d}t} \tag{1}$$

where $\frac{\sigma}{N}$ is the stress per crack-bridging molecule/fibril, $\eta_\xi$ is the molecular friction coefficient, $s$ is the line coordinate along the extension and $\frac{\mathrm{d}s}{\mathrm{d}t}$ is the extraction speed. Here the abbreviation $N$ refers to the number of crack-bridging molecules/fibrils and not to the number of cycles, as it does in the other parts of this thesis. After integrating equation (1) and replacing the drawn-out length with the molecular weight $M_W$, the time to fracture $t_B$ results as [3]:

$$t_B = \eta_\xi \frac{{M_W}^2 \cdot N}{\sigma_B} \tag{2}$$

Corresponding to equation (2), the environmental stress cracking resistance (ESCR) increases when [3]:

- the ambient medium lowers the friction coefficient less significantly,
- the viscosity of the acting medium is higher (slower diffusion through microvoids),
- the chain length is increased,
- the amount of bridging fibrils rises,
- the applied load decreases and
- the mobility of the chains (higher stiffness of chains, more branching) is lowered.

For determining the ESCR, different approaches are available. In all these approaches, the specimen is fully immersed in the medium to enable ESC. At present, the tensile creep test (DIN EN ISO 22088-2), the bent strip test (DIN EN ISO 22088-3) and the ball or pin impression method (DIN EN ISO 22088-4) are used most commonly for ranking the ESCR. In the tensile creep test (Figure 2 a), the specimen is loaded with a constant load below the yield stress. The time to fracture and the tensile stress is measured [3]. In the bent strip test (Figure 2 b), the specimen is exposed to a flexural load by clamping it on a forming plate with a constant radius of curvature. The flexural strain is varied by using different

plates, altering in their radius. After a predefined time, the specimens are visually inspected and the residual tensile strength or residual tensile strain are measured in order to rank materials regarding their ESCR [3]. The "Dow test" represents a modified version of the bent strip test as the forming plate has a parabolic altered curvature. Hence, the surface strain changes continuously in longitudinal direction of the test specimen. The critical strain, at which stress cracks occur, is determined [3]. A further possibility for evaluating the ESC behaviour under flexural loading is the Bell telephone test (ASTM D 1693), originally developed for polyethylene. In this test, ten longitudinally notched specimens are bent in a 180° U-shape. The time, at which 50 % of the specimen show cracks is measured [3]. In the ball or pin impression method (Figure 2 c), an oversized ball or pin is pressed into a hole in the specimen. After a predefined time, the specimens are visually inspected and the residual tensile strength or residual tensile strain is measured. All these methods provide little information about the active mechanisms and the structural parameters that influence ESC. Consequently, they are more or less only useful for material ranking and they are in no case meaningful for lifetime calculations. Moreover, these tests require extra test equipment, they are little known and also error-prone. Therefore, the introduction and standardisation of new test methods, with more information on crack initiation time and crack propagation speed, and consequently the possibility of lifetime prediction, is to be strived for.
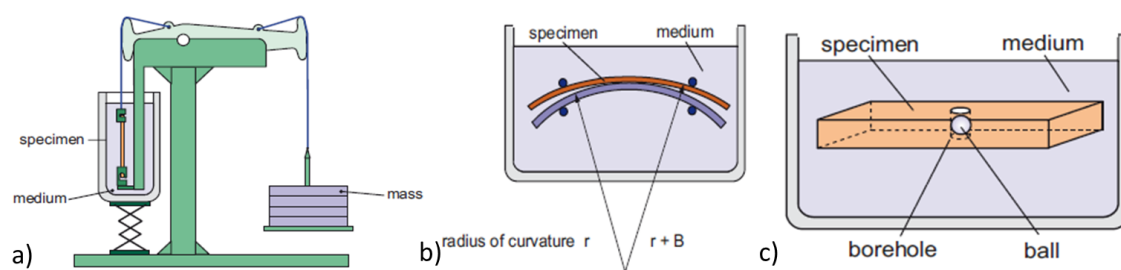


Figure 2: a) Tensile creep test [3], b) bent strip method [3] and c) ball impression method [3].

One approach to obtain more detailed information on the ESC behaviour of materials could be the application of fracture mechanics [10]. The goal is to use already standardised test methods and reliable test setups, and combine them with a media cell for the immersion of the specimens. However, the applicability and reproducibility of these tests under the influence of an active medium must be verified for desired material and medium combinations. For this reason, ESIS-TC4 tries to establish standardised and universally

applicable test methods for analysing ESC. In order to verify the reproducibility of some of these test methods, round robin tests are performed. Schoeffl P. F. [8] published approaches to perform tensile and fatigue tests under the influence of media on conventional testing machines, additionally equipped with a media cell. Fischer J. et al. [9] presented a test procedure for determining the fatigue crack growth on CRB specimens immersed in a medium. Figure 3 shows a typical test setup for applying fracture mechanics to ESC investigations. A CT specimen is exposed to a constant load and a medium. For this purpose, the specimen is immersed in a media cell and the force is applied by a dead weight. The crack propagation is recorded optically. From the acquired data it would be possible to rank materials by their time to crack initiation in a certain medium, by the development of crack growth kinetics during testing and ultimately also perform lifetime analysis based on crack initiation and crack growth kinetics.
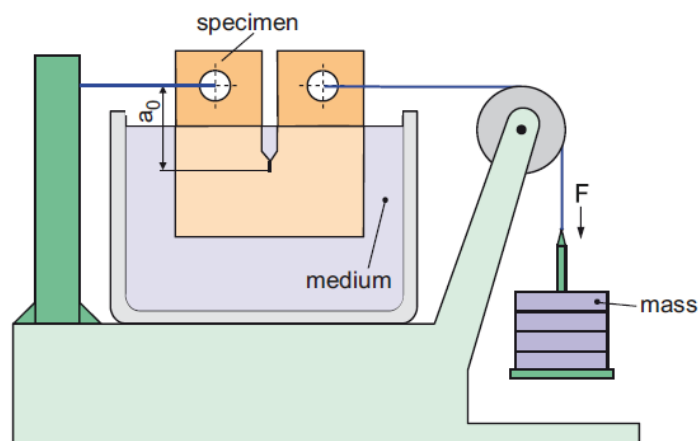


Figure 3: Test setup for static loads tests on CT specimens immersed in a medium [3].

In the following paragraph, some of the influencing factors on ESC are discussed in more detail. At first, the molecular orientation is looked at. For this, the times to fracture of injection moulded and compression moulded specimens, determined in the tensile creep test, are compared. Injection moulding leads to an orientation of the molecular chains whereas compression moulding creates an unoriented chain network. It was found that the tensile creep strength is higher for the injection moulded specimens. The crazes were growing more diffusely in the compression moulded specimens, leading to quicker failure (Figure 4). Due to the higher orientation caused by the injection moulding process, the surface on these specimens first had to soften under the influence of the medium before crazes could initiate [3].
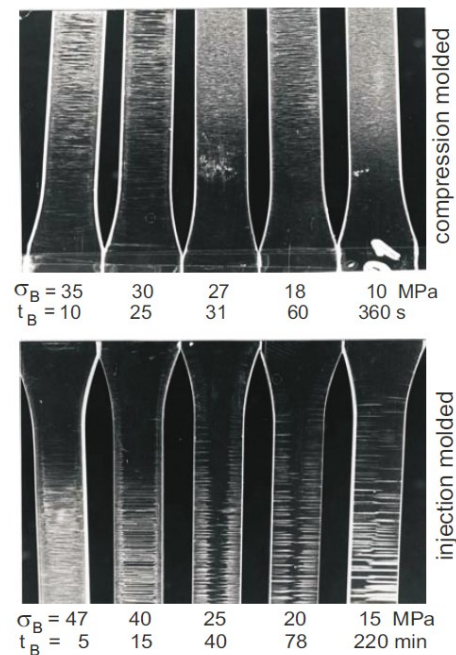
Figure 4: Craze growth in compression and injection moulded PS specimens under the influence of an active medium [3].

A further indication of how strong the tendency for a material and medium combination to ESC is, is the solubility parameter $\delta$. The concept of solubility is explained in more detail in chapter 2.1.2. However, at this point it should be noted, that the closer $\delta$ of the polymer and the active medium are, the higher is the possibility that ESC occurs because of the plasticisation effect [3]. For PS, $\delta$ is between 17.5 and 20 $J^{1/2}$ $cm^{-3/2}$ [3] and for sunflower oil it is approx. 16 $J^{1/2}$ $cm^{-3/2}$ [10]. Hence, $\delta$ is similar for PS and sunflower oil and ESC can be expected. Besides the solubility parameter, also the viscosity of the medium influences the ESC behaviour. If the viscosity of the medium is too high and the crack propagation is too fast, the medium cannot flow to the crack tip and hence it cannot facilitate chain disentanglement. However, the influence of the viscosity must be considered together with the molecular weight and its distribution. The fibril density in front of the crack tip is higher for high-molecular weight polymers than for low-molecular weight ones. This higher density hampers the flow of the medium to the crack tip [3].

## 2.1.2 Conditioning

When polymer materials are stored in a medium, they can absorb a certain amount of the medium depending on the interaction between the material and the fluid. As the polymer absorbs the medium, the material swells because the molecule distances increase [11]. If

this swelling is unlimited, so that all intermolecular binding forces are overcome, the polymer dissolves in the medium [3]. The interaction between polymer and medium can be described as solubility. Solubility and swelling depend on the chemical composition and structure of the polymer, the type and strength of the intermolecular forces, the type of medium and the environmental conditions such as temperature and pressure [3]. With increasing similarity between the structure of the polymer and the medium, the solubility rises. The solubility parameter is defined by equation (3), where $E_s$ is the molar cohesive energy and $V$ is the molar volume [3].

$$\delta = \sqrt{\frac{E}{V}} \tag{3}$$

The smaller the difference between the $\delta$ of the polymer and the medium, the more pronounced is the swelling [3]. This swelling causes an increase in molecular mobility due to a weakening of molecular binding forces. Consequently, the stiffness, hardness and glass transition temperature of the polymer often decrease. As long as no chemical changes in the polymer chains occur, elongation at break tends generally to increase. In some cases, however, the polymer may degrade and consequently become brittle [12, 13].

Two further parameters must be defined regarding medium absorption, namely the saturation concentration $\Delta m_\infty$ and the diffusion coefficient $D$. These parameters are influenced by the free volume, the $T_g$, the storing temperature, the geometry of the specimen and the chemical composition of the diffusing medium [14, 15]. The saturation concentration corresponds to the maximum amount of medium that the polymer can absorb. When this concentration is reached, an equilibrium is established. The relative mass gain $\Delta m$ is calculated with equation (4), where $m_t$ is the mass at time $t$ and $m_0$ is the initial mass after drying [10, 13–15].

$$\Delta m = \left(\frac{m_t - m_0}{m_0}\right) \cdot 100\,\% \tag{4}$$

The maximum of $\Delta m$ equals $\Delta m_\infty$. The diffusion process is described by Fick's second law of diffusion (equation (5)), where $c$ is the concentration of the medium in the specimen, $t$ is the diffusion time and $x$ the position [10, 13–15].

$$\frac{\partial c}{\partial t} = D \left( \frac{\partial^2 c}{\partial x^2} \right)$$

(5)

When assuming that the concentration of the medium remains constant at the polymer surface, the specimen is fully immersed and the material is isotropic, the concentration can be expressed as a function of the thickness $d$ (equation (6)) [10, 13–15].

$$c(x,t) = c_0 \left[ 1 - \frac{4}{\pi} \sum_{n=0}^{\infty} \frac{(-1)^n}{2n+1} exp \left( \frac{-(2n+1)^2 \pi^2 Dt}{d^2} \right) cos \left( \frac{(2n+1)\pi x}{d} \right) \right]$$

(6)

By integrating equation (6) over the layer thickness, the relative mass uptake $m_t/m_\infty$, where the uptake is related to weight of the specimen at saturation $m_\infty$, can be expressed with equation (7) [13, 16–18].

$$\frac{m_t}{m_\infty} = \frac{4}{d} \left( \frac{D}{\pi} \right)^{1/2} t^{1/2}$$

(7)

In Figure 5 the influence of propanol on the long-time behaviour of polystyrene is illustrated. In area III, the time to failure at high applied stresses is the same in air and in propanol. Due to the short time to failure, hardly any influence of the medium is given. Hence, failure is mainly dependent on the material properties. By reducing the applied stress and thus increasing the testing time (and thereby the time subjected to media), the influence of the medium becomes more and more evident since the gap to the results at air increases. This correlation is based on the fact that with longer testing times the medium has more time to diffuse to the crack tip and hence facilitate chain disentanglement. Furthermore, the influence of the specimen thickness is illustrated. Increased widths shift area II to longer times. After the medium had enough time to diffuse into the specimen, the curves flatten (area I). At this stage, no influence of the specimen thickness is given. The time to failure is mainly dependent on the ambient medium and its ability to interact with the polymer as ESC is responsible for failure at these stress levels [3].
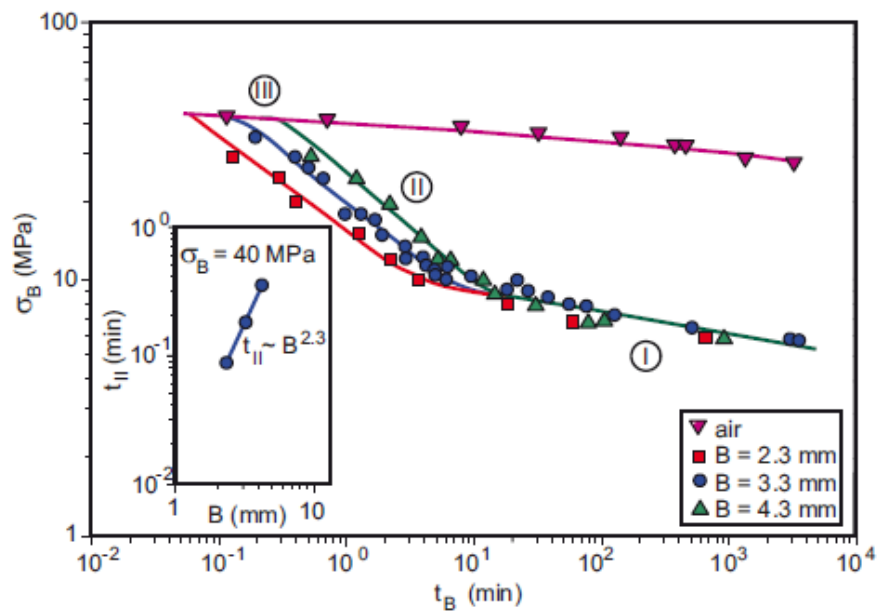
Figure 5: Influence of propanol on the long term behaviour of polystyrene for different specimen thicknesses [3].

## 2.2 Long-term properties of polymer materials

For determining the long-term properties of a product, it is important to consider the type of load during application. Literature states three main load types, which significantly differ in their effect on the long-term behaviour of materials (Figure 6)[8]. Compared to monotonic loading, known from conventional tensile tests, the bearable stresses of a polymeric material decrease with longer loading time for static, as well as fatigue loading. Compared to monotonic and static loading, fatigue loads are the most dangerous regarding the life span since the failure stress decreases the most over time. Moreover, the influence of an active medium on the failure stress is depicted schematically in Figure 6. A shift to lower failure levels can be expected. For abrupt failures at the beginning of the load application, there may be no influence of the medium due to the short interaction time. However, the exact behaviour can differ for each material and medium combination. Hence, application-oriented investigations are crucial for determining material properties.
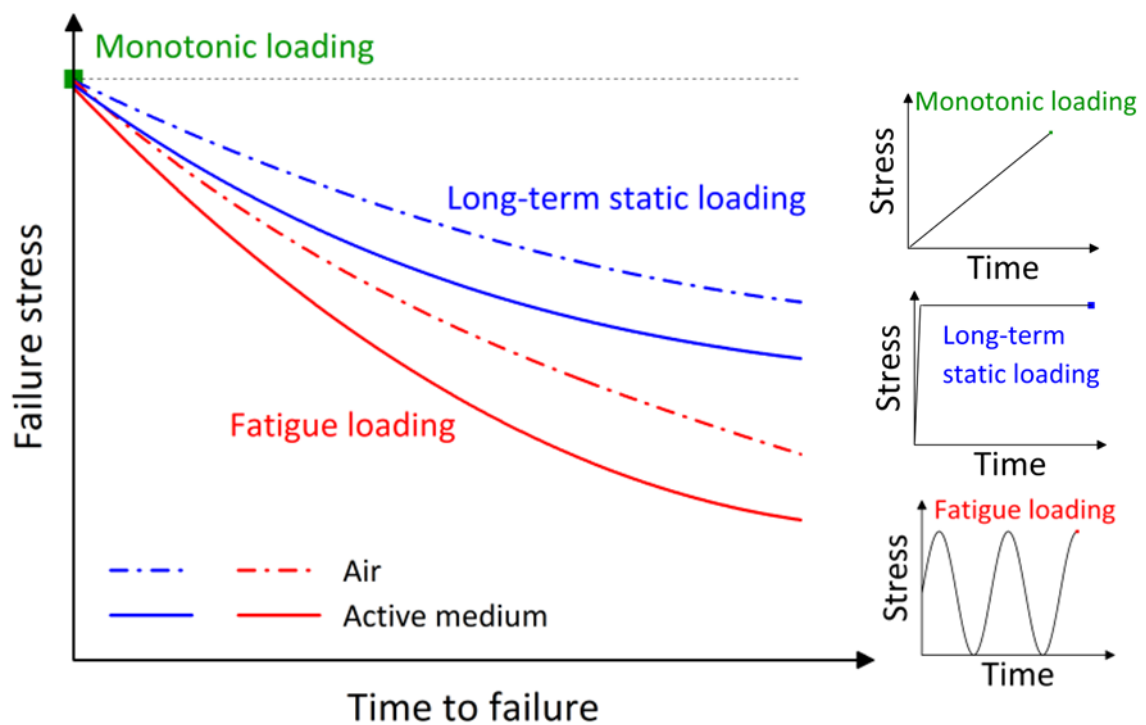
Figure 6: Schematic illustration of the three main load types (monotonic, static and fatigue) at air and under the influence of an active medium and their effect on the failure stress.

To describe the long-term behaviour of a material, two main approaches are available. The conventional way investigates the long-time bearable stresses or strains either under static or fatigue loads. The second possibility is the fracture mechanics approach, where the stress intensity factor $K_I$ is used as characterising property. For the conventional approach, the service life is evaluated on initially uncracked, smooth-surfaced specimens, whereas the fracture mechanics approach is performed on pre-cracked specimens. The conventional approach investigates the initiation and propagation of (multiple) cracks and service life results from damage accumulation. In contrast, fracture mechanics deals with the inititiation, and also with the propagation, of one main crack. The fracture mechanics approach provides several advantages, such as a shorter testing time, a reduced number of specimens and a material-specific fracture toughness, which is independent of the specimen type [19–21]. Depending on the expected damage mechanism (damage accumulation or one dominant crack) the appropriate approach must be selected. Both philosophies are explained in more detail in chapters 2.2.1 and 2.2.2.

### 2.2.1    Fracture mechanics approach

Within fracture mechanics, various approaches are available. Depending on the investigated material and testing conditions, a suitable approach must be chosen. The literature distinguishes between linear-elastic, elastic-plastic, post-yield and full-scale fracture mechanics. For the linear-elastic fracture mechanics (LEFM), the material must behave linear elastic on a global scale, with only little, negligible plastic zones in front of the crack tip. Within the LEFM, the loading mode significantly influences the material behaviour and consequently the obtained results. The three loading modes are visualised in Figure 7, with Mode I representing tensile loading, Mode II in-plane shearing and Mode III out of plane shearing  [20, 22]. The tests conducted in this thesis are based on Mode I, consequently for the following chapters Mode I is assumed.
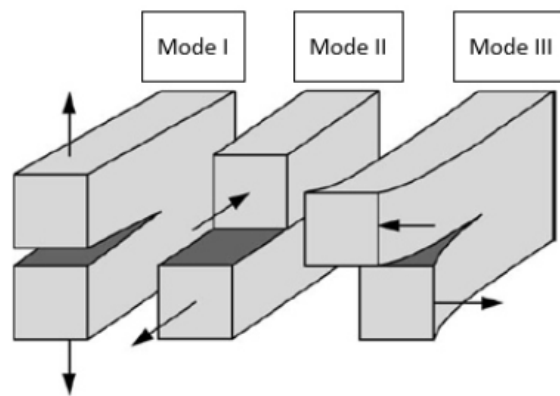


Figure 7: Visualisation of the different loading modes [20].

A characterising parameter for the fracture mechanics approach is the stress intensity factor ($K_I$). $K_I$ describes the stress distribution at the crack tip (Figure 8 a). Stresses decrease with the square root of the distance to the crack tip $r$. At the crack tip ($r \rightarrow 0$), the elastic solution assumes that the stress rises to infinity. However, in reality, the stresses are limited by plastic deformations at the yield stress $\sigma_{ys}$ (Figure 8 b). $K_I$ is calculated with equation (8), where $\sigma$ is the applied global stress, $a$ is the crack length and $f\left(\frac{a}{W}\right)$ is a factor incorporating the specimen geometry ($a$ and the width $W$) and the specimen configuration. When $K_I$ reaches a certain, material specific value, called the critical stress intensity factor $K_{IC}$, which is a measure for the fracture toughness of the material, fracture occurs [20, 23].

$$K_I = \sigma \cdot \sqrt{\pi \cdot a} \cdot f\left(\frac{a}{W}\right) \tag{8}$$
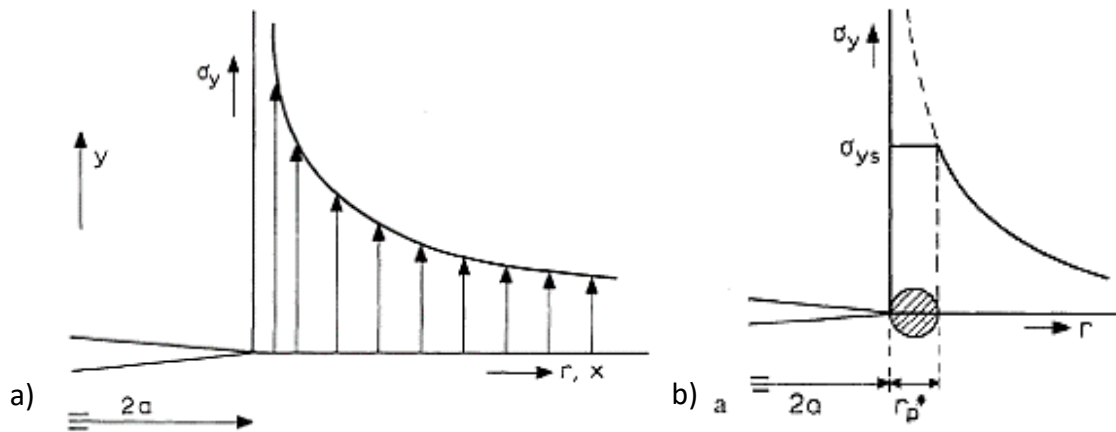
Figure 8: a) Stress distribution in front of the crack tip for the elastic solution [23] and
b) limited stress distribution due to plastic deformation at yield stress [23].

For crack propagation measurements in LEFM for long-term static and fatigue loads, the double-logarithmic plot of crack growth rate $\frac{da}{dt}$, or $\frac{da}{dN}$ over $K_I$ results in a characteristic S-shaped curve with three different regions (Figure 9). This diagram illustrates the linear correlation between $\frac{da}{dt}$, or $\frac{da}{dN}$ and $K_I$ in region II. Region II represents $K_I$ values for stable crack growth. For lower $K_I$ values, in region I, the crack speed decreases significantly. Below a threshold value $K_{th}$, cracks do not propagate. When $K_I$ converges towards $K_{IC}$ (region III), the crack grows at very high rates through the remaining material. The linear section in region II is described by the following power law, originally proposed by Paris and Erdogan [20, 24]:

$$\frac{da}{dt} = A \cdot K_I^m \ or \ \frac{da}{dN} = A \cdot ((1 - R) \cdot K_I)^m \tag{9}$$

where *A* and *m* are empirical constants, depending on the material, temperature, ambient medium and, in case of fatigue loads, loading ratio (*R*) only [25–27]. The parameter *R* is defined as the ratio between minimum ($F_{min}$) to maximum force ($F_{max}$) or minimum ($\sigma_u$) to maximum stress ($\sigma_o$) or minimum ($K_{I,min}$) to maximum stress intensity factor ($K_{I,max}$).

$$R = \frac{F_{min}}{F_{max}} = \frac{\sigma_u}{\sigma_o} = \frac{K_{I,min}}{K_{I,max}} \tag{10}$$

The advantage of aforementioned law is, that if A and m are determined experimentally, they can be used to calculate the lifetime of any component under similar loading conditions by integration of equation (9), by determining the components $K_I$ via analytical expressions or finite element analysis. Hence, these parameters have great potential for

the direct comparison of materials with regard to the total expected lifetime of a component as well.
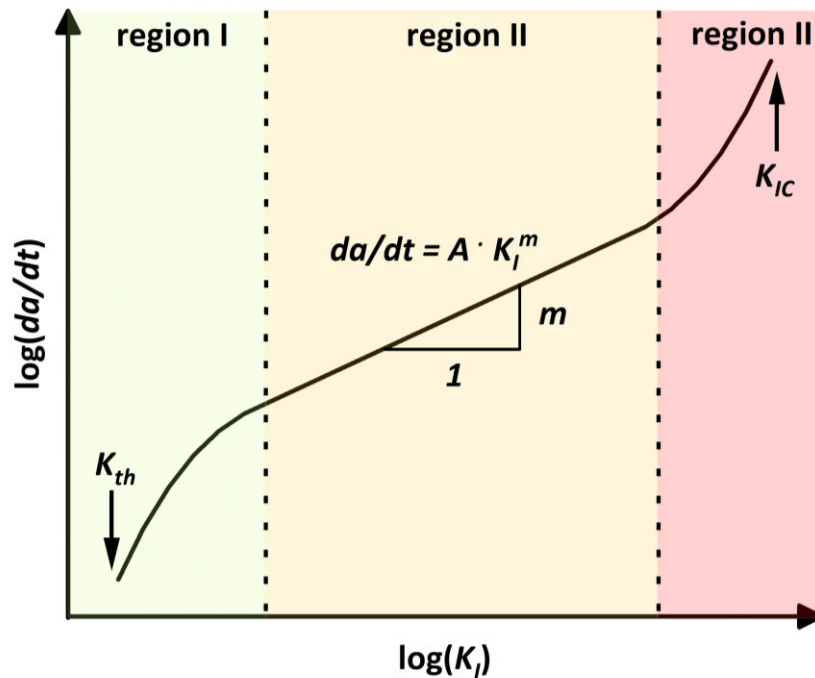


Figure 9: Schematic crack growth kinetic curve with the three characteristic regions.

## 2.2.2 Conventional approach

As indicated above, the conventional approach mainly deals with the time (in static loading) or cycles to failure (in fatigue loading) based on the applied stress or strain. As the intended area of application of the examined PCU material is mostly subjected to cyclic loading, only the fatigue life approach will be discussed here. The total fatigue life approach is conducted with the high-cycle fatigue test ($S$-$N$ test), standardised in DIN 50100. It is distinguished between stress- and strain-controlled loading. In this thesis, stress-controlled fatigue testing with a sinusoidal load is applied. For this case, the acting load is defined by a constant mean stress $\sigma_m$ and a constant stress amplitude $\sigma_a$ (Figure 10). Based on the resulting values for maximum stress $\sigma_o$ and minimum stress $\sigma_u$, three different load groups can be categorised: pulsating compressive, alternating and pulsating tensile stresses. The literature distinguishes between seven load cases, depending on the applied load ratio (Figure 11) [3].
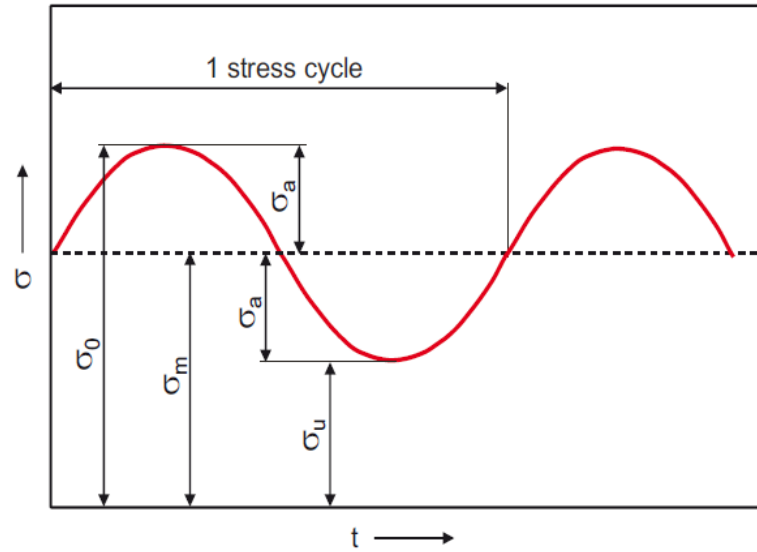
Figure 10: Stress–time diagram for fatigue testing [3].
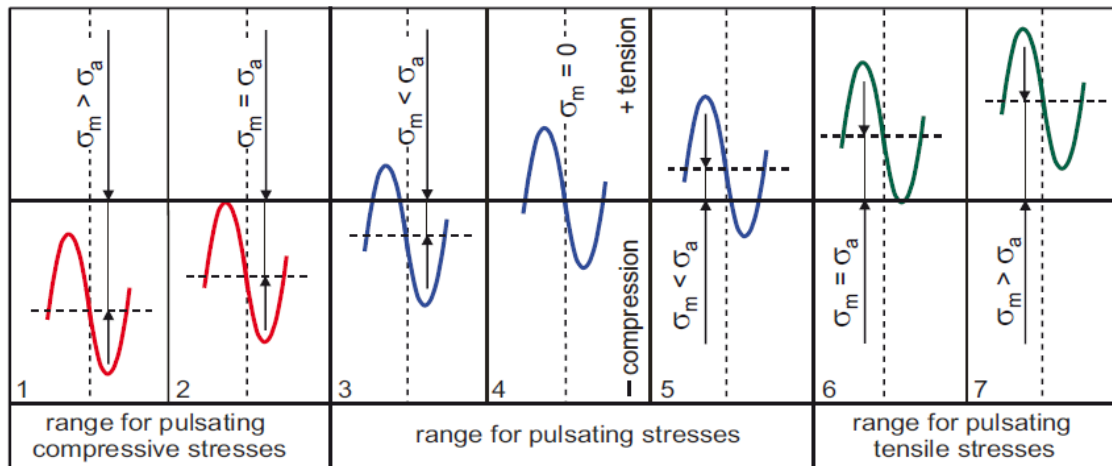


Figure 11: Load cases for fatigue testing [3].

The result of this fatigue test is a $S$-$N$ curve, with $S$ representing the applied stress and $N$ the number of cycles. This curve is typically plotted in a double-logarithmic scale, log $(\sigma)$ over log $(N)$. The $S$-$N$ curve can be approximated by two segments, shown in Figure 12. The first area represents the linear decreasing finite life fatigue strength $\sigma_i$. The second area is called fatigue strength $\sigma_D$. Here, the curve can be horizontal (Type I) or slightly decreasing (Type II). For type I, stresses below this threshold can be sustained for an infinite number of cycles [3]. However, the literature states that $\sigma_D$ cannot be determined for polymer materials. Influences such as creep and ageing of the polymer lead to an ongoing decrease in strength [28, 29]. For this reason, the focus in determining $S$-$N$ curves for polymers is on approximating the fatigue strength as accurately as possible.
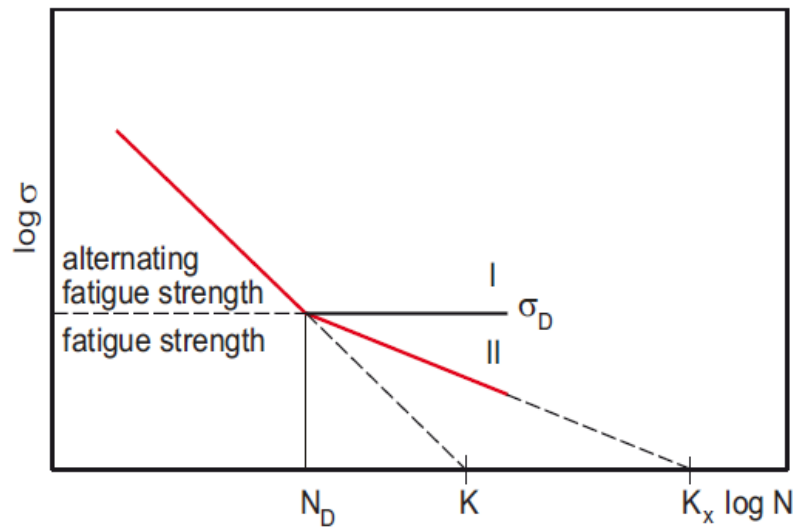
Figure 12: Idealised S-N curve [3].

The material behaviour of polymers is influenced by viscoelasticity. This viscoelasticity leads to a time-delayed material response to applied loads or strains [11]. In Figure 13 the phase shift $\delta_v$ between the applied stress and the resulting strain due to viscoelasticity under cyclic loading is illustrated. The applied sinusoidal load $\sigma(t)$ (equation (11)) is followed by a sinusoidal strain $\varepsilon(t)$ (equation ((12)), where $\omega$ is the angular frequency [11].

$$\sigma(t) = \sigma_0 * \sin(\omega * t) \tag{11}$$

$$\varepsilon(t) = \varepsilon_0 * \sin(\omega * t - \delta_v) \tag{12}$$
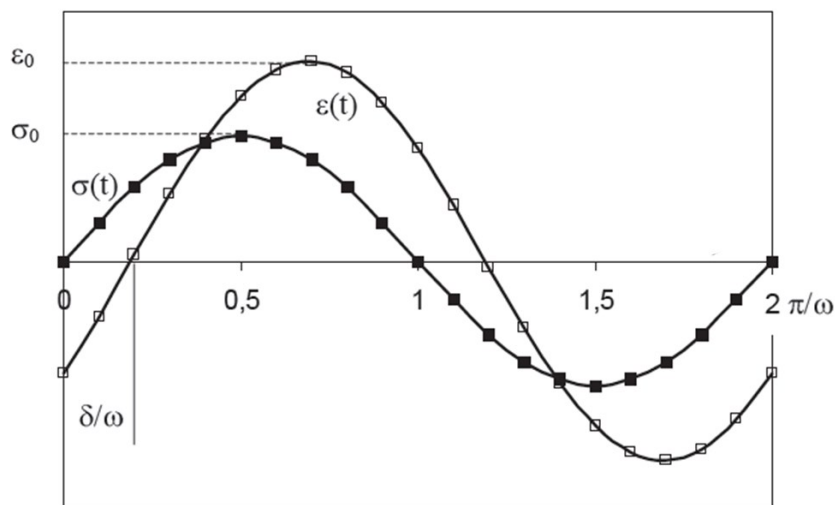


Figure 13: Phase shift between the applied stress and the resulting strain due to viscoelasticity under cyclic loading [11].

By plotting the stress over the strain, hysteresis loops are obtained (Figure 14). The area within this loop ($A_{hyst}$) equals the dissipated energy ($W_{diss}$) (equation (13)) [11]. This loss in energy is caused by the damping ability of the material due the phase shift between stresses and strains. Furthermore, two different moduli, the dynamic ($E_{dyn}$) and the secant modulus ($E_S$) can be calculated with equations (14) and (15) for the quantitative analyses of the hysteresis loops [30, 31]. $E_{dyn}$ is calculated from the maximum ($\sigma_{max}$) and minimum stress ($\sigma_{min}$) and the corresponding maximum ($\varepsilon_{max}$) and minimum strain ($\varepsilon_{min}$) at one specific cycle. Hence it describes the instantly reaction of the material at this cycle number and consequently, it characterises material damage. By investigating $E_{dyn}$ at different load levels and stress ratios, it can be determined at which load cases and after how many load cycles material damage must be expected. In contrast to that, $E_S$ accumulates material damage and cyclic creep [32]. By comparing the development of these moduli as a function of applied cycles, more detailed information regarding the material constitution during testing can be found. Information on linear or non-linear viscoelastic material behaviour can be obtained from the shape of the hysteresis loops. Moreover, the development of the hysteresis area provides information about the dissipated energy.

$$A_{hyst} = W_{diss} = \sigma_0 * \sin(\delta_v) * \varepsilon_0 * \pi \tag{13}$$

$$E_{dyn} = \left| \frac{\sigma_{max} - \sigma_{min}}{\varepsilon_{max} - \varepsilon_{min}} \right| \tag{14}$$

$$E_S = \frac{\sigma_{max}}{\varepsilon_{max}} \tag{15}$$
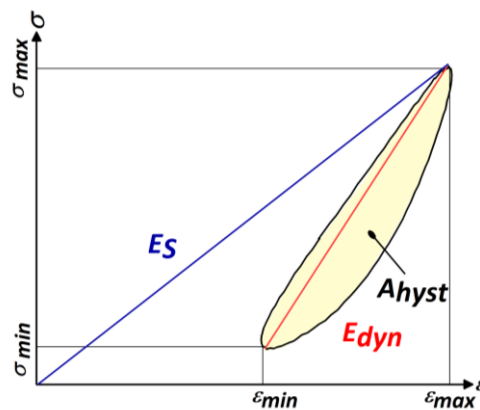


Figure 14: Schematic illustration of a hysteresis loop for cyclic loading.

# 3    MATERIALS AND MEDIA

This chapter introduces the investigated materials and the ambient media in which they were tested. From this point on, all main chapters of this thesis are split into two subtopics. The first topic deals with HIPS tested in sunflower oil, whereas the second one comprises the influence of phosphate-buffered saline (PBS) on PCU.

## 3.1    HIPS and sunflower oil

Polystyrene (PS) is a usually brittle thermoplastic polymer which is used for special applications such as packaging and interior linings of refrigerators. It is therefore often modified with rubber, for example with polybutadiene (PB). The result of this modification is HIPS, a high-impact polystyrene-butadiene block copolymer. Figure 15 illustrates the chemical structure of HIPS and its monomers, PS and PB. Since PS and PB are immiscible, separation between these polymers occurs, with PB being uniformly distributed within the coherent PS matrix [12, 27].
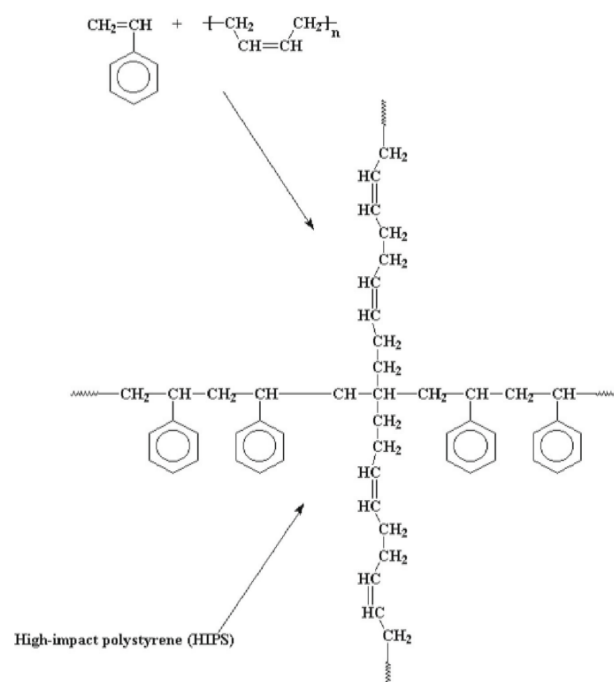


Figure 15: Chemical structure of HIPS and its monomers PS and PB [33].

The interface between the rubber particles and the matrix favours craze formation. To form these crazes, a certain stress must be applied. Many small rubber particles lead to the

formation of multiple crazes simultaneously. Consequently, $\sigma_{ys}$ increases as particle size decreases. Due to the high number of small rubber particles, the formed crazes hit rubber particles much faster. As a result, the elongation at break $\varepsilon_b$ is lower for HIPS with more rubber particles [12, 34, 35].

Besides this influence on stress and strain, rubber modification is also applied to improve the ESCR of HIPS. Several studies investigating ESC of HIPS were conducted in the past [27, 36–39]. Bubeck A. et al. studied the influence of rubber particle size (RPS) and molecular weight on the fracture behaviour for 23 different HIPS grades. The authors found that fracture time increases with increasing RPS and molecular weight [40]. Similar observations were made by Andena L. et al., testing two HIPS grades differing in their RPS [27].

The same two HIPS grades tested by Andena L. et al. were investigated in this thesis as part of the round robin test from ESIS-TC4. Both materials were kindly supplied by Polimeri Europa SpA (Italy). The first grade is a specifically designed commercial high-ESCR grade (ICE R 830D), labelled as HIPS A. The second one is a general-purpose commercial grade (ICE R 850E), labelled as HIPS B. This material is to be used for storage and transportation of sunflower oil. Hence, the polymers were tested in the predefined sunflower oil from Carapelli Giglio Oro. In Figure 16, transmission electron microscope images of HIPS A and HIPS B visualise the difference between both grades. HIPS A shows clearly larger rubber particles [27].
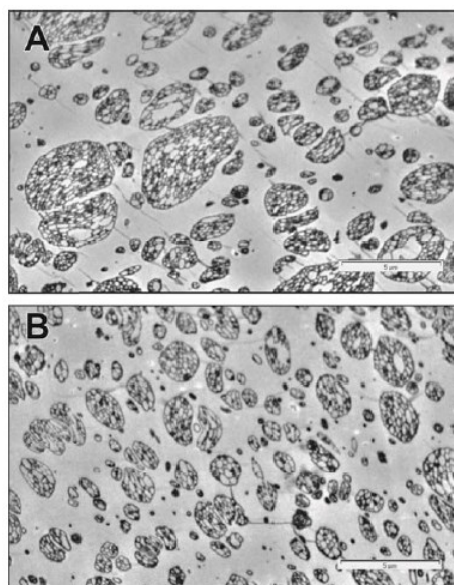


Figure 16: TEM pictures of HIPS A and HIPS B [27].

## 3.2    PCU and PBS

PCU is a block copolymer consisting of hydroxyl-terminated polycarbonate and polyurethane, based on diisocyanate and chain extenders (low molecular weight glycol). The polycarbonate acts as the soft segment and the polyurethane as the hard segment. The characteristic chemical structure of PCUs can be seen in Figure 17 and Figure 18 schematically illustrates the general composition of thermoplastic polyurethanes (TPU). The mechanical properties are regulated by varying the ratio of hard to soft segments [41, 42].
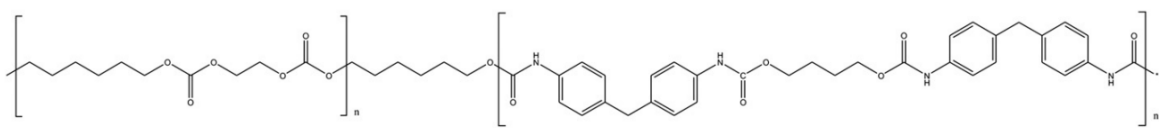


Figure 17: Typical chemical structure of PCU [42].
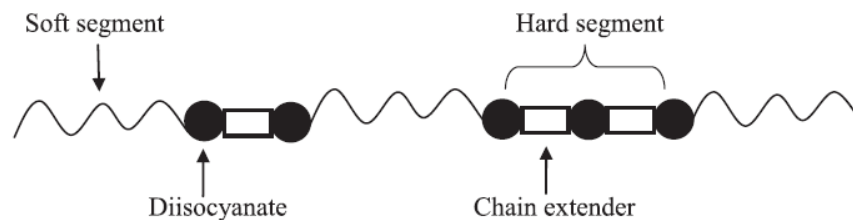


Figure 18: Schematic illustration of a segmented TPU [43].

PCU is a biostable and biocompatible material combined with satisfying mechanical properties. It is of great interest that implants show sufficient material properties when exposed to the human body environment during their service life. Plenty of studies investigated the in-vitro behaviour of PCU, with a focus on water uptake, changes in molecular weight and mechanical properties [41, 44–46]. Moreover, in-vivo studies examined the effect of physiological environments on PCU [47, 48].

In this thesis, the two materials Bionate® 80A and Bionate® 75D from Koninklijke DSM N.V (Netherlands) were investigated. Bionate® consists of poly(hexamethylene carbonate), methylene di(p-phenyl isocyanate) and 1,4-butanediol [42, 49]. Bionate® 80A is a softer material, with a hardness of 83A (ASTM D2240), whereas the hardness of Bionate® 75D is 73D (ASTM D2240). Moreover, Bionate® 80A is more flexible and has a lower tensile strength than Bionate® 75D [50]. Based on these properties, the idea is to use these two materials for additively manufactured bone and tissue implants in the future. Bionate® has

been used in medical applications, e.g. hip and knee joints, over the past two decades. It is backed by a FDA (Food and Drug Administration) Master File [50]. The FDA is a federal agency of the Department of Health and Human Services in the United States. Part of their work is to control the safety and efficacy of biological products and medical devices [51]. Since this material can be processed by Additive Manufacturing and it is approved for use in medical devises and implants, it is excellent for achieving a rapid time to market without costly and time-consuming approval procedures.

With regard to the application conditions for implant materials, different approaches are available for simulating the body environment [44, 52]. In this thesis, PBS was chosen as the ambient medium. PBS is a phosphate-buffered saline solution, which imitates the ionic concentration, osmolarity and pH value of human body fluids [53].

# 4 EXPERIMENTAL

The following chapters provide information on the specimens and test methods. First, the specimen dimensions and preparation are explained. The test setup, test conditions, data acquisition and data processing are discussed hereafter. Moreover, required equations for the evaluation, which were not already listed in chapter 2, are provided.

## 4.1 Influence of sunflower oil on HIPS

As indicated above, the tests on HIPS were performed within the framework of a round robin exercise of ESIS-TC4. This material is mainly loaded in a static way during its application. However, to gather more information on the applicability of different fracture mechanics based tests, also fatigue loading via CRB specimens was examined.

### 4.1.1 Specimen dimensions and preparation

The CRB specimens made of HIPS A and HIPS B were kindly provided by the Johannes Kepler Universität Linz. They were machined with a CNC machine from compression moulded plates in accordance with DIN EN ISO 19063-2:2020. Afterwards, a sharp circumferential notch with an approximate depth of 1.5 mm was introduced with a razor blade. The dimensions of the CRB specimen are depicted in Figure 19 in mm.
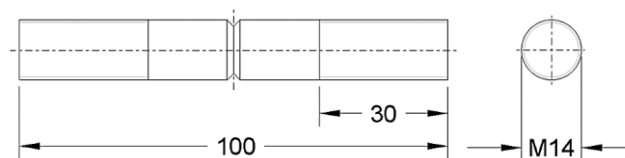


Figure 19: Dimensions of the CRB specimen in mm.

The CT specimens were milled from compression moulded plates of HIPS A and HIPS B. The moulding process was carried out on the press Polystat 300 from Schwabenthan (Germany). A detailed report of the processing parameters and processing steps is attached in appendix (A1). Before the specimens were milled, the plates were annealed to rule out possible effects due to physical ageing. For this purpose, the plates were placed in the Steriliser SF110 from Memmert GmbH + Co. KG (Germany) for one hour at 90 °C. Then the oven got switched off, and the plates cooled down to room temperature with the oven staying closed. The geometry of the CT specimens with dimensions in mm can be seen in

Figure 20. For some of the specimens, side-grooves with a depth of 0.6 mm and a radius of 0.25 mm were added to guide the crack propagation. In the root of the machined V-notch of all specimens, a sharp pre-crack with a target length of 0.6 mm was introduced with a pointed blade No. 692.60 (Martor KG, Germany) and the microtome RM2255 (Leica Microsystems GmbH, Austria) via broaching. The notch was manufactured step by step with a feed depth of 20 µm per revolution.
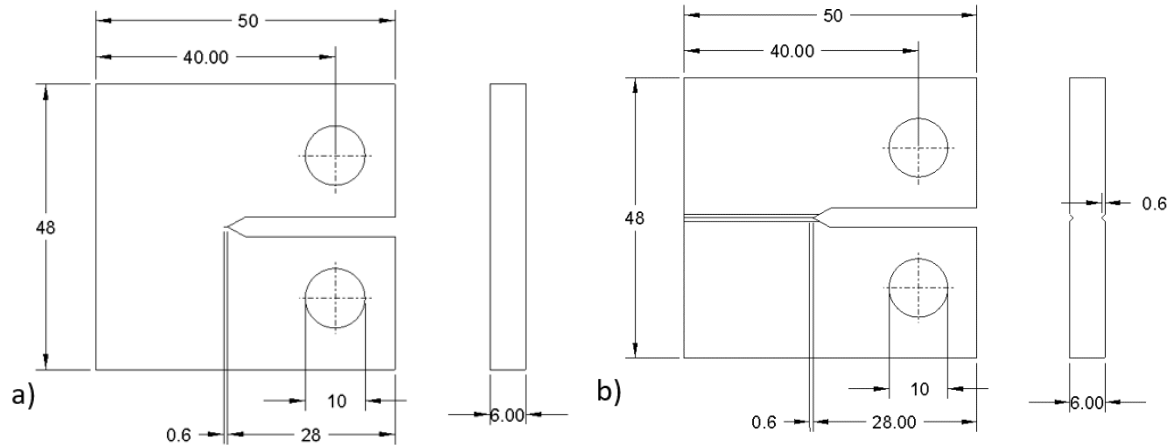


Figure 20: Dimensions of the CT specimen: a) without side-grooves, b) with side-grooves.

L. Andena et al. [27] investigated the applicability of LEFM on the same HIPS grades used in this thesis. They found that no thickness effect occurs for specimen thicknesses between 5 to 20 mm. Furthermore, they claim that the apparent fracture toughness slightly decreases for ligament sizes ($W$-$a$) smaller than 10 mm. For the CT specimen presented above, the initial ligament size at the beginning is approximately 21.4 mm ($W$ = 40 mm, $a$ = 18.6 mm). With increasing crack lengths, the ligament sizes decrease. However, stress intensities at ligament sizes lower than 10 mm are not in the area of interest of this thesis. Hence, the influence of small ligament sizes on the toughness does not affect the results presented in chapter 5.1.2.

### 4.1.2 Cyclic load tests

The cyclic load tests were executed with the CRB specimens. The tests were performed according to ISO 18489:2015 with a testing frequency of 10 Hz (sinusoidal waveform) at 23 °C in air and in sunflower oil. All specimens were loaded with different force levels ($R$ = 0.1), with maximum forces between 170 and 620 N, to reach cycles to failure between 10000 and 10000000 on the servo-hydraulic testing machine MTS 831 TableTop System

(MTS Systems Corporation, USA). $R = 0.1$ is used as it is the most harmful for the material, resulting in fast crack initiation and propagation [54]. The machine was equipped with a 15 kN load cell and a media cell. The media cell is adjustable in its height to be able to clamp the samples outside the cell. Hence, testing at air was also possible. The CRB specimens were held at both ends with threaded clamps. The test set-up is shown in Figure 21.
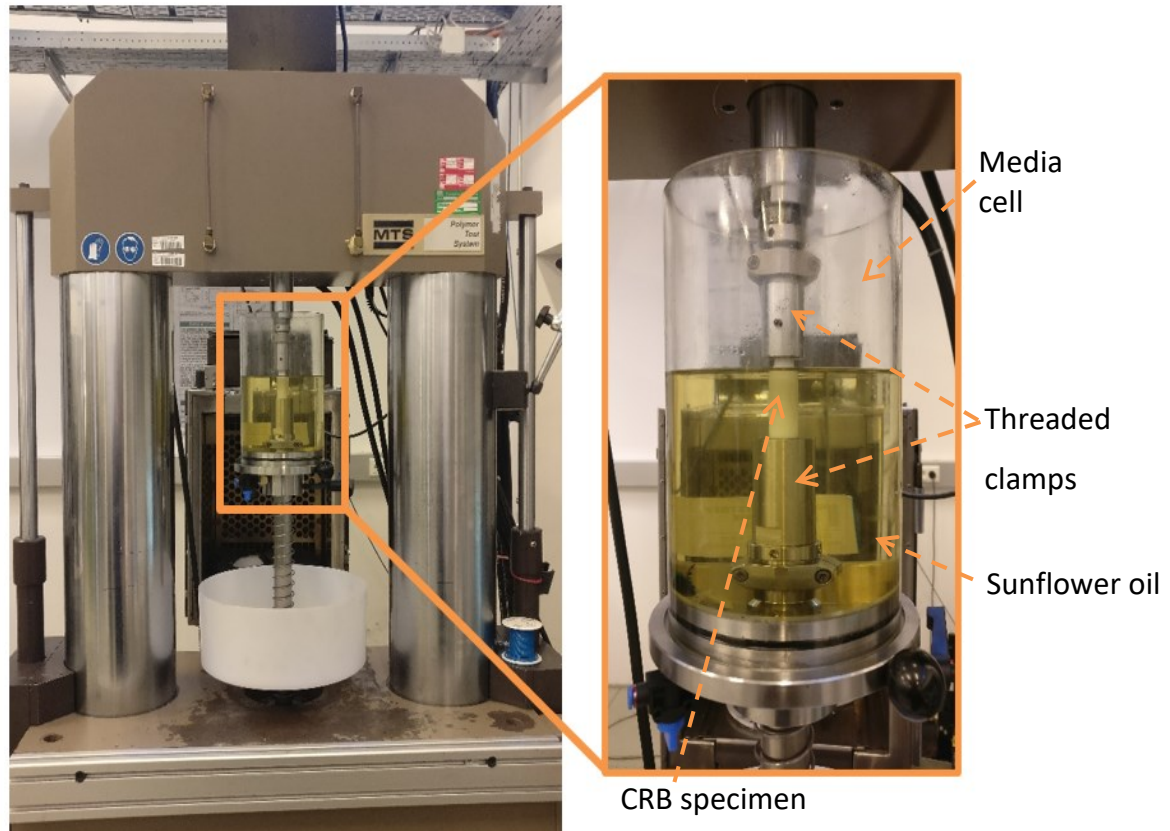


Figure 21: Test setup for the cyclic load test on CRB specimens.

After testing, the fracture surfaces were investigated with the light microscope SZX-ILLB2-200 (Olympus Corporation, Japan). Additionally, the actual initial notch depth was obtained. The data was evaluated in accordance with ISO 18489:2015. The range of the applied initial stress intensity factors $\Delta K_{I,0}$ was calculated with equations (16)-(19) from Benthem and Koiter [55–57], where *F* is the applied force, *a* is the crack length and *r* is the specimen radius. $\Delta K_{I,0}$ is the difference between the maximum ($K_{I,0,max}$) and minimum ($K_{I,0,min}$) initially applied stress intensity factors.

$$K_I = \frac{F}{\pi \cdot b^2} \cdot \sqrt{\frac{\pi \cdot a \cdot b}{r}} \cdot f\left(\frac{b}{r}\right) \tag{16}$$

$$\Delta K_{I.0} = K_{I.0,max} - K_{I.0,min} \tag{17}$$

$$b = r - a \tag{18}$$

$$f\left(\frac{b}{r}\right) = \frac{1}{2} \cdot \left[ 1 + \frac{1}{2} \cdot \left(\frac{b}{r}\right) + \frac{3}{8} \cdot \left(\frac{b}{r}\right)^2 - 0.363 \cdot \left(\frac{b}{r}\right)^3 \cdot 0{,}737 \left(\frac{b}{r}\right)^4 \right] \tag{19}$$

### 4.1.3 Static load tests

The static load tests were performed with the CT specimens on the universal testing machines Z010 and Z250 (ZwickRoell GmbH & Co. KG, Austria), both equipped with a 0.5 kN load cell. The tests were conducted at different load levels between 105 and 275 N at 23 °C in air and in sunflower oil. The crack propagation was tracked with the camera Prosilica GT 6600 (Allied Vision Technologies GmbH, Germany), equipped with a 100-mm Tokina AT-X M100 PRO Dmacro objective (Kenko Tokina Co., Japan) and mounted on a tripod, and the software Mercury RT (Sobriety s.r.o, Czech) at rates between 0.01 and 8 fps, depending on the speed of crack propagation. To ensure constant, sufficient lightning, two lamps of the model COOLH dedcool (Dedolight California, USA) were installed. Since the curved media cell used for the cyclic tests caused a distortion of the pictures, a box-shaped cell was fabricated for the static tests. The specimens were pin loaded with special clevises. The test setup can be seen in Figure 22.
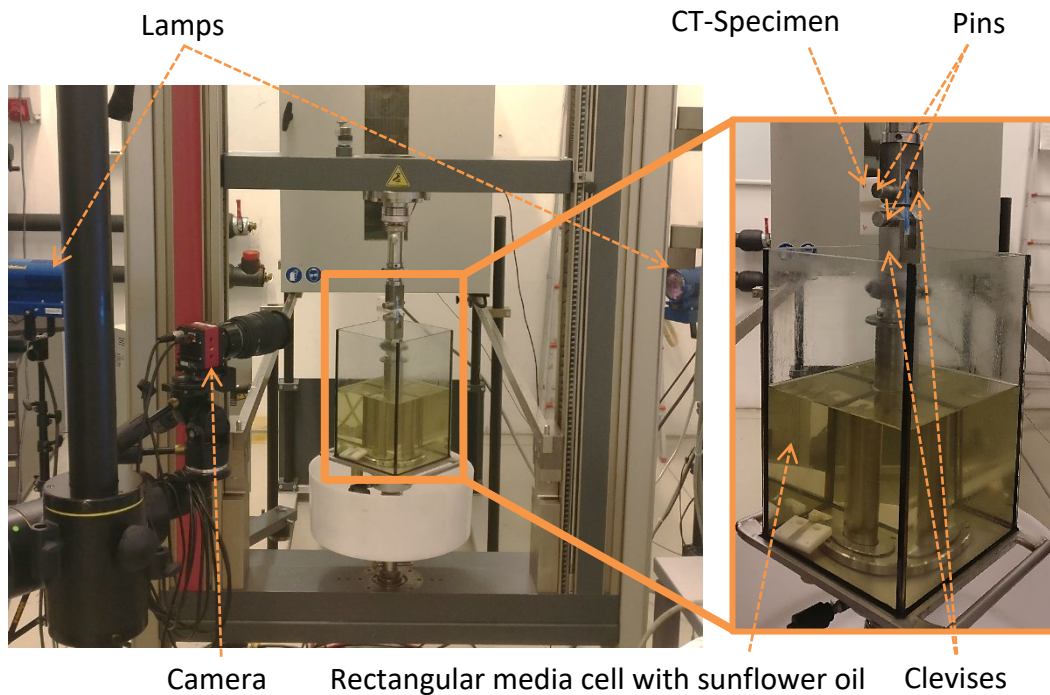
Figure 22: Test setup for the static load tests on CT specimens.

The crack length was measured manually for selected pictures of interest with the software Image J. For the specimens tested in oil, the crack tip opening was less pronounced. Hence, those specimens were coloured black with a water-based acrylic marker to facilitate crack tip detection. In Figure 23, the measurement in Image J is illustrated for specimens in air and in oil.
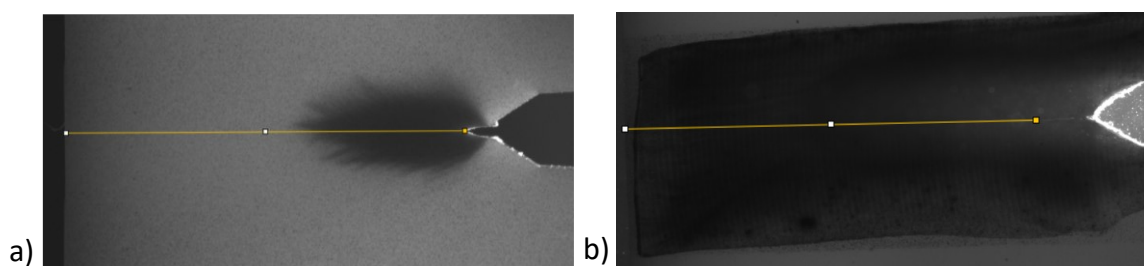


Figure 23: Crack length measurement with Image J a) at ambient air and b) in sunflower oil.

The fracture surfaces were analysed in the same manner as previously described for the CRB specimens. The applied stress intensity factors were calculated with equations (20)-(22), where $F$ is the applied force and $B$ the thickness [20]. For side-grooved CT specimens, the resulting net thickness $B_n$ must be considered [58]. The crack growth rate was determined by using the first derivative of the crack length versus time curve.

$$K_I = \frac{F}{B \cdot \sqrt{W}} \cdot f\left(\frac{a}{W}\right) \tag{20}$$

$$f = \frac{\left(2 + \frac{a}{W}\right)}{\left(1 - \frac{a}{W}\right)^{3/2}} \left[0{,}886 + 4{,}64 \cdot \left(\frac{a}{W}\right) - 13{,}32\left(\frac{a}{W}\right)^2 + 14{,}72 \cdot \left(\frac{a}{W}\right)^3 - 5{,}6 \cdot \left(\frac{a}{W}\right)^4\right] \tag{21}$$

$$K_I = \frac{F}{\sqrt{B * B_n * W}} \cdot f\left(\frac{a}{W}\right) \tag{22}$$

## 4.2 Influence of PBS on PCU

### 4.2.1 Specimen dimensions and preparation

Multipurpose Bionate® 75D and Bionate® 80A specimens were fabricated using the freeformer 200-3X (ARBURG GmbH + Co KG, Germany). The freeformer uses the ARBURG Plastic Freeforming (APF) technology, an additive manufacturing process where granulates are melted in two injection units and then applied to the component drop by drop through needle valve nozzles [59]. The printing parameters used can be found in the appendix (A2). The geometry of the specimens is based on DIN EN ISO 527-2 1A (Figure 24). Due to size restrictions of the temperature chamber and the media cell, the length of the parallel part (*L1)* was adapted. By decreasing this length, lower absolute values for the displacement can be expected and hence testing until break within the test equipment is possible. The exact dimensions of the specimens for the tensile and high-cycle fatigue tests are listed in Table 1.
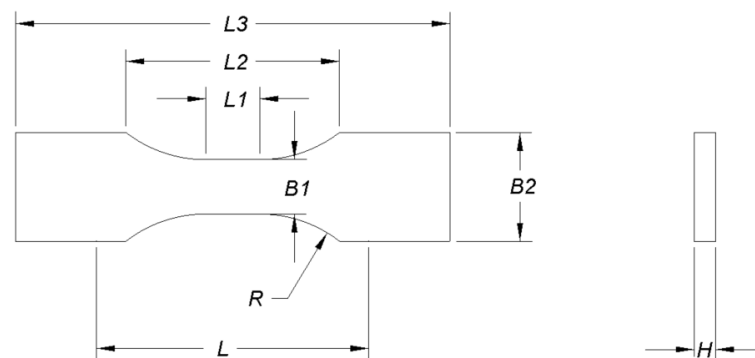


Figure 24: Illustration of the multipurpose specimen.

Table 1: Dimensions of the multipurpose specimens.

| Parameters | Tensile test | High-cycle fatigue test |
|---|---|---|
| Total length *L3* [mm] | 80 | 40 |
| Length of the parallel part *L1* [mm] | 10 | 5 |
| Radius *R* [mm] | 24 | 12 |
| Distance between the wide parallel sides *L2* [mm] | 40 | 20 |
| Width at the ends *B2* [mm] | 20 | 10 |
| Width of the narrow part *B1* [mm] | 10 | 5 |
| Thickness *H* [mm] | 4 | 2 |
| Clamping length *L* [mm] | 42 | 21 |

### 4.2.2 Conditioning

Some of the specimens for the tensile and high-cycle fatigue tests were conditioned in PBS before testing. A detailed overview on the test plan and hence the required conditioning is given in Table 2. Before the specimens were immersed in PBS, they were dried in the vacuum oven Vacutherm (Heraeus Holding GmbH, Germany) at 80 °C until the mass was constant. For the tensile tests, five specimens of Bionate® 75D and Bionate® 80A each were stored at 23 and 37 °C in PBS. For the high-cycle fatigue tests, 20 Bionate® 75D specimens were stored at 37 °C. For the storing, a tailored fixture of a glycol modified polyethylene terephthalate (PETG) was manufactured by fused filament fabrication to ensure complete immersion and the largest possible surface area of the specimens to the medium (Figure 25). This fixture was placed in a glass container filled with the PBS solution. For conditioning at 37 °C, the container was placed in the oven Steriliser SF110. The mass was checked regularly using a balance (Sartorius AG, Germany). In order to record only the quantity of the PBS, which diffused into the test specimen, the liquid adhering to the outside of the test specimen was removed by means of compressed air before weighing. The pH value of the PBS was checked regularly. It stayed constant at 7.4.

Table 2: Overview on the conditioning and test plan for the Bionate® multipurpose specimens.

| | Material | Sample number | Temperature [°C] | Conditioning environment | Testing environment |
|---|---|---|---|---|---|
| **Tensile test** | **Bionate® 75D** | 5 | 23 | Air | Air |
| | **Bionate® 80A** | 5 | | PBS | |
| | **Bionate® 75D** | 5 | 37 | Air | |
| | **Bionate® 80A** | 5 | | PBS | |
| **High-cycle fatigue test** | **Bionate® 75D** | 12 | 37 | Air | Air |
| | | 15 | | Air | PBS |
| | | 10 | | PBS | PBS |
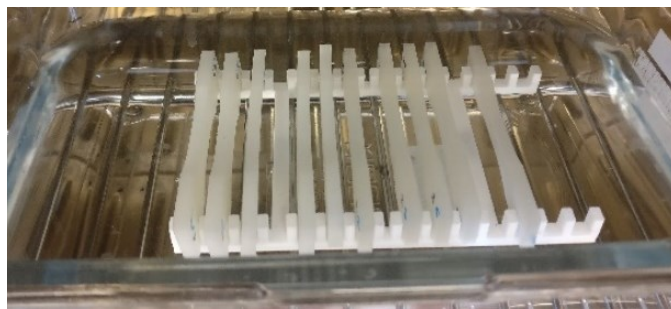


Figure 25: Conditioning of specimens for tensile testing at 37 °C in PBS.

The PBS solution was prepared as follows [60]:

The ingredients listed in Table 3 were solved in 0.8 l of deionised water. The magnetic stirrer C-MAG HS 7 from IKA®-Werke GmbH & CO. KG (Germany) was used to ensure a satisfactory solution and distribution. Next, the pH value was set at 7.4 by adding sodium hydroxide. The pH value was determined with the pH meter Orion S Star from Thermo Fisher Scientific Inc. (USA). At last, 7.2 l deionised water were added.

Table 3: Composition of the prepared PBS solution.

| Chemical | Concentration [g/l] | Total amount [g] |
|---|---|---|
| Sodium chloride (NaCl) | 8.0 | 64 |
| Potassium chloride (KCl) | 0.2 | 1.6 |
| Disodium hydrogen phosphate ($Na_2HPO_4$) | 1.42 | 11.36 |
| Potassium dihydrogen phosphate ($KH_2PO_4$) | 0.24 | 1.92 |

### 4.2.3   Tensile tests

The tensile tests were performed on the universal testing machines Z010 and Z250, both equipped with a 10 kN load cell. The test specimens were clamped in wedge jaws. The testing procedure was based on DIN EN ISO 527-2. For determining the Young's modulus and the Poisson's ratio, the loading rate was set to 1 mm/min. In contrast to the standard, the loading rate switched to 50 mm/min after the strain exceeded 1 % in order to ensure the evaluability of $E$ and $v$. For testing at 37 °C, temperature chambers were used and the specimens were pre-tempered for at least one hour. The elongation for evaluating the Young's modulus and Poisson's ratio was determined optically. For this purpose, a fine speckle pattern was applied to one side of the test specimens using a graphite spray (Figure 26). A LED lamp was placed in the temperature chamber to ensure sufficient illumination. The optical strain measurement was performed with the camera Prosillica GT 6600 and the Mercury software. The camera was equipped with a 100-mm Tokina AT-X M100 PRO Dmacro objective (Kenko Tokina Co., Japan) and mounted on a tripod. The test setup is displayed in Figure 27.
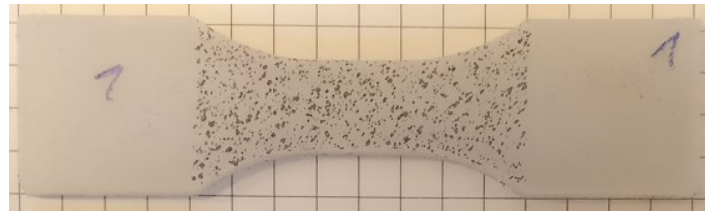


Figure 26: Specimen for tensile testing with speckle pattern for optical measurement of the elongation.
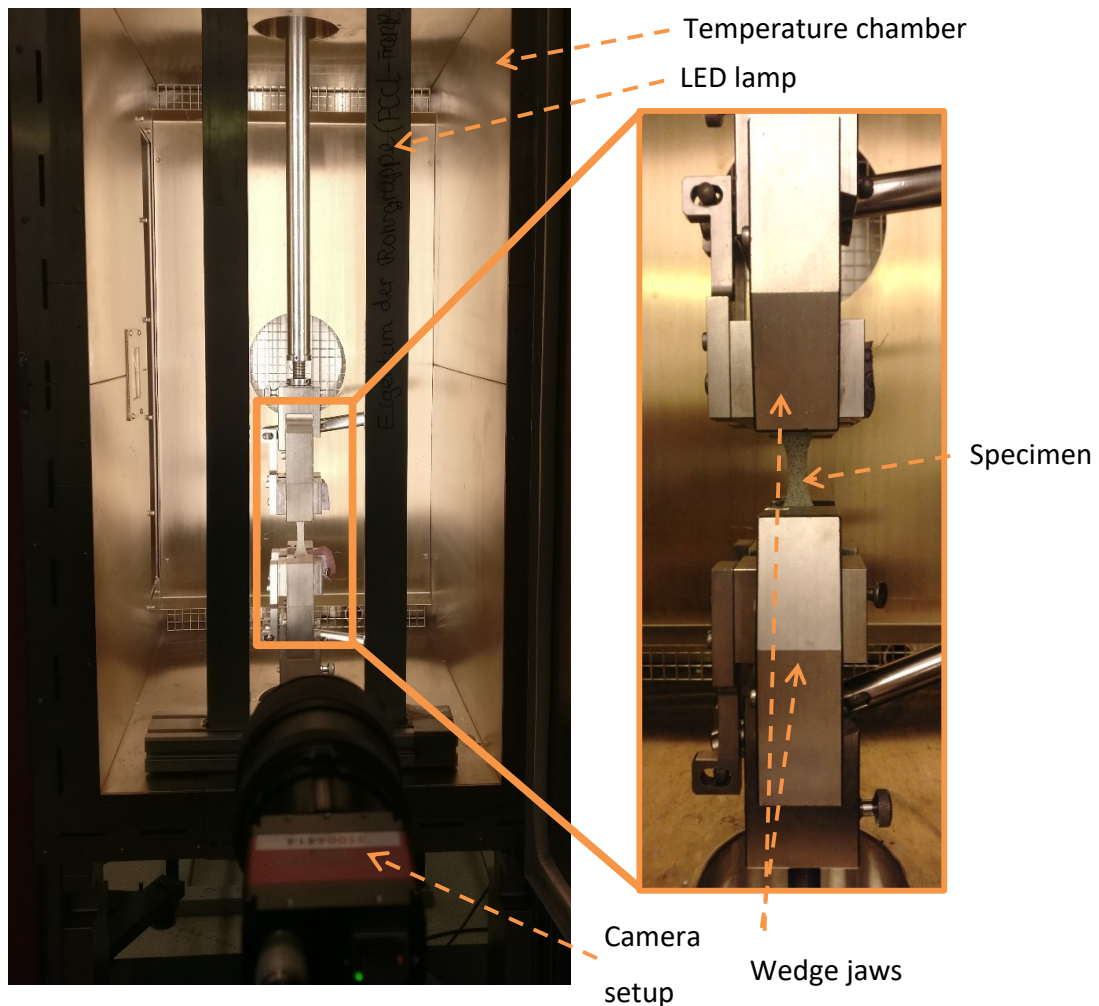
Figure 27: Test setup for the tensile test on multipurpose specimens.

For comparing the influence of the temperature and the medium on the stress-strain curves, the crosshead displacement was used for calculating the strain. The reason for this is that at high strains above approx. 500 %, the optical strain measurement no longer worked because of the high distortion of the speckle pattern and unsuitable lighting conditions in this area. Stresses and strains were determined as technical stresses and strains. The data evaluation was based on DIN EN ISO 527-2. The tensile strength $\sigma_M$ was calculated with equation (23), where $F_{max}$ is the maximum force and $A_0$ is the initial cross-section of the specimen. The Young's modulus $E$ was determined with equation (24), where $\sigma_2$ is the stress at a strain of 0.25 % ($\varepsilon_2$) and $\sigma_1$ is the stress at a strain of 0.05 % ($\varepsilon_1$). The Poisson's ratio $v$ was calculated with equation (25), where $\varepsilon_x$ is the strain perpendicular to the test direction and $\varepsilon_y$ is the strain in test direction. $v$ is evaluated as mean value between strains in test direction from 0.4 to 0.6 %. For smaller strains, $v$ showed a large scattering,

leading to unreasonable results. Between strains from 0.4 to 0.6 %, almost constant values for $v$ could be obtained.

$$\sigma_M = \frac{F_{max}}{A_0} \qquad\qquad (23)$$

$$E = \frac{\sigma_2 - \sigma_1}{\varepsilon_2 - \varepsilon_1} \qquad\qquad (24)$$

$$v = -\frac{\varepsilon_x}{\varepsilon_y} \qquad\qquad (25)$$

### 4.2.4   High-cycle fatigue tests

The high-cycle fatigue tests were performed on an electric dynamic test machine Electropuls® E3000 (Instron, USA), equipped with a loadcell calibrated for 3 kN. The tests in ambient air were performed in a temperature chamber and spring-loaded wedge jaws were used. For testing in the PBS solution, the solution was heated up with the temperature control unit C6 (Lauda Dr. R. Wobser GmbH & Co. KG, Germany) and the specimens were mechanically clamped. In order to stop the medium from condensing, the media cell was covered with a cling film. The test setup is shown in Figure 28.
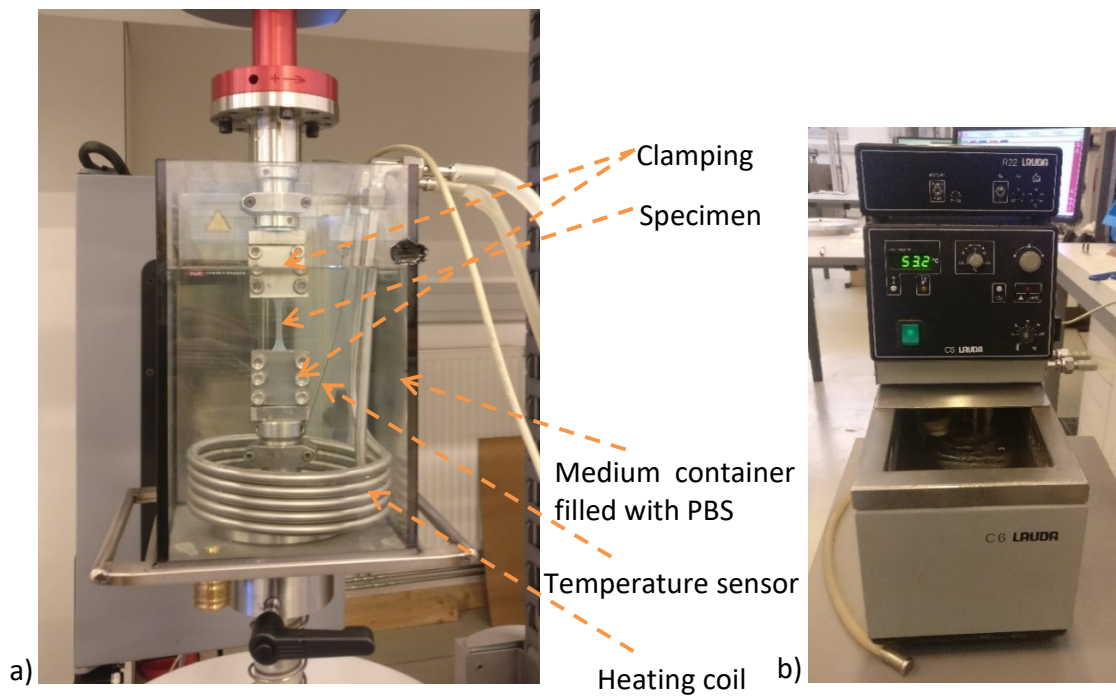


Figure 28: a) Test setup for the high-cycle fatigue tests on multipurpose specimens and b) temperature control unit.

The tests were performed in accordance with DIN 50100 with $R = 0.1$ at three different load levels (maximum forces between 235 and 340 N) with the aim of reaching cycle numbers from 10000 to 150000 until failure. $R = 0.1$ is often used for high-cycle fatigue tests, since it was observed, that values for $R$ close to 0 are the most harmful for the material [61, 62]. However, $R = 0$ is hardly to achieve with the currently available machines due to inertia. For each load level, at least three specimens were tested. The testing frequency was set to 1 Hz (sinusoidal waveform). At higher frequencies, the machine could not reach the set target forces due to the large deformation of the material. For cyclic testing, attention to hysteresis must be paid. The viscoelastic behaviour of polymer materials results in a phase shift between stress and strain and consequently in a loss work. This dissipated energy leads to hysteretic heating of the material. Due to the low applied testing frequency, negligible hysteretic heating can be assumed [11]. All specimens were pre-tempered for at least one hour before testing.

# 5    RESULTS AND DISCUSSION

This chapter presents the obtained results for the influence of sunflower oil on the fatigue behaviour of HIPS followed by the result for the influence of PBS on the physical and mechanical properties of PCU. The order is based on the description of the experimental setups in chapter 4. The analysis in the first part demonstrates the influence of impact modification on the ESCR of a HIPS material. The second part illustrates the importance of studying the long-term behaviour of polymers used for medical applications.

## 5.1    Influence of sunflower oil on HIPS

### 5.1.1    Cyclic load test

The cracked round bar test was performed according to ISO 18489:2015. This method was originally developed for accelerated fracture mechanics characterisation of polyethylene (PE) [63, 64]. By adjusting the test parameters, the CRB test can be adapted for other thermoplastic materials [65]. Within the framework of an ESIS-TC4 round robin test, F. Arbeiter (Montanuniversitaet Leoben) and P. Freudenthaler (Johannes Keppler Universitaet Linz) investigated these test parameters, especially notching procedure and test frequency, with regard to the applicability to HIPS in previous tests (unpublished). Testing at 10 Hz did not show a significant temperature increase in HIPS. Furthermore, the chosen notching procedure led to sharp and reproduceable pre-cracks. Thus, the test parameters presented in chapter 4.1.2 were considered appropriate.

In Figure 29 the number of cycles until failure at different initial stress intensity factors $\Delta K_{I,0}$ are plotted in a double-logarithmic diagram. HIPS A showed higher resistance to fatigue crack growth. Even with the influence of sunflower oil, it could bear greater stresses than HIPS B. For HIPS B, a massive influence of the oil on the number of cycles until failure was observed. A shift of the fitted curve downwards to dramatically lower values for $\Delta K_{I,0}$ was found. Compared to that, values for HIPS A decreased significantly less. This result is reasonable since the ESCR (determined with the Bent Strip Method, ISO 22088-3) is 94 for HIPS A and 26 for HIPS B [27]. For long-term static loads and also in the tensile test, HIPS B performs better than HIPS A when tested in air, showing a greater resistance against crack

growth and also a higher yield stress [27]. A possible explanation, why HIPS A is superior in the cyclic load test when tested in air, could be given by the investigated stress intensity factors, with the maximum initial stress intensity factor at approx. 0.35 MPa. As shown by Andena L. et. al. [27], HIPS A outperforms HIPS B at low applied stress intensity factors under static loading. Additionally, the smaller rubber particles lead to higher notch factors and consequently to higher stress concentration at the interface of the particles and the PS matrix. Solberg et al. [66] found that notches can lead to notch strengthening under quasi-static loading and for testing at low cycle number under fatigue loading, but at higher cycle numbers notch weakening occurs. To verify this claim, further measurements at higher stress intensities are required. Furthermore, in HIPS A there is probably more matrix mass between the larger rubber particles, which must be deformed during each cycle, leading to a greater energy dissipation.
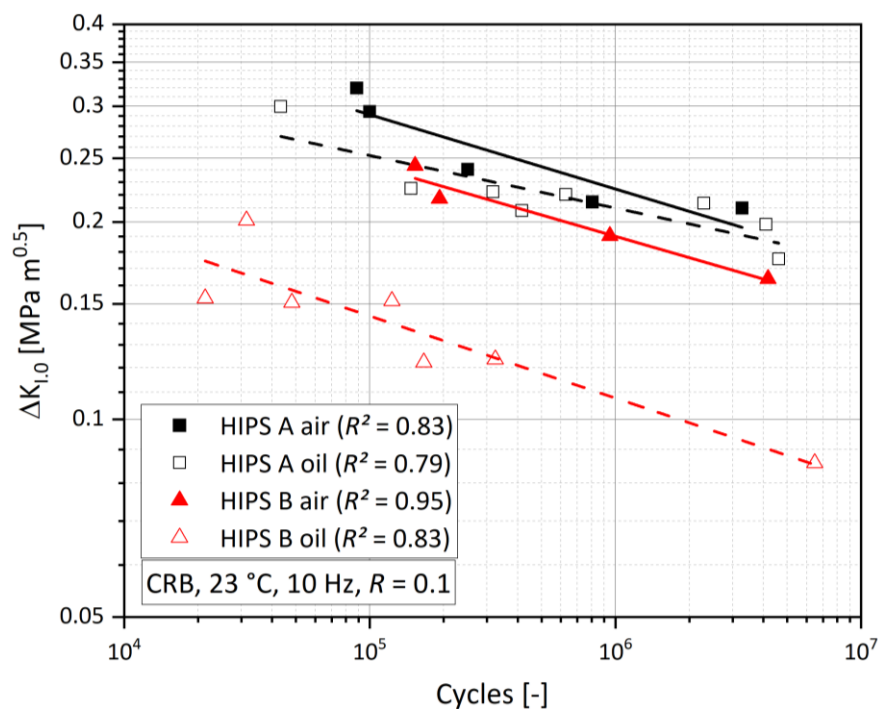


Figure 29: Comparison of the fatigue crack growth in both HIPS A and B at air and in oil.

Further attention must be given to the deviation of the measured points to the regression line. For testing PE in accordance to ISO 18489:2015, the coefficient of determination $R^2$ was found at 0.97-0.99 [64, 67]. As noted in the above figure, $R^2$ was far less satisfactory for HIPS. For this reason, the scope of testing was increased. Due to the rubber particles, the more pronounced inhomogeneity of HIPS compared to PE is possibly responsible for

this behaviour. Moreover, when testing in oil, the quality of the circumferential notch may have a more considerable influence on the crack initiation time since different notch qualities result in different factors of stress concentrations.

The fracture surfaces of the HIPS A specimens are illustrated in Figure 30 and those for HIPS B in Figure 31. Beginning from the initial notch, after blunting, the fracture surfaces are pretty smooth. With increasing crack lengths, the stress intensity rises and after a critical crack length is reached, the remaining cross-section fails in a ductile, highly deformed manner. However, especially for HIPS A specimens tested in oil at low stress intensities, this ductile failure is no longer visible on the fracture surfaces. Furthermore, the cracks did not propagate symmetrically from the outside to the centre for some of the specimens. Literature explains this phenomenon with asymmetries in the specimen, the clamping and the testing machine [55].

**Without oil**     **With oil**



$N$: 884843, $\Delta K_{I.0}$: 0.32     $N$: 43444, $\Delta K_{I.0}$: 0.30     $N$: 146951, $\Delta K_{I.0}$: 0.23

$N$: 99768, $\Delta K_{I.0}$: 0.30     $N$: 316765, $\Delta K_{I.0}$: 0.22     $N$: 416454, $\Delta K_{I.0}$: 0.21

$N$: 250453, $\Delta K_{I.0}$: 0.24     $N$: 627827, $\Delta K_{I.0}$: 0.22     $N$: 2292809, $\Delta K_{I.0}$: 0.21

$N$: 804485, $\Delta K_{I.0}$: 0.15     $N$: 4099144, $\Delta K_{I.0}$: 0.20     $N$: 4626221, $\Delta K_{I.0}$: 0.17
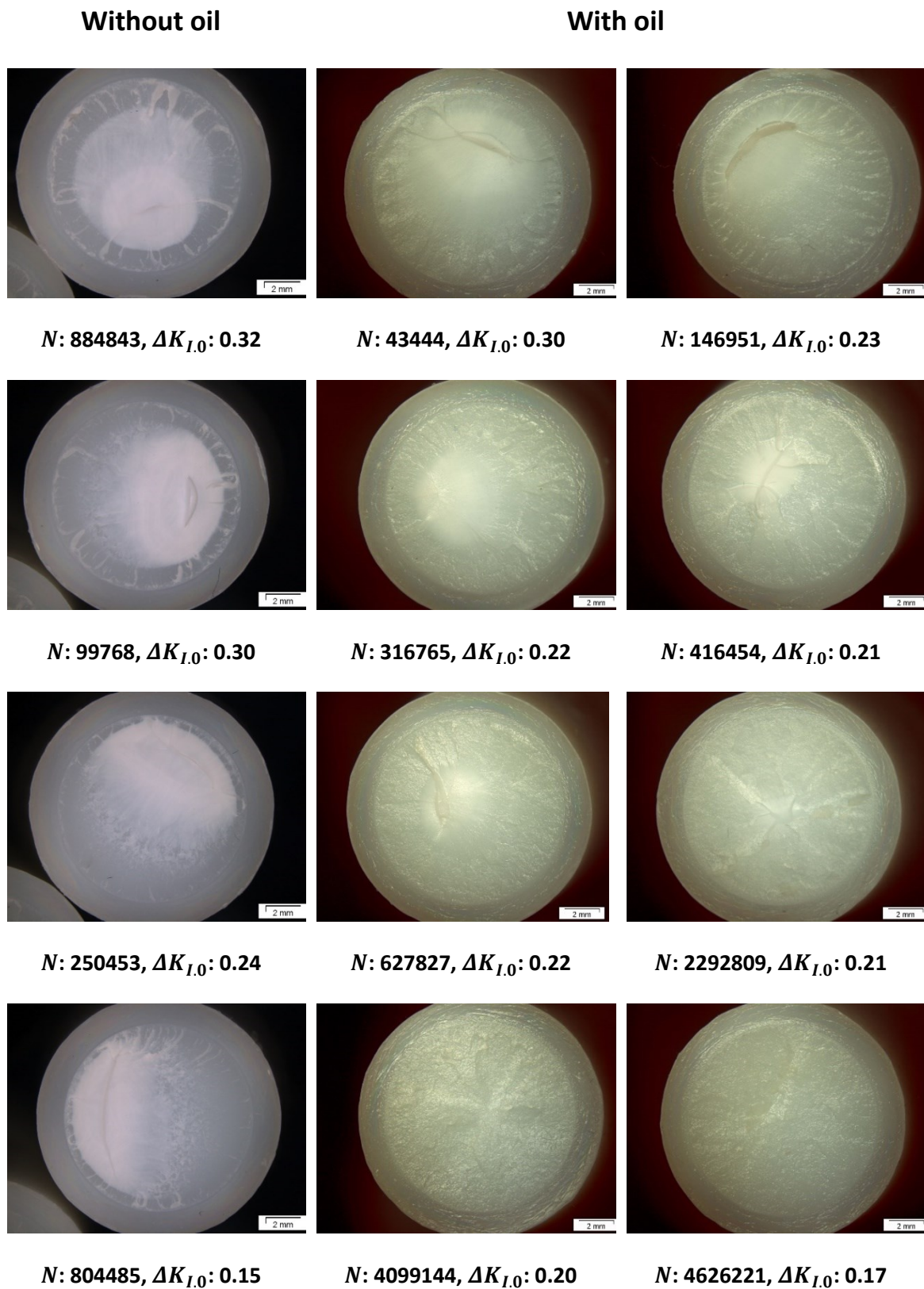
Figure 30: Fracture surfaces of the HIPS A CRB specimens tested in air and in oil with the number of cycles to failure and the initial stress intensity factors in MPa.

**Without oil**　　　　　　　**With oil**



$N$: 153041, $\Delta K_{I.0}$: 0.24　　$N$: 21380, $\Delta K_{I.0}$: 0.15　　$N$: 31505, $\Delta K_{I.0}$: 0.20



$N$: 192215, $\Delta K_{I.0}$: 0.22　　$N$: 48184, $\Delta K_{I.0}$: 0.15　　$N$: 123180, $\Delta K_{I.0}$: 0.16



$N$: 949070, $\Delta K_{I.0}$: 0.19　　$N$: 165889, $\Delta K_{I.0}$: 0.12　　$N$: 324121, $\Delta K_{I.0}$: 0.12



$N$: 4180989, $\Delta K_{I.0}$: 0.16　　$N$: 6479297, $\Delta K_{I.0}$:  0.09
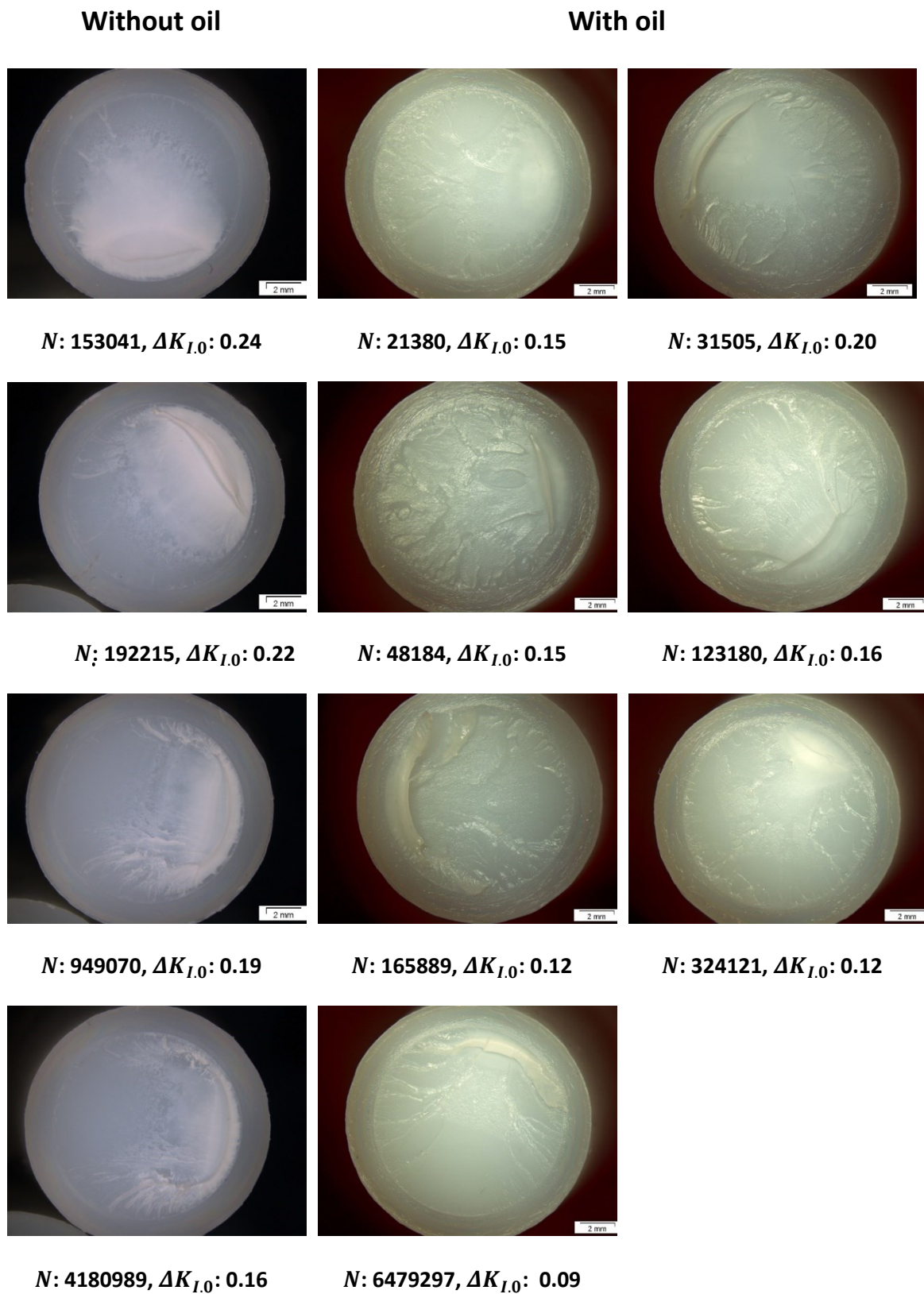
Figure 31: Fracture surfaces of the HIPS B CRB specimens tested in air and in oil with the number of cycles to failure and the initial stress intensity factors in MPa.

## 5.1.2 Static load test

At first, CT specimens with side grooves were investigated. These side grooves made the detection of the crack tip more difficult because the crack front at the front and back side of the specimen was at different positions. Moreover, the crack did not run exactly straight forward but fluctuated up and down (Figure 32). Furthermore, surface defects (higher roughness) supported additional crack initiations (Figure 33 a). By increasing the surface quality of the side grooves by using a diamond saw blade, this problem was reduced (Figure 33 b). Due to this reworking, the radius of the side grooves changed to 1.5 mm. However, also without side grooves, the crack propagated straight forward in air. When tested in oil, cracks propagated even flatter than with side groves. Hence, the subsequent measurements were conducted without side grooves.



Figure 32: Front side of a HIPS B CT specimen with side grooves tested in oil.
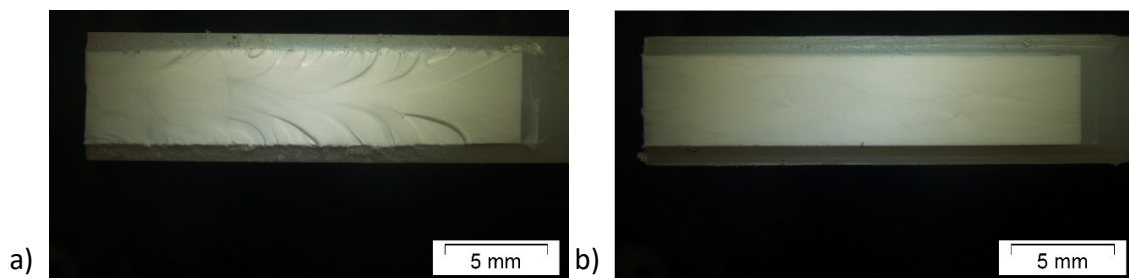


Figure 33: Fracture surfaces of HIPS A CT specimens with side grooves tested in air: a) bad surface quality and b) good surface quality.

As a result of the recording rate of the camera, fewer images were available for the crack length evaluation at higher $K_I$ values and thus higher crack growth rates. In order to generate more data points, a calibration was performed for the measurements with higher $K_{I,0}$ using the crosshead displacement of the testing machine. The measured crack lengths were plotted over the crosshead displacement (Figure 34). By fitting this correlation, the

crack length could be calculated as a function of the crosshead displacement and consequently, more data points were available (Figure 35).
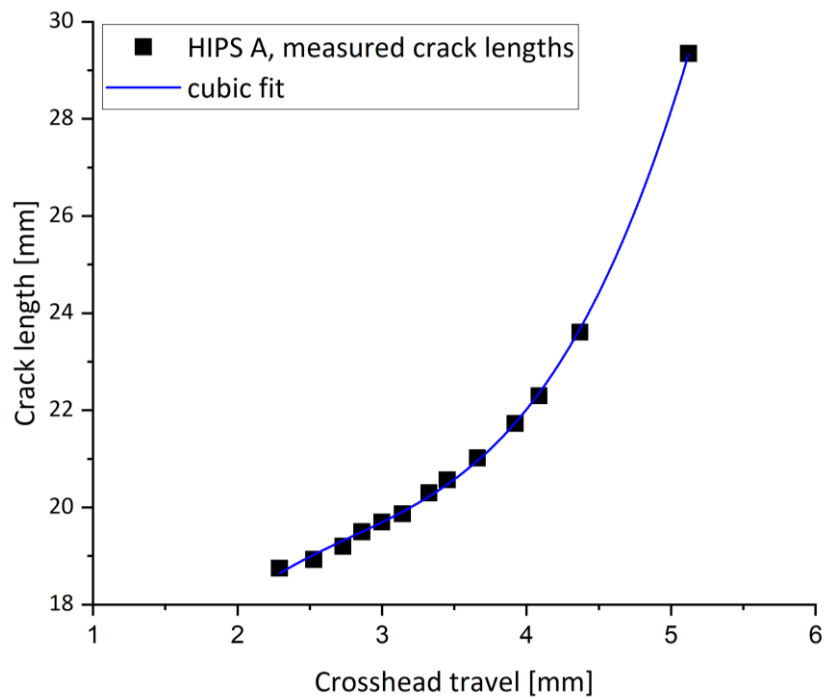


Figure 34: Illustration of the calibration of the crack length over the crosshead travel for HIPS A.
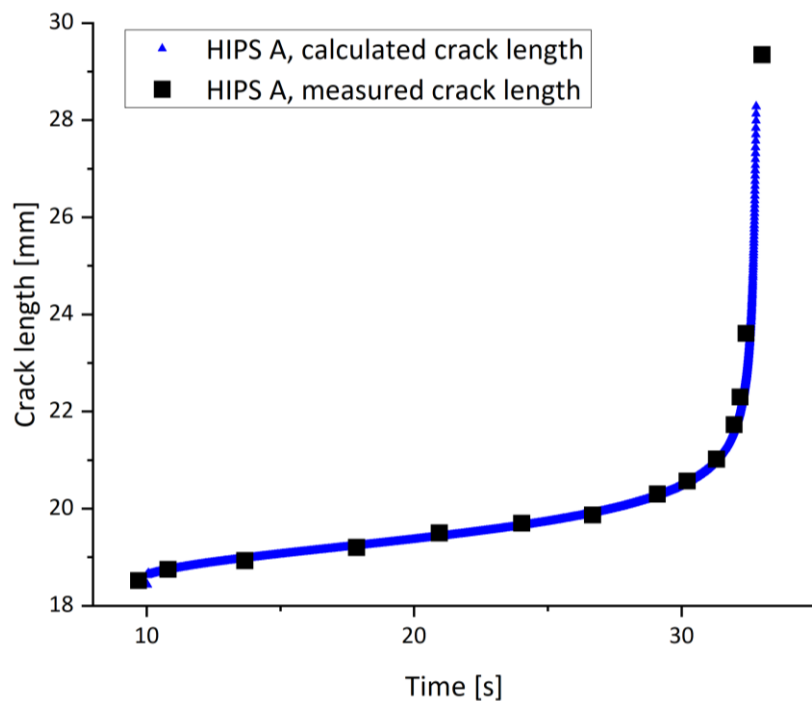


Figure 35: Crack length as a function of the time with measured and calculated data points for HIPS A.

In Figure 36, the crack growth kinetic curves for HIPS A and in Figure 37 for HIPS B compare the crack propagation in air and in the active medium. Both, data points generated from manually measured crack lengths as well as from crack lengths calculated with the calibration, are presented. A sufficient correlation between both evaluation methods is given. Obviously, HIPS A and B have a greater crack growth resistance when tested in air. The presence of the oil shifts the crack growth to lower $K_I$ values as a consequence of ESC. However, at a certain $K_I$ value, the curves for testing in oil show a kink and the trend of the curves is then similar to those for testing in air. Consequently, at these crack growth rates, no influence of the active medium is given. Williams J. G. and Marshall G. P. [68] described this behaviour in more detail using a simple fluid flow model. They divided the crack growth in the environment of an active medium into two areas, the relaxation controlled (area I) and the fluid flow controlled (area II) one. At a specific crack growth rate, the time span is too short and the fluid flow to the crack tip cannot be maintained. Hence, the craze at the crack tip is deprived of the medium.
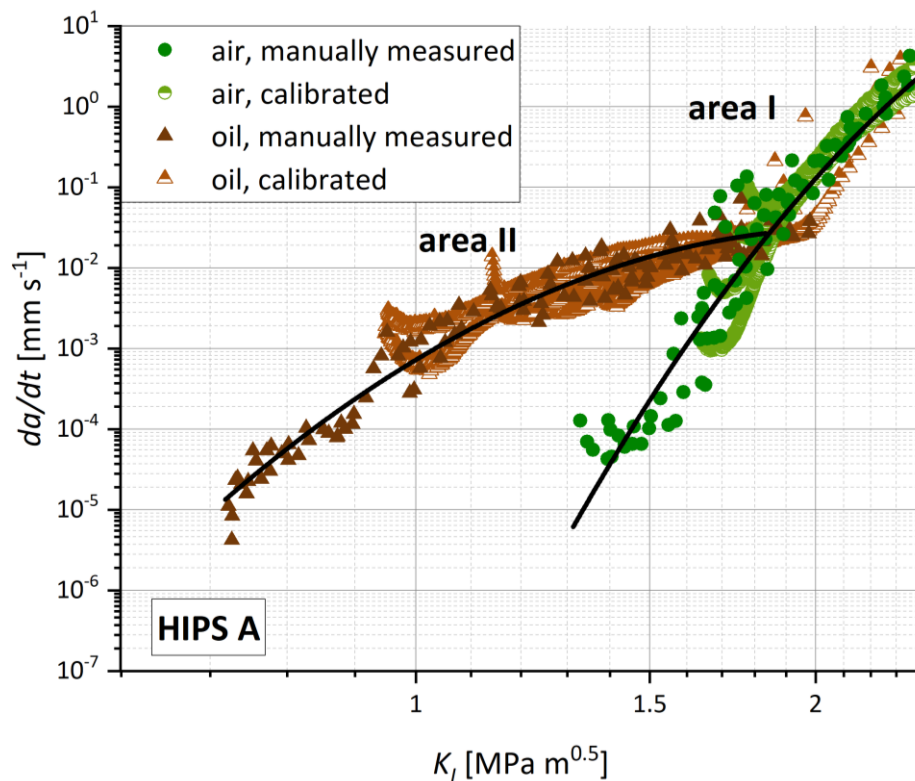


Figure 36: Crack growth kinetic curves for HIPS A tested in air and in oil.
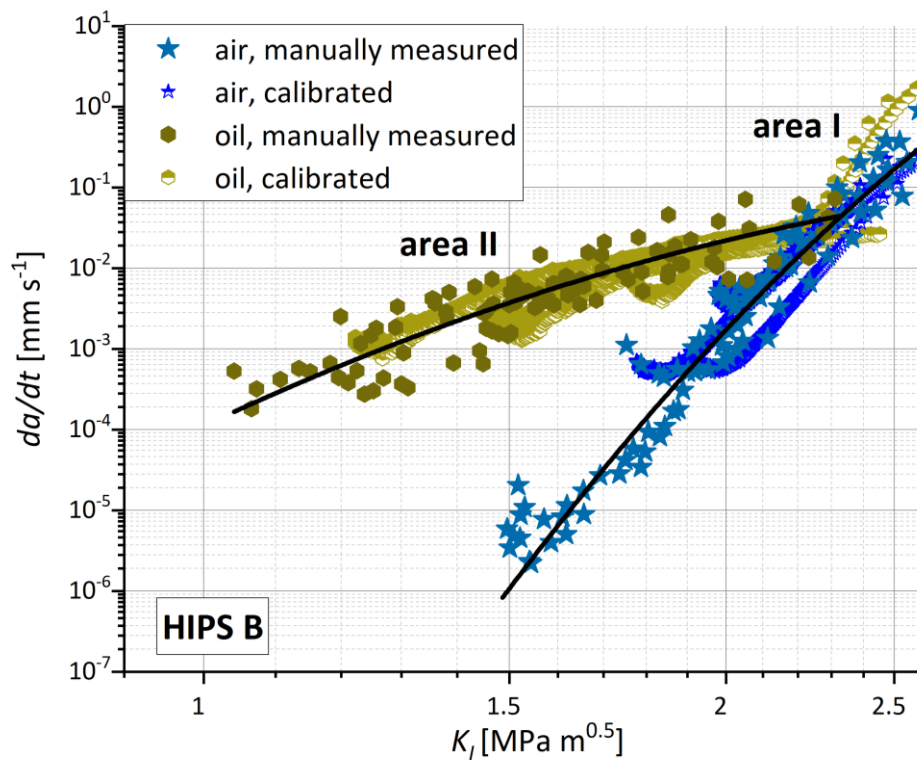
Figure 37: Crack growth kinetic curves for HIPS B tested in air and in oil.

The influence of the active medium is also demonstrated on the fracture surfaces (Figure 38 – HIPS A and Figure 39 – HIPS B). The specimens tested in air show smooth fracture surfaces with no visible deformations. In contrast to that, the oil led to far more distorted fracture surfaces. Moreover, this effect is more pronounced for HIPS B. For testing in oil, the fracture surfaces show two different areas. Starting from the pre-crack, the surface is quite rough. With increasing crack length, the surface changes abruptly. It looks much smoother and more similar to the fracture surfaces of the specimens tested in air. Hence, it can be assumed that this switchover can be attributed to the kink in the crack kinetic curves, where no interaction between the medium and the polymer occurs (Figure 40 a). Especially for HIPS B, the oil diffuses not only from the pre-crack into the material, but also from the side surfaces of the specimen (Figure 40 b). The non-interaction zone is then limited to the inner area of the specimen.

**Without oil**                    **With oil**



$t_B$: 29140, $K_{I.0}$: 1.35          $t_B$: 96418, $K_{I.0}$: 0.75

$t_B$: 21073, $K_{I.0}$: 1.38          $t_B$: 48754, $K_{I.0}$: 0.80

$t_B$: 1215, $K_{I.0}$: 1.53          $t_B$: 1669, $K_{I.0}$: 1.00

$t_B$: 237, $K_{I.0}$: 1.64          $t_B$: 3440, $K_{I.0}$: 1.00

$t_B$: 70, $K_{I.0}$: 1.71          $t_B$: 443, $K_{I.0}$: 1.36

$t_B$: 33, $K_{I.0}$: 1.79          $t_B$: 443, $K_{I.0}$: 1.36
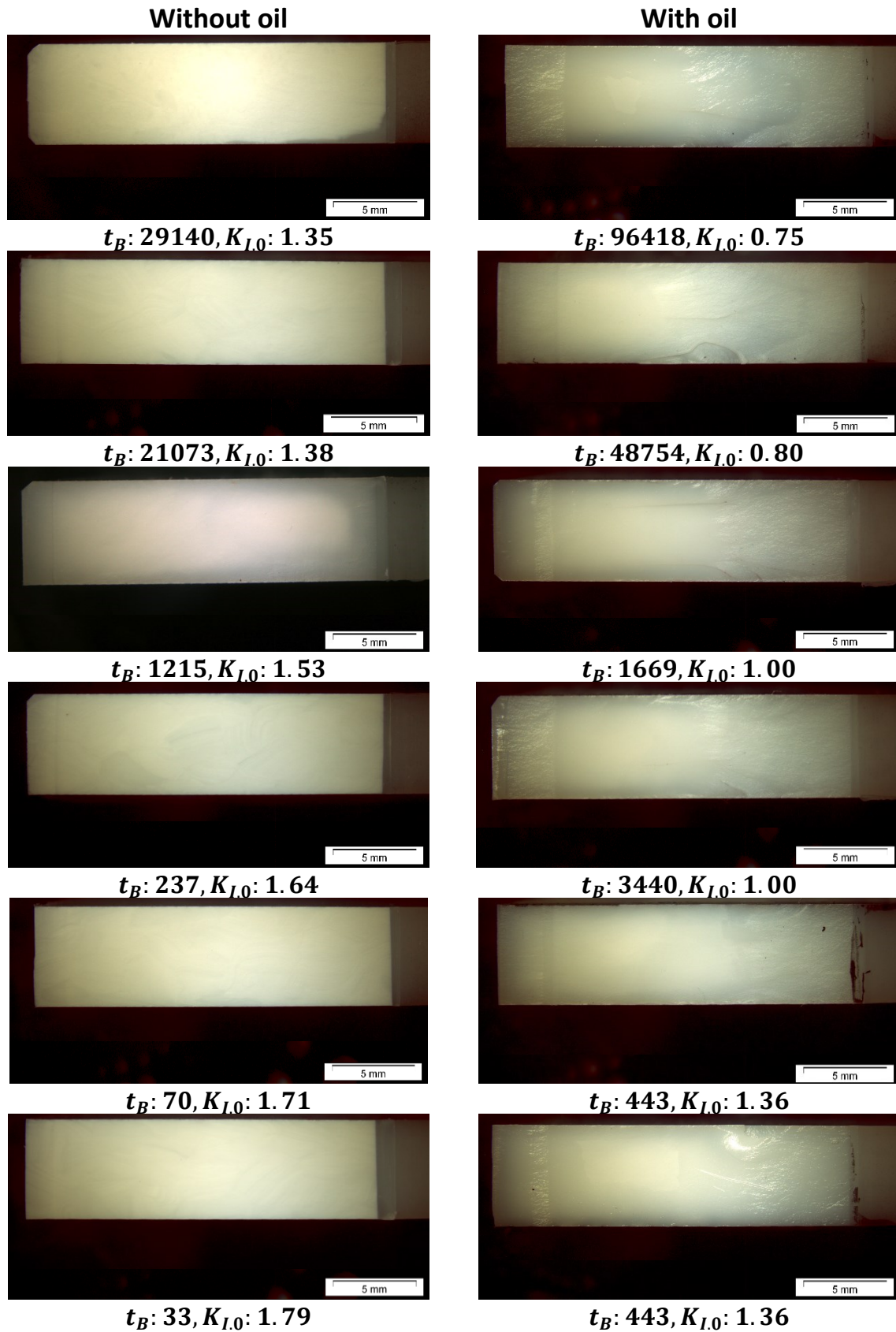
Figure 38: Fracture surfaces of the HIPS A CT specimens tested in air and in oil with the fracture time in s and the initial stress intensity factors in MPa.

**Without oil**     **With oil**



$t_B$: 443484, $K_{I.0}$: 1.49     $t_B$: 10354, $K_{I.0}$: 1.00

$t_B$: 186627, $K_{I.0}$: 1.57     $t_B$: 8526, $K_{I.0}$: 1.00

$t_B$: 2903, $K_{I.0}$: 1.76     $t_B$: 1531, $K_{I.0}$: 1.20

$t_B$: 2335, $K_{I.0}$: 1.86     $t_B$: 1388, $K_{I.0}$: 1.26

$t_B$: 367, $K_{I.0}$: 2.00     $t_B$: 494, $K_{I.0}$: 1.50

$t_B$: 304, $K_{I.0}$: 2.00     $t_B$: 401, $K_{I.0}$: 1.52
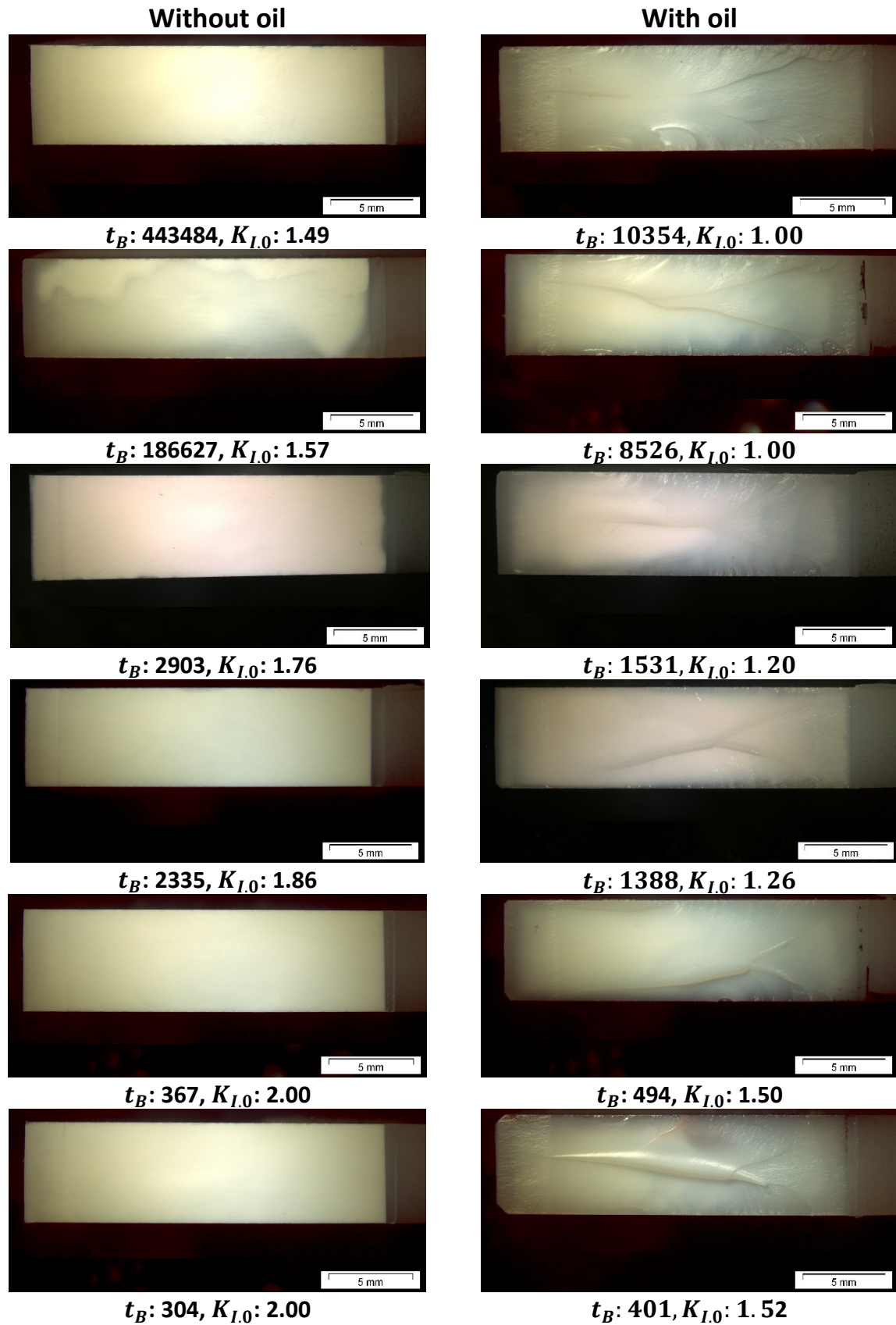
Figure 39: Fracture surfaces of the HIPS B CT specimens tested in air and in oil with the fracture time in s and the initial stress intensity factors in MPa.
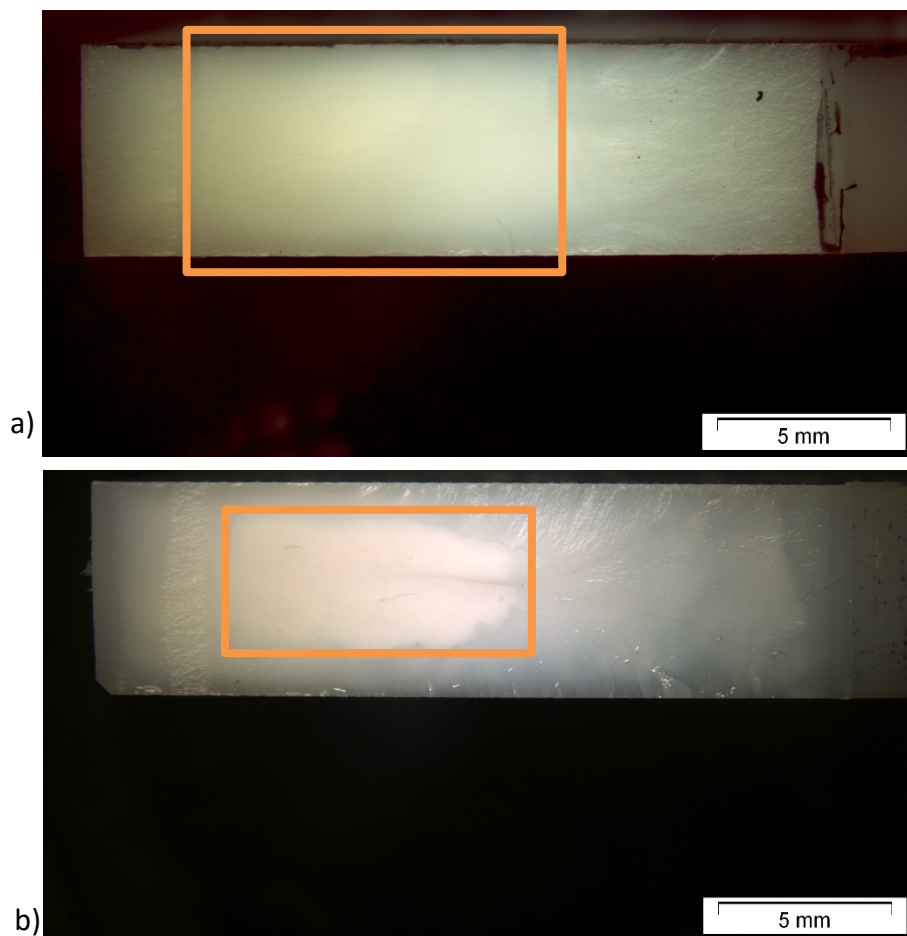
Figure 40: Fracture surfaces of two CT specimens tested in oil with the inserted rectangle marking the non-interaction zone in a) HIPS A and b) HIPS B.

In Figure 41, a comparison of HIPS A and B's crack growth kinetic curves is given. HIPS B outperforms HIPS A regarding crack growth resistance. Especially when testing in air, HIPS B is superior. At lower $K_I$ values, the gap between HIPS A and B tested in oil is smaller, however HIPS A performs still worse than HIPS B, even though it is the special designed ESCR grade.
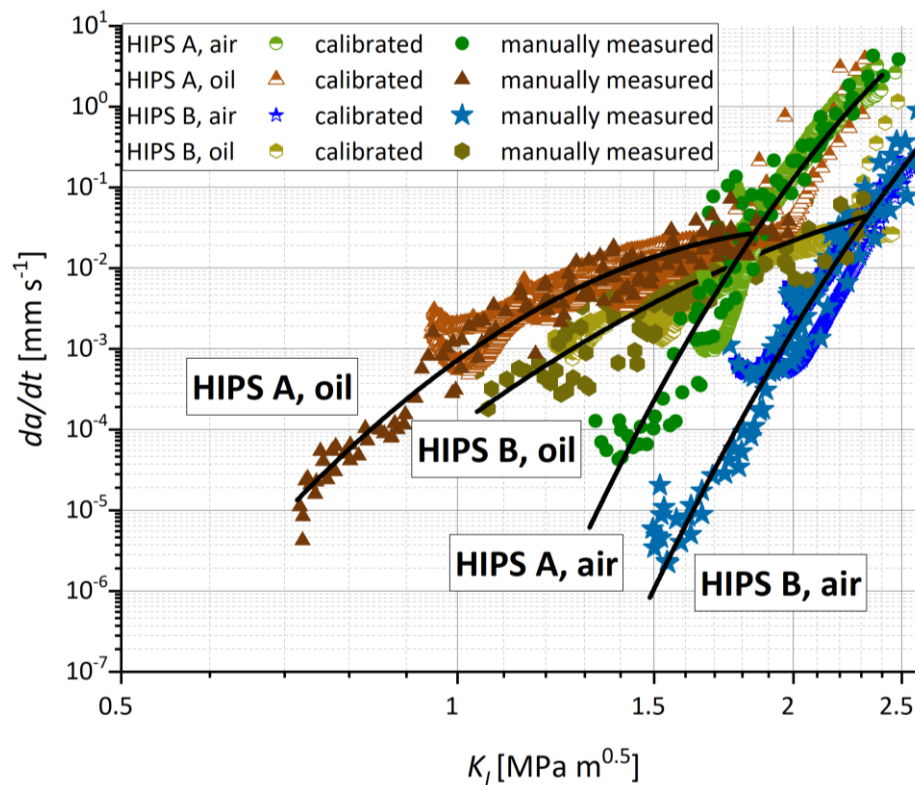
Figure 41: Comparison of the crack growth kinetic curves for HIPS A and B tested in air and in oil. Similar behaviour for the same HIPS grades from this thesis was found by Andena L. et al. [27]. HIPS B showed a higher crack growth resistance as well. However, they found that with decreasing loads and hence longer testing times, the influence of the oil became more significant for HIPS B. For stress intensity factors below 1 MPa m$^{0.5}$ HIPS A was tougher when tested in oil. This crossover between HIPS A and B at lower loads in oil was not found in this thesis because testing HIPS B in oil at $K_{I,0}$ below 1 MPa was not possible, as after some time, the cracks started to initiate and propagate at the corners of the V-notch, instead of the razor blade induced notch. Moreover, a different evaluation method was used in contrast to Andena L. et al.. Whereas in this thesis the crack growth was tracked optically, they evaluated the crack growth by a compliance calibration [27]. The problem with crack growth measurement is discussed in more detail in the next paragraph.

Especially the results of HIPS B in oil show great scattering. This is because of the problematic crack tip detection caused by ESC. The sunflower oil creates multiple crack initiations across the specimen's width and different propagation rates of these cracks. Hence, determining the crack tip optically is very subjective. In Figure 42 the front side of a HIPS B specimen tested in oil is shown. The huge gap between the crack tip on the surface

in the front and on inside of the specimen in the back is demonstrated. The fracture surface of this specimen (Figure 43) shows the complicated crack growth across the cross-section. At the front, where the interaction between the polymer and the oil is possible immediately, the crack is much further ahead than in the centre of the specimen.
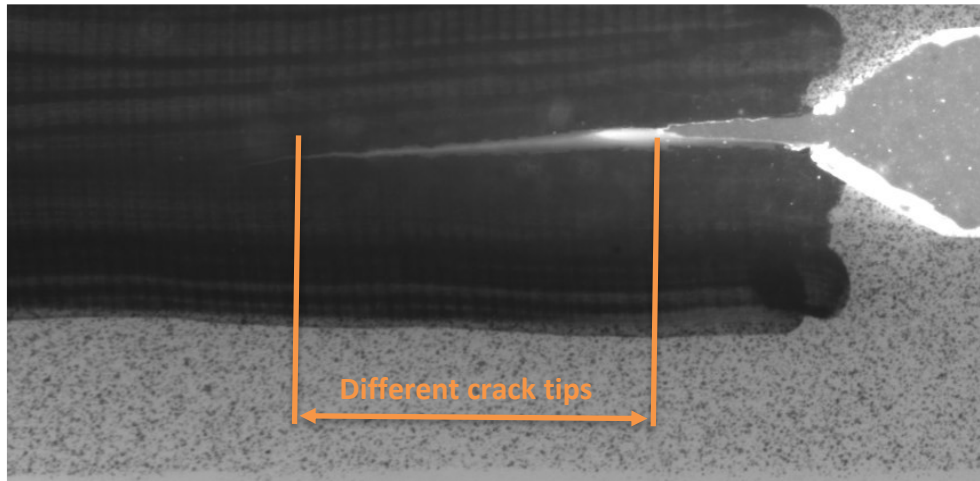


Figure 42: Different crack tips in HIPS B when tested in oil.



Figure 43: Fracture surface of a HIPS B CT specimen tested in oil.

The above specimen was evaluated in two ways to investigate the influence of the crack tip detection in more detail. At first, the forefront crack tip was chosen for measuring the crack length. Secondly, the rearmost crack tip, where the whole cross-section has been opened, was used. In Figure 44, the crack growth kinetics is shown for both variants. For reference, the fitted crack growth curves from Figure 37 are depicted. It can be seen that when using the forefront tip, the material's toughness is overestimated because the greater crack lengths result in higher values for $K_I$. On the contrary, the rearmost tip

underestimates the material, and the curve is shifted to lower values for $K_I$. Hence it is crucial to analyse the obtained results critically. For curve I, it makes no sense that the material prone to ESC, shows a higher fracture resistance when exposed to the oil than when tested in air. The course of curve II fits the obtained trend quite well at the beginning of the crack growth. However, at larger crack lengths, the slope of the curve increases too early. As described before, the kink characterises the crack growth rate where no interaction between the polymer and the oil occurs. Therefore, in the area of these stress intensity factors, the curve must follow the trend of the specimens tested in air. The actual curve thus will lie in between curves I and II. Moreover, as was demonstrated in Figure 40, p.52), also the assumed constant width of the ligament is false for some of the tests. Due to the additional crack growth from the side surfaces of the specimen, the effective $B$ decreases as the crack grows. To obtain the correct crack kinetics curves for testing in oil, probably the determination of the averaged crack front over the specimen's width and the effective width as a function of crack length are necessary.
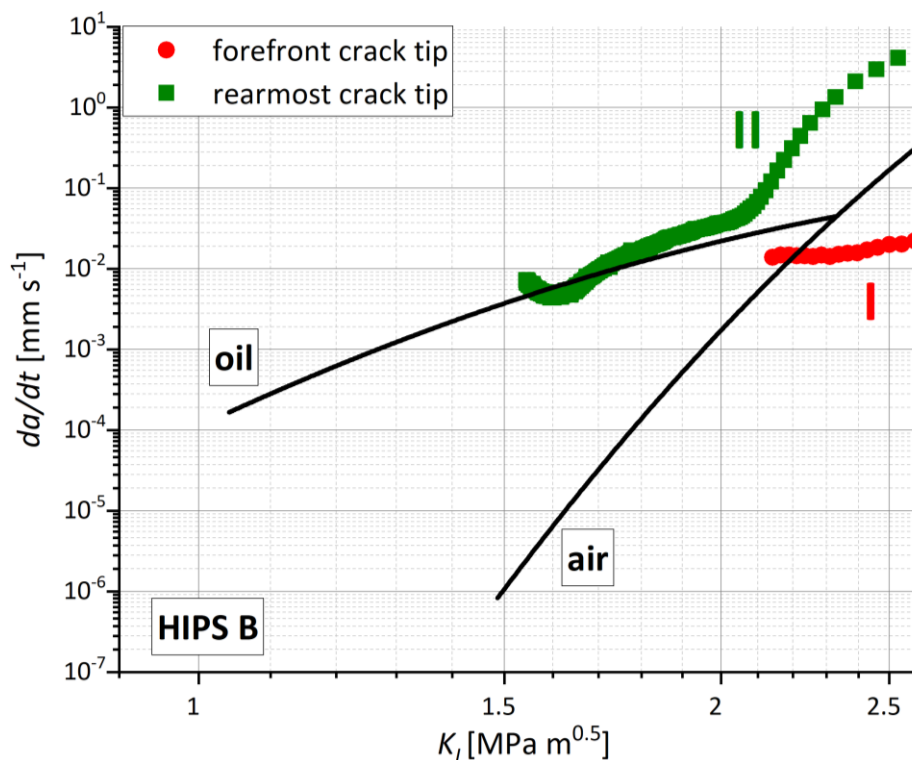


Figure 44: Investigation of the influence of the crack tip detection between foremost and rearmost crack tip.

To check if the superiority of HIPS B in crack growth resistance is only due to aforementioned difficulties of measurement, also the total time to failure was examined

for the CT specimens. The initial stress intensity factors were plotted over the time to failure (Figure 45). It can be seen that HIPS B performs only slightly better than HIPS A under the influence of oil. As the slope of HIPS B in oil is steeper, a cross-over point can be expected. This would be in accordance with the real application, where at low stress intensity HIPS A outperforms HIPS B [27].
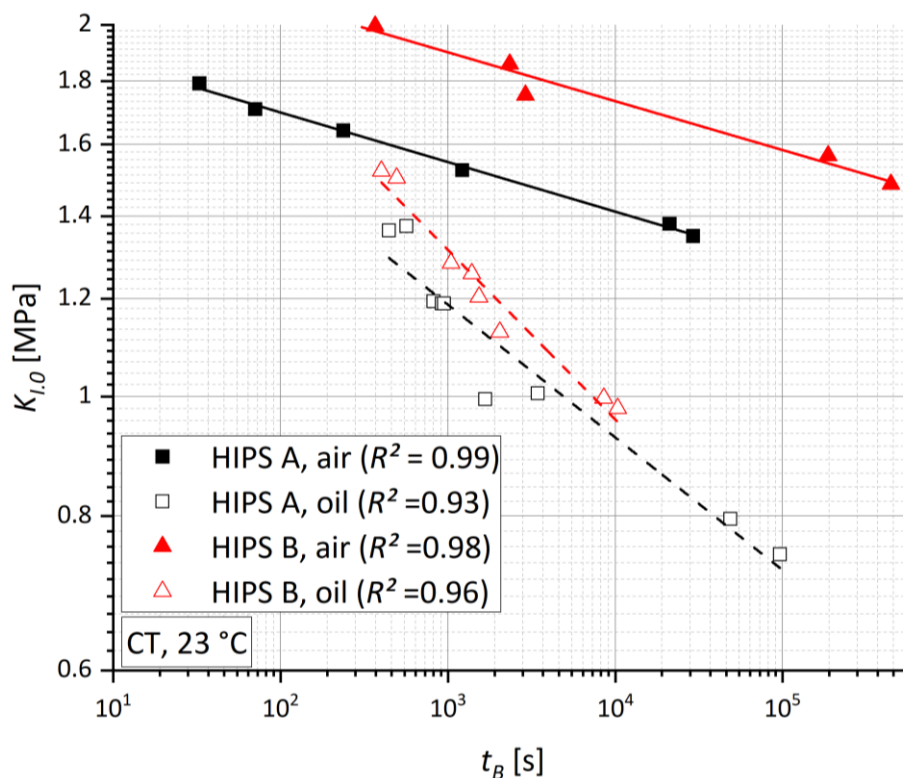


Figure 45: Initial stress intensity factors as a function of fracture time for HIPS A and B tested at air and in oil.

To understand why the gap between HIPS A and HIPS B decreases when ESC occurs, a closer look at the morphology of the two HIPS types must be taken. V. G. Grassi et al. [38] investigated the ESCR of different HIPS grades. They found that the rubber particle size, the molecular weight ($M_w$) of the PS and the PB content are the critical parameters for optimising ESCR in HIPS. To obtain the highest possible ESCR, a good balance between $M_w$ and RPS must be found. A high $M_w$ stabilises the craze growth, however, it also hinders the rubber particle growth due to higher viscosity. Hence, a medium $M_w$ with a higher PB content, leading to larger RPS, showed the greatest ESCR [38]. R. A. Bubeck et al. [40] also studied the ESC behaviour of HIPS. They found the same correlation between $M_w$, RPS and ESCR. Their explanation for this result is, that the larger rubber particles nucleate and grow

crazes with a higher fibril volume fraction with fewer voids, which hampers the flow of the medium to the crack tip. A possible explanation from the authors is, that a larger rubber particle creates more crazes within the deformed zone. Hence, the given strain is distributed to more crazes. Consequently, the craze fibril structure gets drawn and thinned out less than when the strain would be accommodated by fewer crazes.

In Figure 46, the craze formation for HIPS B in the CT specimens is illustrated. It can be seen that multiple crazes, oriented in different directions, are formed when testing in air. In oil, nearly no deformation zones can be seen in front of the crack tip. Probably due to the quick disentanglement of the polymer chains in oil, no or only small plastic zones arise. Although the size of the zone with plastic deformation appears quite large, Andena L. et al. verified the applicability of LEFM on these HIPS grades, as they observed the same toughness when applying LEFM to different specimen types (single-edge notched bending, double cantilever beam and buckled plate) [27].
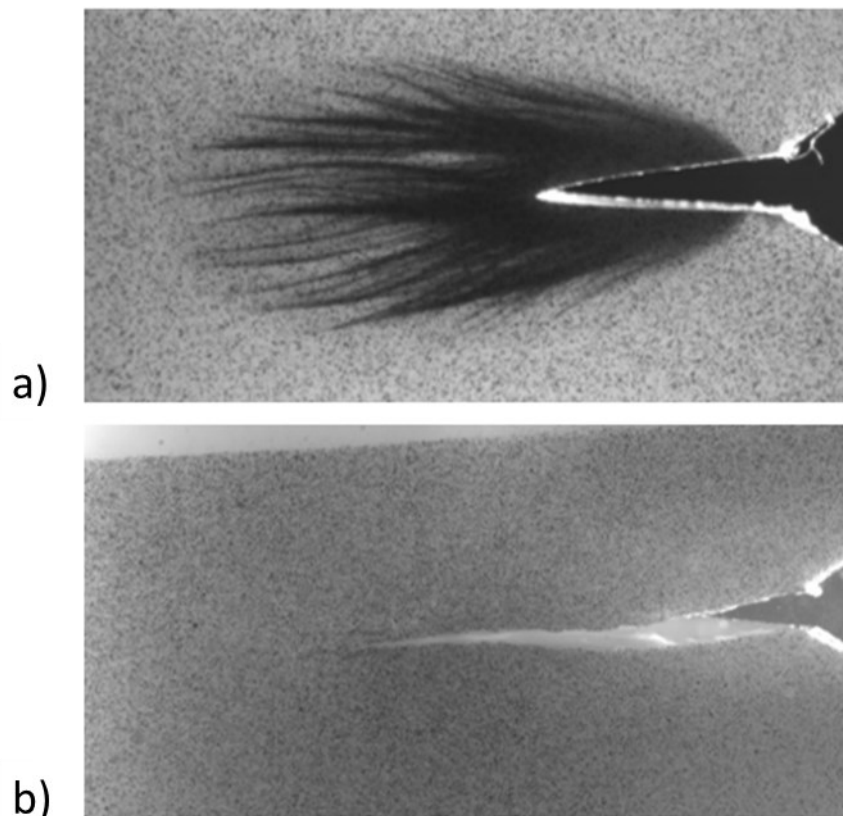


Figure 46: Craze formations in HIPS B a) in air and b) in oil.

## 5.2　Influence of PBS on PCU

### 5.2.1　Conditioning

Figure 47 shows the relative change in mass of the Bionate® 75D and 80A specimens during both drying and storing. The relative change in mass was related to the mass after the drying process, which corresponds to time zero in the diagram. Consequently, the measuring points in the area of the negative time scale correspond to the drying process; those on the positive time scale to the storing in PBS. The values presented were calculated as the mean and standard deviation of five specimens.
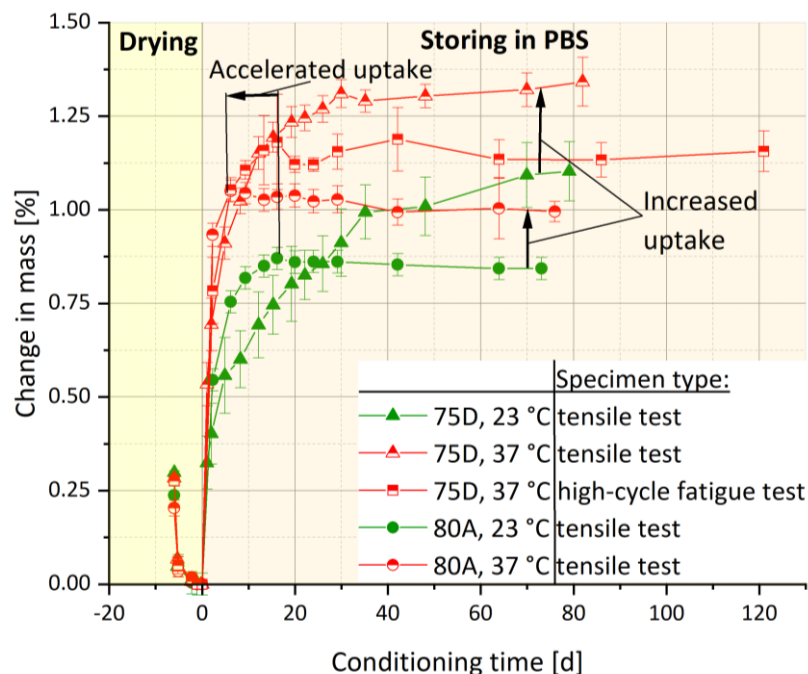


Figure 47: Change in mass for drying and storing of multipurpose specimens.

The evaluation clearly shows that the elevated temperature of 37 °C leads to an increased and faster uptake of the PBS solution. Looking at Bionate® 80A, the saturation point is already reached after 6 days at 37 °C, whereas at 23 °C it is only reached after 16 days. However, after reaching saturation, Bionate® 80A shows a minimal decrease in mass. One explanation could be degradation of the polymer, followed by diffusion of the thereby formed polymer chain fragments into the PBS solution. Mishra A. et al. [44] investigated the degradation behaviour of several thermoplastic urethanes. Amongst them, they analysed Bionate® 55D in a PBS and a nitrogen environment at different temperatures.

They found that thermal degradation and hydrolysis take place. The molecular weight decreased around 50 % during storing the specimen for one year in the PBS environment at 80 °C and around 10 % at 37 °C. By storing the specimen at 80 °C under a nitrogen atmosphere, $M_w$ decreased around 25 %. Hence, the authors observed that at 80 °C, half of the change of $M_w$ is attributed to thermal degradation. The thermal degradation for PCU is a two-step process. At first, the hard segments' carbamate bonds (N–COOH) degrade, forming isocyanate, alcohol, amines, olefins and carbon dioxide. Secondly, the soft segments can also decompose, whereas this step is considered much slower [44, 69]. For the second phenomenon, hydrolysis, the presence of water molecules can split the polymer chains into two parts. This process is illustrated for the hydrolysis of carbonate (Figure 48) [70]. Furthermore, the literature states, that a higher degree of hard segments leads to less hydrolytic degradation [71].
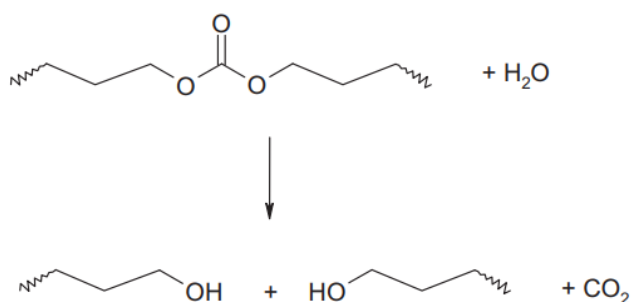


Figure 48: Illustration of the hydrolysis of a carbonate group [70].

Regarding Bionate® 75D, the specimens for tensile testing show still a small increase in mass after 80 days. However, looking at the slope of the curves, the samples should be close to the saturation point. The thinner specimens for the high-cycle fatigue tests reached saturation after 16 days. Furthermore, Bionate® 80A was found to absorb less PBS than Bionate® 75D. Since higher saturation concentrations were measured for 75D than 80A, it can be concluded that the harder polyurethane segments absorb more PBS than the soft polycarbonate segments. Similar results were obtained by Mishra A. et al. [44]. An explanation for this result could be the different content of hard and soft segments in Bionate® 75D and 80A and hence the different solubility parameters. For the hard segment consisting of methylene di(p-phenyl isocyanate) and 1,4-butanediol, $\delta$ is 23.92 $J^{1/2}$ cm$^{-3/2}$ [72]. For the soft segment consisting of polycarbonate, $\delta$ is 19.1 $J^{1/2}$ cm$^{-3/2}$ [3]. For distilled water, $\delta$ is 47.9 $J^{1/2}$ cm$^{-3/2}$ [3]. Assuming that the solubility of PBS is similar to that of water,

it can be concluded that the hard segments are more likely to absorb greater amounts of the PBS solution.

Using equation (7) from chapter 2.1.2, the diffusion coefficients were determined. Table 4 lists the results for the saturation concentrations and diffusion coefficients. The diffusion coefficients underline the results discussed above with the highest obtained values at 37 °C. The obtained results correlate well with those from other studies [13, 18].

Table 4: Saturation concentration and diffusion coefficient for the Bionate® specimens stored in PBS.

| Specimen type and condition | | Saturation concentration [%] | Diffusion coefficient [$10^{-12}$ m² s$^{-1}$] |
|---|---|---|---|
| Tensile test | 75D, 23 °C | 1.11 | 3.04 |
| | 75D, 37 °C | 1.34 | 5.39 |
| | 80A, 23 °C | 0.87 | 6.33 |
| | 80A, 37 °C | 1.05 | 12.6 |
| High-cycle fatigue test | 75D, 37 °C | 1.19 | 1.86 |

## 5.2.2 Tensile tests

Figure 49 shows one representative stress-strain curve for each Bionate® type, temperature and conditioning condition. The diagram demonstrates the difference between Bionate® 75D and 80A, with 80A showing significantly greater strains at break and smaller stiffness and tensile strength than 75D. The S-shaped curves for Bionate® 80A are characteristic for thermoplastic polymers at temperatures above the glass transition temperature and for rubbers, which is in good accordance to the greater amount soft PC segments in 80A [3]. The stress-strain curves of Bionate® 75D reflect the much stiffer behaviour.
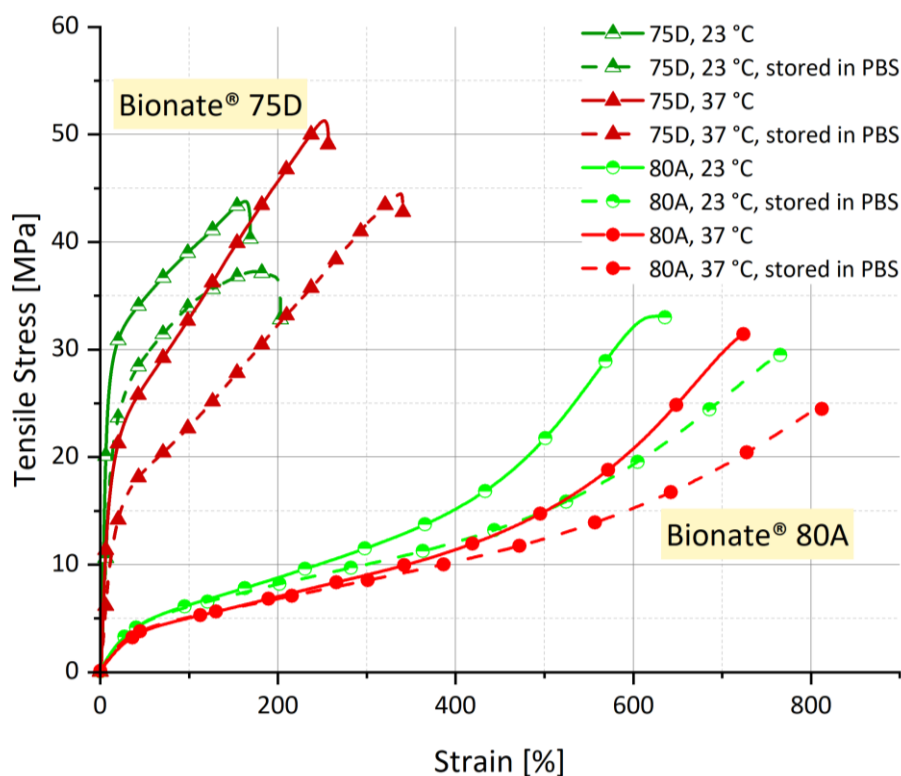
Figure 49: Representative stress-strain curves for both materials and all test conditions.

Figure 50 compares the Young's modulus, tensile strength strain at break and Poisson's ratio as the arithmetic mean of five specimens. Furthermore, the standard deviation is depicted in this figure. The exact values for these mechanical properties are listed in the appendix (A3). For Bionate® 80A, the higher temperature and the storage in PBS resulted in a slight decrease in tensile strength and an increase in strain at break. The tensile strength decreased by 5 % due to elevated temperature, by 10 % due to storing in PBS and by 23 % due to the combined effect of temperature and storage. The elongation at break increased by 15 % due to elevated temperature, by 19 % due to storing in PBS and by 28 % due to the combined effect. For the Young's modulus, no significant changes were observed. The higher temperature and the absorbed PBS increase the flexibility of the polymer chains, resulting in a plasticisation effect. This phenomenon has been observed in several studies [13, 73]. Moreover, the possibility of degradation could also contribute to the changes in the tensile behaviour. Studies verified that lower molecular weights decrease the tensile strength [74, 75]. The molecular weight correlates with the density of chain entanglements, which serve as physical crosslinks. Hence, degradation and consequently lower molecular weights result in a smaller resistance against chain

disentanglement [74, 76, 77]. The Poisson's ratio was determined close to 0.5; elevated temperature and storing in PBS did not lead to significant changes. For Bionate® 75D, the tensile strength increased by 15 % due to elevated temperature but decreased by 14 % due to storing in PBS and by 3 % due to the combined effect of temperature and storage. An explanation for the increase in tensile strength at 37 °C could be the increased chain mobility. Geary C. et al. [41] found that the $T_g$ for Bionate® 75D is approx. 76 °C for injection moulded specimens. Hence, when testing at 37 °C, and consequently at a temperature closer to $T_g$, the polymer chains can possible rearrange faster and more efficiently in the direction of the testing force, leading to higher tensile strengths. However, detailed studies of the morphology are needed to better understand the behaviour at different temperatures. The elongation at break increased by 47 % due to temperature, by 16 % due to storing in PBS and by 87 % due to the combined effect. In contrast to Bionate® 80A, significant changes were observed for the Young's modulus of Bionate® 75D. It decreased by 56 % due to temperature, by 3 % due to storing in PBS and by 63 % due to the combined effect of temperature and storage. The Poisson's ratio at air is notably lower than for Bionate® 80A, with values around 0.4. Nic An Ghaill and Little [78] determined the Poisson's ratio for both materials on injection moulded specimens in a cyclic compression test at 37.5 °C. For the first loading cycle, the Poisson's ratio for Bionate® 80A was determined with 0.49 and for Bionate® 75D with 0.43. These results correlate well with those calculated within this thesis. Moreover, the storing in PBS increased the Poisson's ratio of Bionate® 75D. This behaviour correlates with literature [79, 80]. A possible explanation for this phenomenon can be the almost incompressibility of the absorbed medium or the shift of the glass transition temperature to lower temperatures due to plasticisation [80, 81].
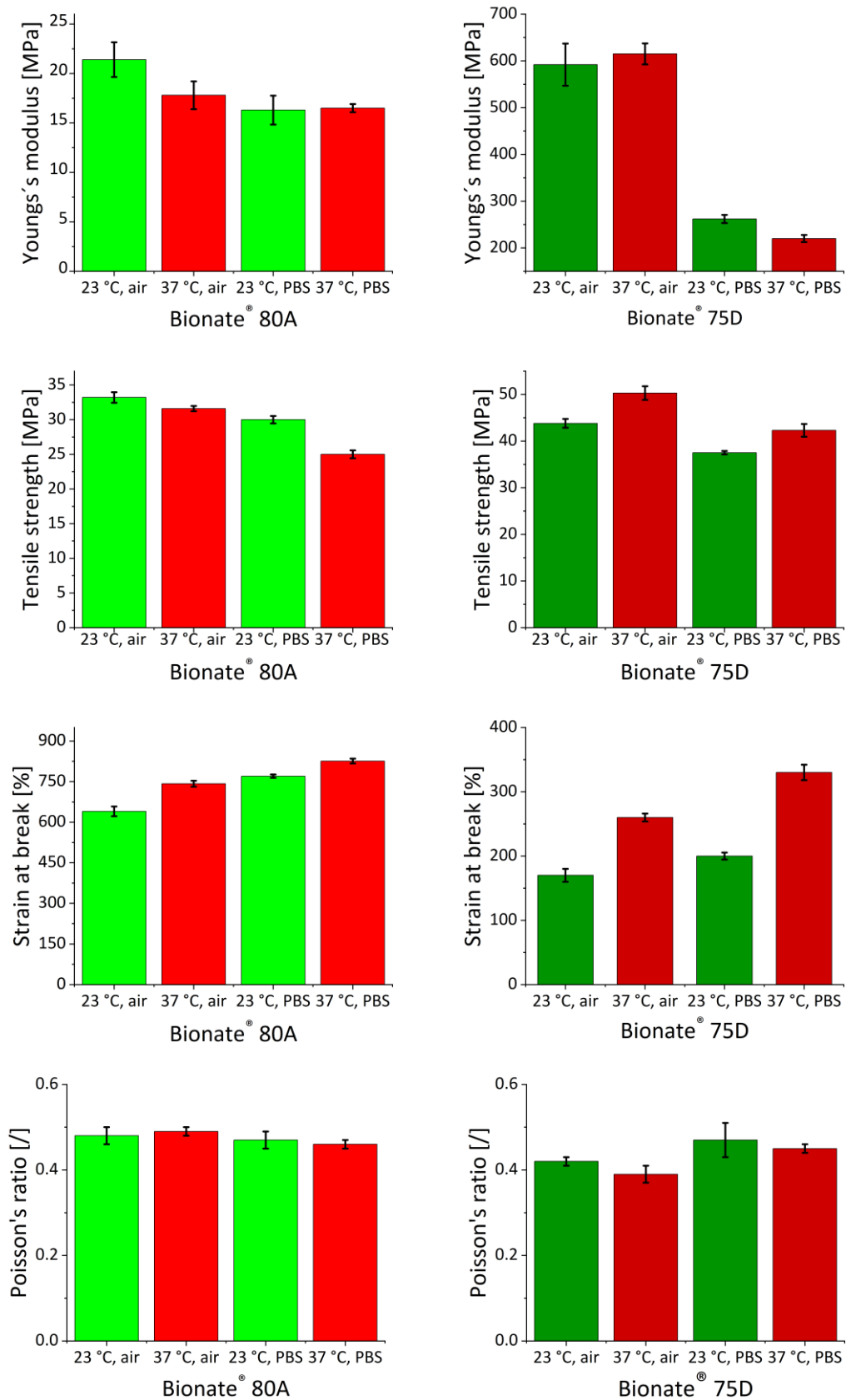
Figure 50: Comparison of the Young´s modulus, tensile strength, strain at break and Poisson´s ratio for the different conditioning and testing conditions for Bionate® 75D and 80A.

Figure 51 and Figure 52 show representative fracture surfaces for each testing condition of the Bionate® 75D and 80A tensile specimens, respectively. No significant differences between the fracture surfaces of the stored and non-stored specimens could be observed. Furthermore, the quality of the printing process is satisfactory, as no imperfections are visible. For Bionate® 75D, the overload fracture at the end of the test is evident on the fracture surfaces.
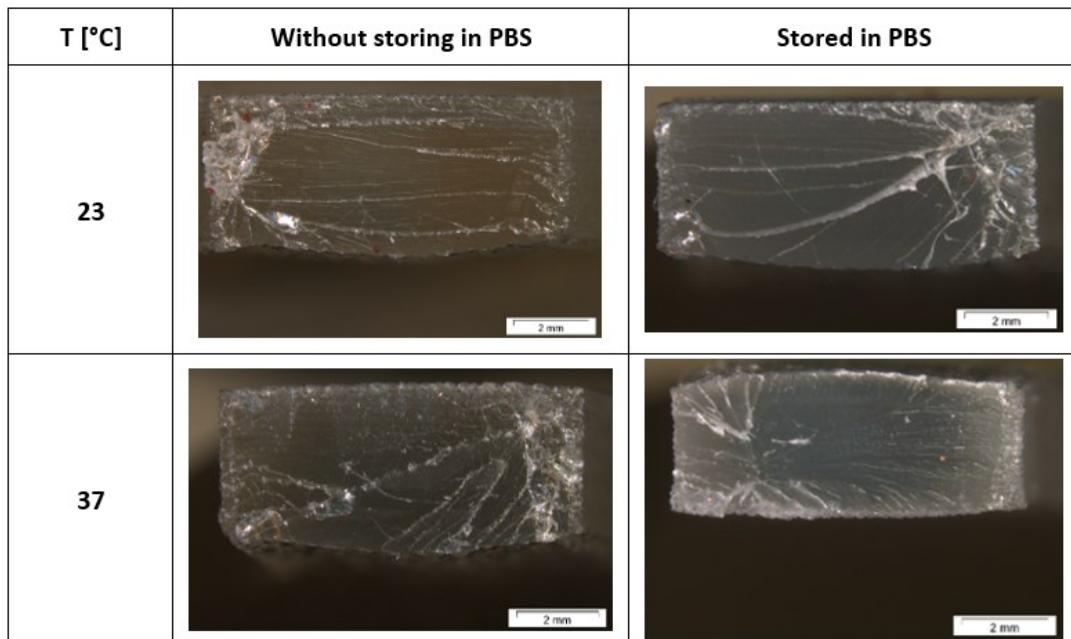


Figure 51: Fracture surfaces of the Bionate® 80A tensile specimens.
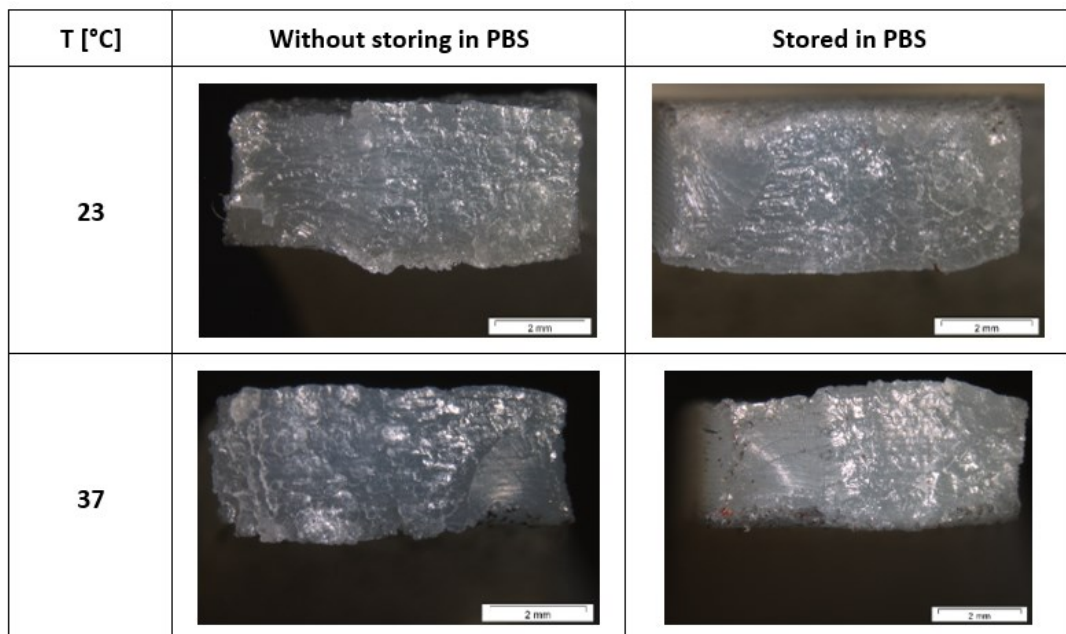


Figure 52: Fracture surfaces of the Bionate® 75D tensile specimens.

### 5.2.3 High-cycle fatigue test

Three $S$-$N$ curves were obtained from the high-cycle fatigue tests, in order to analyse the influence of the PBS solution on the fatigue behaviour (Figure 53). Six datapoints are labelled in this diagram since they are used for hysteresis investigations on the following pages.

First, reference measurements were performed in air at 37 °C. Afterwards, specimens, without previously storing in the PBS solution, were tested immersed in the media at 37 °C. Hence, the influence of the immersion time, correlating with the PBS uptake, could be investigated. Finally, the previously stored and fully saturated specimens were tested in media at 37 °C. The $S$-$N$ curves were generated by applying a power law to the measured data points. Tests in air and without pre-storing the specimens in PBS resulted in the highest stress levels (curve I). When testing the previously stored specimens in the PBS environment, the $S$-$N$ curve was shifted almost parallel to lower stress levels (curve III). A decrease in the bearable stresses of approx. 6 MPa was observed. The specimens tested in PBS, but without previous storing, failed at stresses between the curves I and III. The $S$-$N$ curve II approaches curve III with decreasing stresses and, consequently, increasing testing times. A cross-over point of curves II and III arises at around 255000 cycles. However, it must be assumed that this is not a real cross-over point. It would be illogical for the stored specimens to withstand higher stresses than those that were not stored in PBS. Instead, curve II potentially shows a kink before the cross-over point is reached and the slope approaches that of curve I. The outer data point at 438000 cycles supports this thesis. The continuous purple line in Figure 53, constructed from two fits, represents the assumed shape of curve II. To describe this behaviour more precisely, further measurements would be necessary.

Nonetheless, it can be concluded that with increasing PBS uptake the resistance against fatigue failure decreases. According to the conditioning study presented before, the specimens from curve II are completely saturated after 16 days. For the data points at around 100000 cycles, where curves II and III merge and the corresponding immersion time is approx. 28 hours, the specimens are only saturated to around 20 %. Therefore, it can be

concluded that already small amounts of absorbed PBS led to a significant decrease in fatigue resistance and, hence, a decrease in service life.
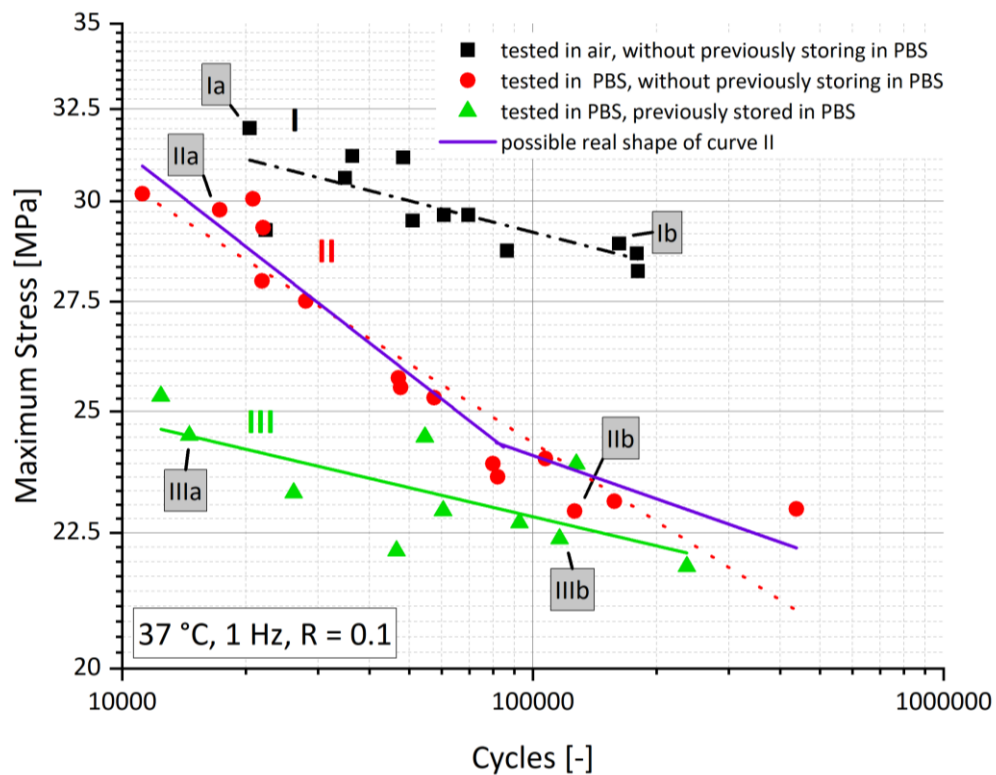


Figure 53: S-N curves for Bionate® 75D.

In Figure 54 the hysteresis for two selected specimens (one at high and the other at low loads, both labelled in Figure 53) tested in air without previously storing in PBS is illustrated. Three hysteresis loops are presented for each specimen, the first at 100 cycles, the second at half of the cycles to failure and the third at the end of testing. The area within the hysteresis loops decreases as the cycle number increases in the beginning of the test. The reason for this is that at the beginning of the test, there is a high chain mobility, leading to higher energy dissipation. With increasing number of load cycles, the chains get more and more oriented into testing direction. This orientation process, correlating with high elongation, happens during the first few hundred cycles. Looking at the strains, it is obvious that most of the elongation happens at the start of the test, whereas in the second half of the test the increase in strain is far less. This further elongation after the initial phase can be referred to cyclic creep.

Figure 54: Hysteresis during the high-cycle fatigue test for Bionate® 75D tested at air, without previously storing in PBS.

Figure 55 illustrates representative hysteresis loops for testing in PBS with previously storing in PBS. The principle of specimen selection and depicted loops is the same as for Figure 54. When comparing the shape of the loops with those without the influence of PBS, for testing in PBS the non-linearity between stress and strain is more distinctive. As observed by tensile testing, the medium acts as plasticiser, boosting the chain mobility and hence energy loss.
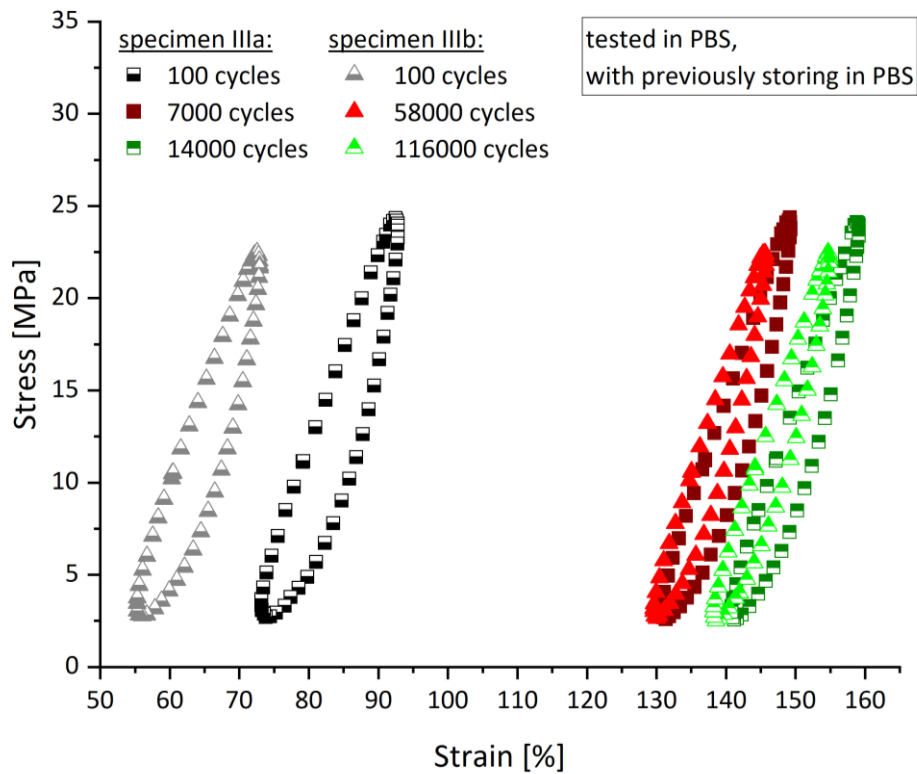
Figure 55: Hysteresis during the high-cycle fatigue test for Bionate® 75D tested in PBS, previously stored in PBS.

Figure 56 illustrates the time dependent influence of PBS, when the specimens where not pre-stored. In contrast to tests without PBS and testing the fully saturated specimens in PBS, the dissipated energy increases with increasing cycle numbers, especially when testing at low loads and consequently long immersion times. Testing at higher loads does not lead to a noticeable increase in energy loss as only little amounts of PBS can be absorbed within this short time.
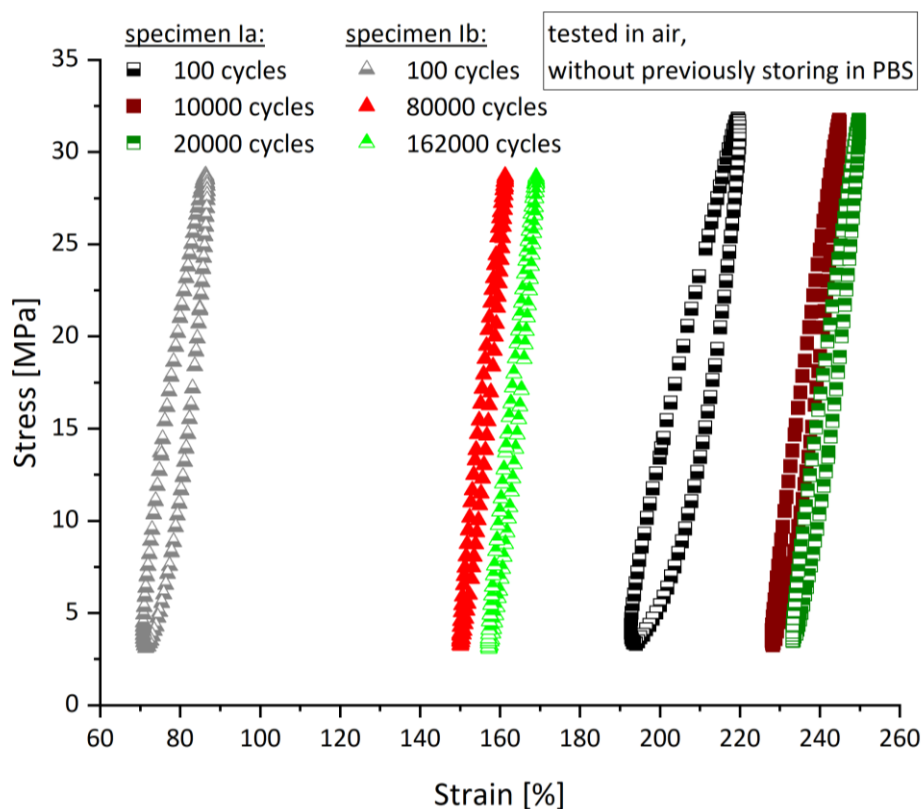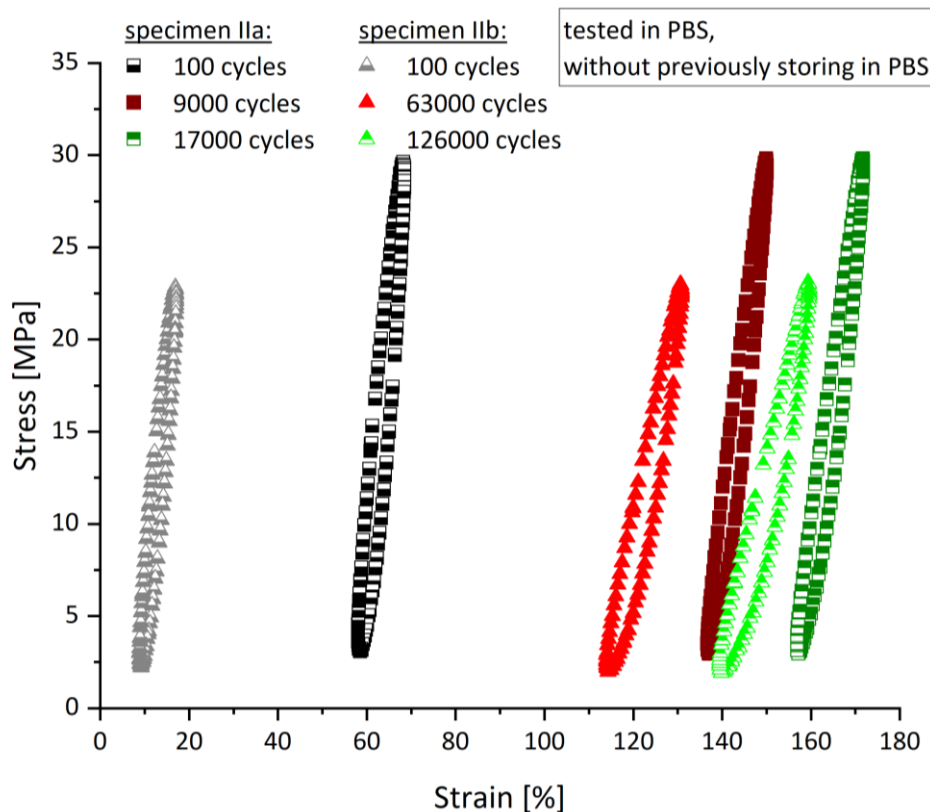
Figure 56: Hysteresis during the high-cycle fatigue test for Bionate® 75D tested in PBS, without previously storing in PBS.

Based on the hysteresis investigation, the dynamic and the secant modulus were determined (Figure 57). No additional equipment was used for exactly measuring the local strain during testing. Strains were calculated from the crosshead displacement. Subsequently, the observed values for the moduli should only be used in direct comparison and not as material values. As the machine needed some cycles to reach the set forces, the evaluation for the moduli is depicted only after the 100th cycle. Due to the large deformation at the beginning of the test due to primary creep, $E_S$ drops dramatically. For testing in PBS, without previous conditioning, $E_S$ decreases less pronounced at lower loads, but as the amount of absorbed medium increases, the values approach those for fully saturated specimens. $E_{dyn}$ indicates the same trend for testing in air and for testing the fully saturated specimens in PBS. At higher cycle numbers, $E_{dyn}$ increases minimally, which can be attributed to strain hardening. This behaviour can also be seen by a little increase of the slope of the hysteresis loops. Interestingly, there is no distinct decrease in $E_{dyn}$, which is a measure for damage in the material, before failure. For testing the non-previously stored specimens in PBS, $E_{dyn}$ proceeds different. Starting at higher levels, it

decreases and approaches to $E_{dyn}$ from the fully saturated specimens. As can be seen, it even falls below $E_{dyn}$ from the fully saturated specimens at approx. 70000 cycles. Probably the inaccurate strain determination via the crosshead displacement is responsible for this otherwise implausible observation. The trend of $E_{dyn}$ can also be observed in the hysteresis loops. The hysteresis loops at 100 cycles look more linear than those at 100 cycles for testing at air. The reason for this is that after 100 cycles no influence of the medium is given and when looking at the results of the tensile tests (Figure 49 on p. 61), it can be concluded that at these applied lower loads, and hence lower strains, the material is much stiffer and shows less plasticisation. At higher cycle numbers, the slope of the loops decreased due to the absorption of the medium. Comparing the values at different load levels, it can be concluded that lower loads lead to higher dynamic moduli, as expected for high stresses beyond linear-viscoelasticity. Furthermore, $E_{dyn}$ is notworthy higher when tested in air.
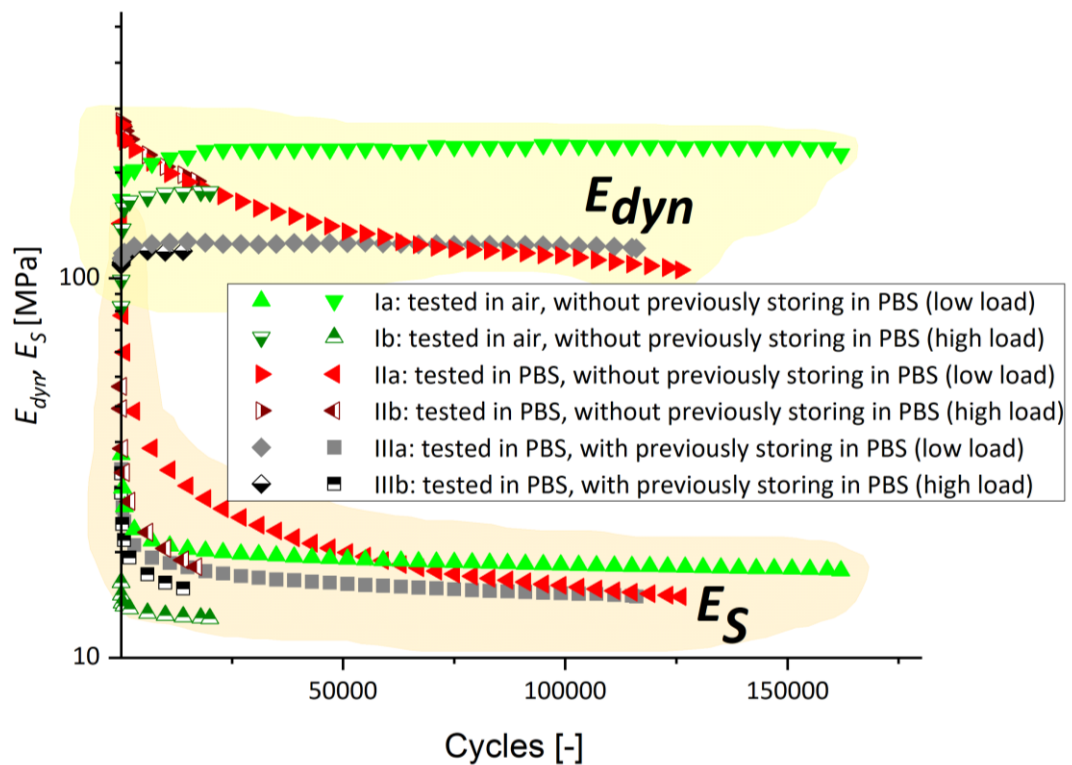


Figure 57: Dynamic and secant moduli for the different conditioning and testing conditions for Bionate® 75D at two different load levels.

Figure 58 shows the front side of a specimen tested in PBS without previously storing. Multiple crazes were detected along the specimen. The cracks initiate at the edge of the specimen and then they grow into it. As soon as one crack is large enough, so that the

remaining cross-section is no longer able to withstand the applied stresses, the specimen fails abruptly. This behaviour was also observed at the fracture surfaces (Figure 59). In these pictures, the left area of the fracture surfaces represents stable crack growth and the right, more disrupted area, represents the final, abrupt failure.
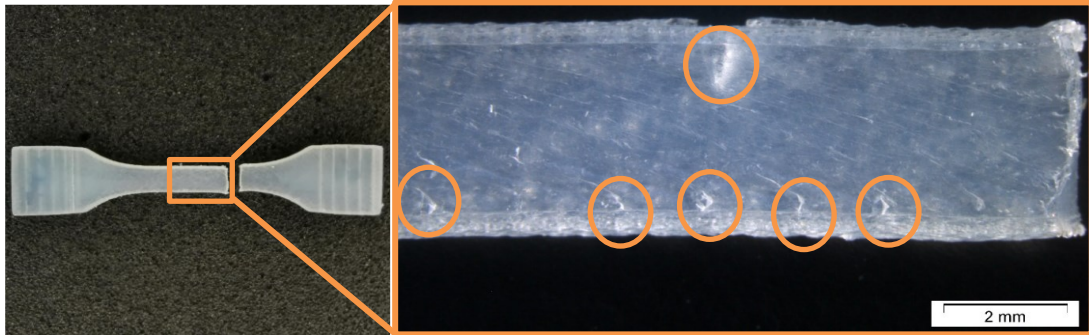


Figure 58: Multiple crazes along a specimen tested in PBS without previously storing.
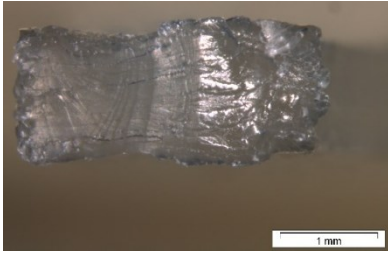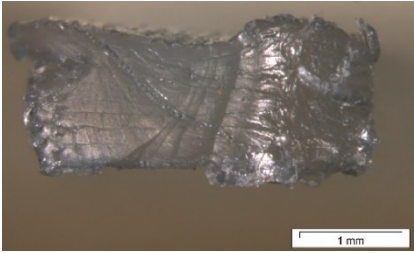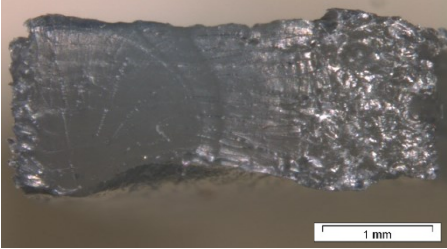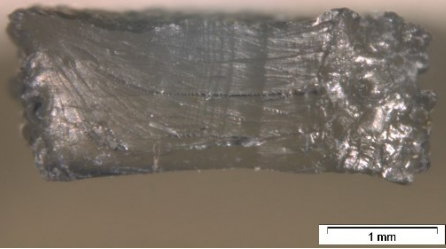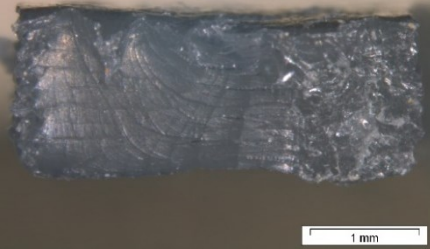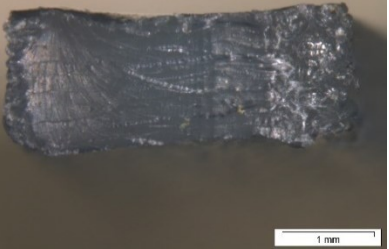
| Without storing in PBS, tested at air |  |  |
|---|---|---|
| $N$ [/] <br> $\sigma_o$ [MPa] | 20417 <br> 31.96 | 180093 <br> 28.23 |
| **Without storing in PBS, tested in PBS** |  |  |
| $N$ [/] <br> $\sigma_o$ [MPa] | 22045 <br> 29.32 | 14551 <br> 24.48 |
| **With storing in PBS, tested in PBS** |  |  |
| $N$ [/] <br> $\sigma_o$ [MPa] | 14551 <br> 24.48 | 116091 <br> 22.38 |

Figure 59: Fracture surface of the specimens for the high-cycle fatigue test for two different load levels with the number of cycles to failure and the maximum stress.

# 6 CONCLUSION AND OUTLOOK

In order to see how polymeric materials behave in actual applications, different tests were conducted in environments as close to reality as possible. The influence of sunflower oil on two different high impact polystyrene (HIPS) grades was investigated using cyclic and static load tests based on linear-elastic fracture mechanics. Environmental stress cracking (ESC) led to significant lower bearable stresses for both materials. Larger rubber particles were less prone to ESC, because crazes with a higher fibril volume fraction with fewer voids hampered the flow of the medium to the crack tip. For testing in air, HIPS with smaller rubber particles showed a greater resistance against crack growth under static loading. On the contrary, under cyclic loading, HIPS with the larger rubber particle size was superior. An explanation for the higher performance of HIPS with larger rubber particles under fatigue loading could be the change in the failure mechanism from ductile to brittle failure. Further fracture mechanics tests under cyclic loads are necessary in order to investigate the material behaviour at higher loads and hence lower cycles to failure. Moreover, notch strengthening and weaking can cause the inversed ranking of HIPS A and HIPS B under static and fatigue loading. Since the cracked round bar (CRB) test is not recommended for determining crack growth kinetics because often asymmetrically crack growth occurs [55], performing the cyclic fatigue test on the compact tension (CT) specimens should be preferred. To obtain more insight on the different behaviour between dynamic and static loading, focus should also be put on crack initiation times. Probably the smaller rubber particles cause higher stress concentrations at the interface between particles and polystyrene matrix, leading to faster failure under fatigue loads. Furthermore, detailed observations of the fracture surfaces using a scanning electron microscope (SEM) would be desirable. However, due to the absorption of oil, sample preparation for SEM was not possible.

The CRB test on HIPS showed worse results for the coefficient of determination ($R^2$) compared to polyethylene, which can be attributed to the influence of the oil and the rubber modification. Hence, the scope of testing of four specimens, as recommended in ISO 18489:2015, is insufficient to obtain reliable results.

The optical crack tip detection at the static load test proved to be problematic under the influence of the oil, as multiple crack tips across the specimen's cross-section occurred. Moreover, an automated crack tip measurement in ImageJ was not possible due to this complex fracture behaviour. Hence, determining the crack length must be done manually. Furthermore, the obtained results must be questioned critically because evaluating the wrong crack tip can lead to non-plausible results. Also, the decreasing width of the ligament at increasing crack lengths for testing in oil makes the application of the equations of linear-elastic fracture mechanics questionable. At this point, it must be summarised that the CT specimens have not proven effective for determining crack kinetics and environmental stress cracking resistance. It remains to be seen what results the other participants in the round robin test will achieve. Nonetheless, one subject of future research may be uniformly crack tip evaluation when different crack fronts occur so that subjectivities can be ruled out. Moreover, the effective ligament width would have to be recorded in order to enable correct calculations.

The second part of this thesis dealt with the influence of phosphate-buffered saline (PBS) on two polycarbonate polyurethane (PCU) grades. The conditioning study showed that the hard segment made of polyurethane is more prone to PBS absorption. Further, it was observed that increased temperatures led to an increased and faster uptake of the PBS by the polymer. Tensile tests showed that the absorption of body-like fluids leads to a decrease in stiffness and tensile strength and an increase in elongation at break. Similar effects could be observed by increased temperature, although the tensile strength increased for the material with the higher hard segment content. A possible explanation for this could be the enhanced chain mobility at temperatures closer to the glass transition temperature. A detailed investigation of the morphology of the used PCU could be subject of further research in order to better understand the influence of the temperature. The Poisson's ratio of the softer PCU was not influenced by the increased temperature and the PBS uptake. In contrast, an increase of the Poisson's ratio due to the absorbed medium was detected for the harder material. It must be weighed up whether these changes in stiffness, tensile strength and elongation are allowable for the desired application.

The high-cycle fatigue tests showed that as the amount of liquid absorbed increases, the fatigue behaviour deteriorates considerably. It was found that a saturation around 20 %

already lead to a significant decrease in fatigue resistance and, hence, a decrease in service life. Thus, if corresponding loads act on the implant, a significant drop in fatigue strength can be expected shortly after implantation, which must be considered when dimensioning and simulating the desired application. Moreover, this dependency on the amount of absorbed medium was also observed for the dynamic and secant modulus. Last but not least, it was found that the absorption of PBS promotes energy dissipation.

# 7    REFERENCES

1.    Wright D. C. (1996) Environmental stress cracking of plastics. Rapra Technology, Shrewsbury

2.    Jansen J.A. (2004) Environmental stress cracking - the plastic killer. Advanced Materials & Processes

3.    Grellmann W., Seidler S. (2011) Polymer Testing. Hanser, München

4.    Spektra "RoundRobin Test and Interlaboratory Comparison Program - SPEKTRA R ". https://www.spektra-dresden.com/en/dienstleistungen/round-robin-tests.html. Accessed 14 May 2022

5.    PIERSON R. H., FAY E. A. (1959) Guidelines for Interlaboratory Testing Programs. Analytical Chemistry:25A-49A. https://doi.org/10.1021/ac60156a708

6.    Jansen J. (2015) Plastic Failure through Environmental Stress Cracking. Plastics Engineering. https://doi.org/10.1002/j.1941-9635.2015.tb01435.x

7.    Kambour R. P. (1973) Solvent crazing of "dry" polystyrene and "dry" crazing of plasticized polystyrene. Journal of Polymer Science. https://doi.org/10.1002/pol.1973.180111003

8.    Schoeffl P. F., Bradler P. R., Lang R. W. (2014) Yielding and crack growth testing of polymers under severe liquid media conditions. Polymer Testing 40:225–233. https://doi.org/10.1016/j.polymertesting.2014.09.005

9.    Fischer J., Freudenthaler P. J., Bradler P. R. et al. (2019) Novel test system and test procedure for fatigue crack growth testing with cracked round bar (CRB) specimens. Polymer Testing 78:105998. https://doi.org/10.1016/j.polymertesting.2019.105998

10.   Bertouche S., Sahraoui N., Boutekedjiret C. et al. (2018) Determining Hansen Solubility Parameters by StefanisPanayiotou Method for Fatty Acids Extraction by Petrochemical and Green Solvents. International Journal of Scientific Research & Engineering Technology 6:14-20

11.   Frick A. (2010) Praktische Kunststoffprüfung. Hanser Verlag, München

12. Ehrenstein G. W. (2011) Polymer-Werkstoffe: Struktur - Eigenschaften - Anwendung. Hanser, München

13. Boubakri A., Haddar N., Elleuch K. et al. (2010) Impact of aging conditions on mechanical properties of thermoplastic polyurethane. Materials & Design 31:4194–4201. https://doi.org/10.1016/j.matdes.2010.04.023

14. Jouwersma C. (1959) Die Diffusion von Wasser in Kunststoffe. Chemie Ingenieur Technik:652–658. https://doi.org/10.1002/cite.330311006

15. Valenzuela L. M., Michniak B., Kohn J. (2011) Variability of water uptake studies of biomedical polymers. Journal of Applied Polymer Science:1311–1320. https://doi.org/10.1002/app.33485

16. Crank J. (1975) The Mathematics of Diffusion, 2nd edn. Oxford university press, Oxford

17. Comyn J. (1985) Polymer Permeability. Springer, Dordrecht

18. Huacuja-Sanchez J. E. Müller, K., Possart W. (2016) Water diffusion in a crosslinked polyether-based polyurethane adhesive. International Journal of Adhesion and Adhesives. https://doi.org/10.1016/j.ijadhadh.2016.01.005

19. Suresh S. (2012) Fatigue of Materials, 2nd edn. Cambridge University Press, Cambridge

20. Anderson T. L. (2017) Fracture mechanics: fundamentals and applications, 4th edn. CRC Press, Boca Raton

21. Moore D. R. (ed) (2004) The application of fracture mechanics to polymers, adhesives and composites. ESIS publication, vol 33. Elsevier, Amsterdam, Heidelberg

22. Heinrich W. (1980) Broek, D., Elementary Engineering Fracture Mechanics. Alphen aan den Rijn, Sijthoff & Noordhoff 1978. Zeitschrift für angewandte Mathematik und Mechanik 60:60. https://doi.org/10.1002/zamm.19800600120

23. Broek D. (1982) Elementary engineering fracture mechanics. Springer Dodrecht, Cham

24. Stern A., Asanger F., Lang R. W. (1998) Creep crack growth testing of plastics—II. data acquisition, data reduction and experimental results. Polymer Testing 17:423–441. https://doi.org/10.1016/S0142-9418(97)00068-8

25. Beaumont P. W. R., Young R. J. (1975) Failure of brittle polymers by slow crack growth. Journal of Materials Science:1334–1342. https://doi.org/10.1007/BF00540823

26. Marshall G. P., Coutts L. H., Williams J. G. (1974) Temperature effects in the fracture of PMMA. Journal of Materials Science 9:1409–1419. https://doi.org/10.1007/BF00552926

27. Andena L., Castellani L., Castiglioni A et al. (2013) Determination of environmental stress cracking resistance of polymers: Effects of loading history and testing configuration. Engineering Fracture Mechanics. https://doi.org/10.1016/j.engfracmech.2012.09.004

28. Blumenauer H. (1989) Werkstoffprüfung, 5th edn. Dt. Verl. für Grundstoffindustrie, Leipzig

29. Carlowitz B., Boysen M. (1990) Die Kunststoffe: Chemie, Physik, Technologie, vol 1. Hanser, München

30. Altstädt V., Ehrenstein G. W. (eds) (1987) Hysteresismessungen zur Charakterisierung der mechanisch-dynamischen Eigenschaften von R-SMC: Zusammenhang von Struktur und Eigenschaften. Zugl.: Kassel, Gesamthochsch., FB Maschinenbau, Diss. : 1987. Inst. für Werkstofftechnik, Kassel

31. Talreja R., Manson J.-A. E. (op. 2001) Polymer matrix composites, 1st ed. A comprehensive composite materials publication. Elsevier, Oxford, Amsterdam

32. Pinter G., Ladstatter E., Billinger W. et al. (2006) Characterisation of the tensile fatigue behaviour of RTM-laminates by isocyclic stress–strain-diagrams. International Journal of Fatigue 28:1277–1283. https://doi.org/10.1016/j.ijfatigue.2006.02.012

33. Salimi M., Pirouzfar V., Kianfar E. (2017) Enhanced gas transport properties in silica nanoparticle filler-polystyrene nanocomposite membranes. Colloid and Polymer Science:215–226. https://doi.org/10.1007/s00396-016-3998-0

34. Donald A. M., Kramer E. J. (1982) Internal structure of rubber particles and craze break-down in high-impact polystyrene (HIPS). Journal of Materials Science 17:2351–2358. https://doi.org/10.1007/BF00543744

35. Altstädt V. (2005) The Influence of Molecular Variables on Fatigue Resistance in Stress Cracking Environments. In: Intrinsic Molecular Mobility and Toughness of Polymers II. Springer, Berlin, Heidelberg, pp 105–152

36. Altstädt V., Keiter S., Renner M. et al. (2004) Environmental Stress Cracking of Polymers Monitored by Fatigue Crack Growth Experiments. Macromolecular Symposia:31–46. https://doi.org/10.1002/masy.200451004

37. Corleto C. R., Sosa J., Bradley W. L. (1996) Fracture behavior of high-impact polystyrene under an aggressive environment. Polymer Engineering & Science

38. Grassi V. G., Dal Pizzol M. F., Forte M. M. C. et al. (2009) High impact polystyrene with enhanced environmental stress cracking resistance. Anais do 10o Congresso Brasileiro de Polímeros

39. Kamaludin M., Patel Y., Blackman B. et al. (2016) Fracture mechanics testing for environmental stress cracking in thermoplastics. Procedia Structural Integrity 2:227–234. https://doi.org/10.1016/j.prostr.2016.06.030

40. Bubeck R. A., Arends C. B., Hall E. L. et al. (1981) Environmental stress cracking in impact polystyrene. Polymer Engineering & Science 21:624–633. https://doi.org/10.1002/pen.760211009

41. Geary C., Birkinshaw C., Jones E. (2008) Characterisation of Bionate polycarbonate polyurethanes for orthopaedic applications. Journal of materials science. Materials in medicine 19:3355–3363. https://doi.org/10.1007/s10856-008-3472-8

42. Cipriani E., Zanetti M., Brunella V. et al. (2012) Thermoplastic polyurethanes with polycarbonate soft phase: Effect of thermal treatment on phase morphology. Polymer Degradation and Stability 97:1794–1800. https://doi.org/10.1016/j.polymdegradstab.2012.06.004

43. Yilgör I., Yilgör E., Wilkes G. L. (2015) Critical parameters in designing segmented polyurethanes and their effect on morphology and properties: A comprehensive review. Polymer 58:A1-A36. https://doi.org/10.1016/j.polymer.2014.12.014

44. Mishra A., Seethamraju K., Delaney J. et al. (2015) Long-term in vitro hydrolytic stability of thermoplastic polyurethanes. Journal of biomedical materials research. Part A 103:3798–3806. https://doi.org/10.1002/jbm.a.35523

45. Chandy T., van Hee J., Nettekoven W. et al. (2009) Long-term in vitro stability assessment of polycarbonate urethane micro catheters: resistance to oxidation and stress cracking. Journal of Biomedical Materials Research Part B: Applied Biomaterials 89:314–324. https://doi.org/10.1002/jbm.b.31218

46. Dempsey D. K., Carranza C., Chawla C. P. et al. (2014) Comparative analysis of in vitro oxidative degradation of poly(carbonate urethanes) for biostability screening. Journal of Biomedical Materials Research Part A 102:3649–3665. https://doi.org/10.1002/jbm.a.35037

47. Christenson E. M., Dadsetan M., Wiggins M. et al. (2004) Poly(carbonate urethane) and poly(ether urethane) biodegradation: in vivo studies. Journal of biomedical materials research. Part A 69:407–416. https://doi.org/10.1002/jbm.a.30002

48. Simmons A., Hyvarinen J., Odell R. A. et al. (2004) Long-term in vivo biostability of poly(dimethylsiloxane)/poly(hexamethylene oxide) mixed macrodiol-based polyurethane elastomers. Biomaterials 25:4887–4900. https://doi.org/10.1016/j.biomaterials.2004.01.004

49. Wiggins M. J., MacEwan M., Anderson J. M. et al. (2004) Effect of soft-segment chemistry on polyurethane biostability during in vitro fatigue loading. Journal of biomedical materials research. Part A 68:668–683. https://doi.org/10.1002/jbm.a.20081

50. DMS "Bionate® Bionate-Thermoplastic Polycarbonate Polyurethane (PCU)". https://www.dsm.com/content/dam/dsm/biomedical/en_us/documents/document-bionate-pcu-productsheet.pdf. Accessed 30 Mar 2022

51. U.S. Food & Drug Administration "What We Do". https://www.fda.gov/about-fda/what-we-do#mission. Accessed 23 May 2022

52. Prochor P., Mierzejewska Ż. A. (2021) Bioactivity of PEEK GRF30 and Ti6Al4V SLM in Simulated Body Fluid and Hank's Balanced Salt Solution. Materials 14:2059. https://doi.org/10.3390/ma14082059

53. Greelane "Herstellung einer phosphatgepufferten Salzlösung". https://www.greelane.com/wissenschaft-technologie-mathematik/wissenschaft/phosphate-buffered-saline-pbs-solution-4061933/. Accessed 30 Mar 2022

54. Frank A., Freimann W., Pinter G. et al. (2009) A fracture mechanics concept for the accelerated characterization of creep crack growth in PE-HD pipe grades. Engineering Fracture Mechanics 76:2780–2787. https://doi.org/10.1016/j.engfracmech.2009.06.009

55. Pinter G., Haager M., Balika W. et al. (2007) Cyclic crack growth tests with CRB specimens for the evaluation of the long-term performance of PE pipe grades. Polymer Testing 26:180–188. https://doi.org/10.1016/j.polymertesting.2006.09.010

56. Murakami Y. (1990) Stress intensity factors handbook. Pergamon, Oxford

57. Sih G. C. (1973) Methods of Analysis and Solutions of Crack Problems: Recent developments in fracture mechanics Theory and methods of solving crack problems. Mechanics of fracture. Springer Dordrecht, Leyden

58. Mao J., Li X., Bao S. et al. (2019) Comparative Study of the Geometric Effects on Fracture Behaviors of Side-Grooved and Plain-Sided Compact Tension Specimens. J of Materi Eng and Perform 28:6514–6524. https://doi.org/10.1007/s11665-019-04335-1

59. ARBURG GmbH + Co KG "The APF process - ARBURG". https://www.arburg.com/en/gb/products-and-services/additive-manufacturing/the-apf-process/. Accessed 11 Apr 2022

60. Cold Spring Harbor Laboratory Press (2006) Phosphate-buffered saline (PBS). Cold Spring Harbor Protocols:pdb.rec8247. https://doi.org/10.1101/pdb.rec8247

61. Krijger de J., Rans C., van Hooreweder B. et al. (2017) Effects of applied stress ratio on the fatigue behavior of additively manufactured porous biomaterials under compressive loading. J Mech Behav Biomed Mater 70:7–16. https://doi.org/10.1016/j.jmbbm.2016.11.022

62. Ferdous W., Manalo A., Yu P. et al. (2021) Tensile Fatigue Behavior of Polyester and Vinyl Ester Based GFRP Laminates-A Comparative Evaluation. Polymers (Basel) 13. https://doi.org/10.3390/polym13030386

63. Kratochvilla T. R., Frank A., Pinter G. (2014) Determination of slow crack growth behaviour of polyethylene pressure pipes with cracked round bar test. Polymer Testing 40:299–303. https://doi.org/10.1016/j.polymertesting.2014.10.002

64. Frank A., Pinter G. (2014) Evaluation of the applicability of the cracked round bar test as standardized PE-pipe ranking tool. Polymer Testing 33:161–171. https://doi.org/10.1016/j.polymertesting.2013.11.013

65. Arbeiter F., Schrittesser B., Frank A. et al. (2015) Cyclic tests on cracked round bars as a quick tool to assess the long term behaviour of thermoplastics and elastomers. Polymer Testing 45:83–92. https://doi.org/10.1016/j.polymertesting.2015.05.008

66. Solberg K., Berto F. (2020) The effect of defects and notches in quasi-static and fatigue loading of Inconel 718 specimens produced by selective laser melting. International Journal of Fatigue 137:105637. https://doi.org/10.1016/j.ijfatigue.2020.105637

67. Frank A., Berger I. J., Arbeiter F. et al. (eds) (2014) Characterization of crack initiation and slow crack growth resistance of PE 100 and PE 100 RC pipe grades with Cyclic Cracked Round Bar (CRB) Tests Proceedings, 17th Plastic Pipes Conference Proceedings

68. Williams J. G., Marshall G. P. (1975) Environmental crack and craze growth phenomena in polymers. Proceedings of the Royal Society of London. A. Mathematical and Physical Sciences 342:55–77. https://doi.org/10.1098/rspa.1975.0012

69. Petrović Z., Zavargo Z., Flyn J. et al. (1994) Thermal degradation of segmented polyurethanes. Journal of Applied Polymer Science 51:1087–1095. https://doi.org/10.1002/app.1994.070510615

70. Kozakiewicz J., Rokicki G., Przybylski J. et al. (2010) Studies of the hydrolytic stability of poly(urethane–urea) elastomers synthesized from oligocarbonate diols. Polymer Degradation and Stability 95:2413–2420. https://doi.org/10.1016/j.polymdegradstab.2010.08.017

71. Tang Y. W., Labow R. S., Santerre J. P. (2001) Enzyme-induced biodegradation of polycarbonate-polyurethanes: Dependence on hard-segment chemistry. Journal of biomedical materials research 57:597–611. https://doi.org/10.1002/1097-4636(20011215)57:4<597:aid-jbm1207>3.0.co;2-t

72. Solouki Bonab V., Manas-Zloczower I. (2017) Revisiting thermoplastic polyurethane, from composition to morphology and properties. Journal of Polymer Science Part B: Polymer Physics 55:1553–1564. https://doi.org/10.1002/polb.24413

73. Amjadi M., Fatemi A. (2020) Tensile Behavior of High-Density Polyethylene Including the Effects of Processing Technique, Thickness, Temperature, and Strain Rate. Polymers (Basel) 12. https://doi.org/10.3390/polym12091857

74. Xiao S., Sue H.-J. (2019) Effect of molecular weight on scratch and abrasive wear behaviors of thermoplastic polyurethane elastomers. Polymer 169:124–130. https://doi.org/10.1016/j.polymer.2019.02.059

75. Schollenberger C. S., Dinbergs K. (1973) Thermoplastic Urethane Molecular Weight-Property Relations. Journal of Elastoplastics 5:222–251. https://doi.org/10.1177/009524437300500404

76. Landel R. F., Nielsen L. E. (1993) Mechanical properties of polymers and composites, Second edition. Mechanical engineering. CRC Press, Boca Raton

77. Bersted B. H. (1979) Entanglement network model relating tensile impact strength and the ductile-brittle transition to molecular structure in amorphous polymers. Journal of Applied Polymer Science 24:37–50. https://doi.org/10.1002/app.1979.070240105

78. Nic An Ghaill N., Little E. G. (2008) Determination of the mechanical properties of Bionate 80A and Bionate 75D for the stress analysis of cushion form bearings. Proceedings of the Institution of Mechanical Engineers. Part H, Journal of engineering in medicine 222:683–694. https://doi.org/10.1243/09544119JEIM372

79. Krauklis A. E., Gagani A. I., Echtermeyer A. T. (2018) Hygrothermal Aging of Amine Epoxy: Reversible Static and Fatigue Properties. Open Engineering 8:447–454. https://doi.org/10.1515/eng-2018-0050

80. Theocaris P. S. (1979) Influence of plasticizer on Poisson's ratio of epoxy polymers. Polymer 20:1149–1154. https://doi.org/10.1016/0032-3861(79)90308-2

81. Fine R. A., Millero F. J. (1973) Compressibility of water as a function of temperature and pressure. The Journal of Chemical Physics 59:5529–5536. https://doi.org/10.1063/1.1679903

# APPENDIX

## A1 | Parameters for compression moulding of HIPS A and HIPS B plates for the preparation of CT specimens

According to the ESIS testing protocol the moulding procedure is defined as followed:

1.) Preheat mould at 200 °C.

2.) Spread pellets in the open mould, then close the mould with no pressure applied.

3.) Preheat the pellets for ten minutes.

4.) Apply 2 MPa pressure for six to seven minutes.

5.) Increase the pressure to 4 MPa for eight minutes.

6.) Release the pressure and cool down to 140 °C with approximately 9 °C/min.

7.) Slow cooling to 140 °C with 1 to 2 °C/min.

8.) Cooling to room temperature.

To reproduce this procedure as similar as possible, the following steps were conducted:

1.) Place a PTFE film on both side of the tool (to ensure a flawless ejection).

2.) Preheat the mould to 220 °C for approximately one hour (Temperature is set 20 °C higher as ordered due to heat loss).

3.) Put 270 g of the granules into the opened mould, then close the mould without applying pressure for ten minutes.

4.) Set the pressure to 100 bar for six minutes.

5.) Increase the pressure to 160 bar for eight minutes.

6.) Turn of the heating (The oil continuous to circulate –> Cooling due to cooler ambient air.

7.) Turn of the temperature unit after one hour.

8.) Switch of the machine after two hours.

For step 4) and 5), the required pressure is calculated with the following equation, where $p_c$ is the pressure in the hydraulic cylinder, set at the machine control unit, $p_t$ is the acting pressure in the tool, $A_z$ is the cross section of the cylinder and $A_t$ is the cross section of the tool:

$$p_c = p_t * \frac{A_t}{A_z}$$

**A2 | Parameters for APF of Bionate® 80A and Bionate® 75D multipurpose specimens**

|  | Bionate® 80A | Bionate® 75D |
|---|---|---|
| **Building chamber temperature [°C]** | 80 | 110 |
| **Cylinder temperature T1 [°C]** | 180 | 160 |
| **Cylinder temperatureT2 [°C]** | 185 | 210 |
| **Nozzle temperature [°C]** | 195 | 220 |
| **Screw speed [m/min]** | 4 | 2 |
| **Metering stroke [mm]** | 15 | 6 |
| **Melt cushion [mm]** | 3 | 1.5 |
| **Dynamic pressure [bar]** | 50 | 100 |
| **Discharge number [%]** | 60 | 65 |
| **Form factor** | 1.15 | 1.225 |
| **Overlapping [%]** | 75 | 60 |
| **Layer thickness [mm]** | 0.2 | 0.2 |
| **Nozzle diameter [mm]** | 0.2 | 0.2 |

**A3 | Results of the tensile tests as arithmetic mean of five specimens with the standard deviation in brackets**

| Material | Condition | | Young's modulus [MPa] | Tensile strength [MPa] | Strain at break [%] | Poisson's ratio [/] |
|---|---|---|---|---|---|---|
| **Bionate® 80A** | 23 °C | at air | 21.4 (1.76) | 33.2 (0.76) | 640 (18) | 0.48 (0.02) |
| | | stored in PBS | 16.3 (1.46) | 30.0 (0.53) | 770 (6.1) | 0.47 (0.02) |
| | 37 °C | at air | 17.8 (1.40) | 31.6 (0.38) | 742 (11) | 0.49 (0.01) |
| | | stored in PBS | 16.5 (0.41) | 25.0 (0.57) | 826 (8.8) | 0.46 (0.01) |
| **Bionate® 75D** | 23 °C | at air | 592 (45.0) | 43.8 (0.95) | 170 (10) | 0.42 (0.01) |
| | | stored in PBS | 615 (22.4) | 37.5 (0.37) | 200 (5.4) | 0.47 (0.04) |
| | 37 °C | at air | 262 (8.69) | 50.3 (1.42) | 260 (6.1) | 0.39 (0.02) |
| | | stored in PBS | 220 (7.62) | 42.3 (1.37) | 330 (12) | 0.45 (0.01) |